

T-3985

Temperature Determination in an Inductively Heated Graphite
Die using Finite Element Methods

by

Timothy J. P. Lewis

ARTHUR LAKES LIBRARY
COLORADO SCHOOL of MINES
GOLDEN, COLORADO 80401

ProQuest Number: 10783668

All rights reserved

INFORMATION TO ALL USERS

The quality of this reproduction is dependent upon the quality of the copy submitted.

In the unlikely event that the author did not send a complete manuscript and there are missing pages, these will be noted. Also, if material had to be removed, a note will indicate the deletion.



ProQuest 10783668

Published by ProQuest LLC (2018). Copyright of the Dissertation is held by the Author.

All rights reserved.

This work is protected against unauthorized copying under Title 17, United States Code
Microform Edition © ProQuest LLC.


ProQuest LLC.
789 East Eisenhower Parkway
P.O. Box 1346
Ann Arbor, MI 48106 – 1346

A thesis submitted to the Faculty and the Board of Trustees of the Colorado School of Mines in partial fulfillment of the requirements for the degree of Master of Science (Materials Science).

Golden, Colorado

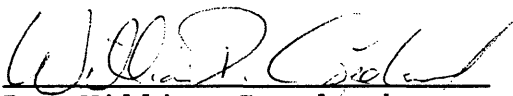
Date 1/8/91

Signed: 
Timothy Jon Patrick Lewis

Approved: 
Dr. G.L. DePoorter
Thesis Advisor

Golden, Colorado

Date JANUARY 8, 1991


Dr. William Copeland
Professor and Coordinator,
Materials Science Program

ABSTRACT

The sintering and hot pressing of optical spinels has been an area of large research interest. The understanding of the mechanisms of densification as related to the spinel's microstructure involves several steps. The first consideration is the densification temperature of the spinel being hot pressed.

The purpose of this work was to design and construct a hot press system. In addition, this work focused on measuring and calculating the temperature in the hot press die. The temperature profile in an inductively heated graphite die was predicted using Finite Element Methods (FEM). These predictions were compared to experimentally obtained temperatures. The modeling was accomplished by deriving the equations that describe the phenomena of electromagnetic heating. These equations were then implemented in a FEM code to produce temperature profiles.

The results of this work produced numerically predicted temperature profiles within a 10% accuracy of the experimentally obtained temperatures. It was also concluded that the heating characteristics of the hot press process are very sensitive to the insulation configuration.

TABLE OF CONTENTS

	<u>PAGE</u>
TABLE OF CONTENTS	v
LIST OF FIGURES	viii
LIST OF TABLES	xv
LIST OF SYMBOLS	xvi
ACKNOWLEDGMENTS	xx
Chapter 1. INTRODUCTION	1
1.1 Introduction	1
1.2 Aim of the Present Work	1
1.3 Outline of Presentation	4
Chapter 2. BACKGROUND AND LITERATURE SURVEY . .	5
2.1 Relevance and Application to this Work	5
2.2 Classical Approach to Induction Heating Problems	6
2.3 Finite Element Modeling of Magnetic Fields	8
Chapter 3. DESIGN AND CONSTRUCTION OF HOT PRESS SYSTEM	10
3.1 Introduction	10
3.2 Hot Press Stack	10
3.2.1 Design Criteria	10
3.2.2 Graphite Punch	13
3.3 Hot Press Package	13
3.4 Hydraulic Press	16
3.4.1 Hydraulic Press Support Table	18
3.4.2 Hydraulic Press Carriage .	20
3.4.3 Hydraulic Cylinder Support Structure	23

TABLE OF CONTENTS
(continued)

	<u>PAGE</u>
3.5 Hydraulic System	24
3.6 Electrical Schematic	26
3.7 Vacuum System	26
Chapter 4. ENERGY BALANCE IN THE EXPERIMENT . .	28
4.1 Introduction	28
4.2 The Heat Equation	28
4.3 The Total Heat Generated in the System	30
4.4 The Heat Convected from the Quartz Containing Vessel	32
4.5 The Total Heat Radiated from the System	35
4.6 The Total Heat Removed from the System by Mass Transport . .	35
4.7 The Energy Balance of the System	36
Chapter 5. DESIGN OF THE FINITE ELEMENT MODEL. .	37
5.1 Introduction	37
5.2 Geometry of the Finite Element Model	37
5.3 Material Properties	41
5.4 FEM Formulation of the 2-D Heat Diffusion Equation	47
5.5.1 The First DOT Input File .	51
5.5.2 The Second DOT Input File.	64
5.6 Correlation of the FEM Model to Experimental Data	65
Chapter 6. RESULTS	67
6.1 Introduction	67
6.2 Thermocouple Emplacement	67
6.3 Temperature Measurements	70
6.4 Estimation of Additional Boundary Temperatures	88
6.5 Comparison of Dot Output to Measured Temperature Profile . .	98
6.6 Postdot Interpretations of DOT Output	102

TABLE OF CONTENTS
(continued)

	<u>PAGE</u>
6.7 Energy Balance of the Hot Press System	105
Chapter 7. CONCLUSIONS AND RECOMMENDATIONS . . .	109
7.1 Conclusions	109
7.2 Recommendations	110
REFERENCES	112
APPENDIX I. DERIVATION OF THE HEAT GENERATION TERM	115
APPENDIX II. VERIFICATION OF THE Dot CODE USING SAMPLE PROBLEMS	137
APPENDIX III. LOTUS SPREADSHEET EQUATIONS FOR HEAT GENERATION CALCULATIONS	153
APPENDIX IV. CALIBRATION DATA FOR LOAD CELL	160
APPENDIX V. CERTIFICATE OF CONFORMANCE	162
APPENDIX VI. STANDARD OPERATING PROCEDURE FOR HOT PRESS	163
APPENDIX VII. DRAWINGS OF EQUIPMENT	178

LIST OF FIGURES

<u>FIGURE</u>		<u>PAGE</u>
1	Block Diagram of the Induction Hot Press System	3
2	Simplified Model of Hot Press Stack and Hot Press Package	11
3	Hot Press Stack	12
4	Graphite Punch	14
5	Hot Press Package	15
6	Hydraulic Press	17
7	Hydraulic Press Support Table	19
8	The Hydraulic Press Carriage	21
9	Hydraulic Flow Circuit	25
10	Electrical Control Panel	27
11	Hot Press Stack	39
12	Discretization Mesh for the Finite Element Model of the Induction Hot Press Stack	40
13	FEM Mesh for the Hot Press Stack with Node Numbers Specified Along with Dimensions	42
14	Diagram of Section AA of the Graphite Die with Thermocouple Locations Specified	43

LIST OF FIGURES

<u>FIGURE</u>		<u>PAGE</u>
15	Diagram of Section BB of the Graphite Die with Thermocouple Locations Specified	44
16	Finite Element Mesh of the Induction Hot Press Stack With Thermocouple Locations Specified	45
17	The Heat Generation Term as a Function of Position in the Graphite	49
18	FEM Model Element Designations	50
19	Master Element Nodal Numbering Sequence	62
20	Induction Press with Insulation Configuration Set 1	68
21	Induction Press with Insulation Configuration Set 2	69
22	Tungsten-5% Rhenium/ Tungsten-26% Rhenium Thermocouple EMF-vs-Temperature Plot with a Second Order Best Fit Regression Curve	71
23	Boundary Condition Set 1 Temperature-vs-Time Plot for Graphite Surface Temperatures	77
24	Boundary Condition Set 1 Temperature-vs-Time Plot for Graphite Internal Temperatures	78
25	Boundary Condition Set 2 Temperature-vs-Time Plot for Graphite Surface Temperatures	86

LIST OF FIGURES

<u>FIGURE</u>		<u>PAGE</u>
26	Boundary Condition Set 2 Temperature-vs-Time Plot for Graphite Internal Temperatures	87
27	Temperature-vs-Graphite Die Height for Insulation Configuration Set 1 . . .	92
28	Temperature-vs-Graphite Die Height for Insulation Configuration Set 2 . . .	97
29	Postdot Temperature Isothermal Contour Plot for Insulation Configuration Set 1	103
30	Postdot Temperature Isothermal Contour Plot for Insulation Configuration Set 2	104
31	Magnetic Field Lines in a Solenoid . . .	116
32	Magnetic Field Lines in a Solenoid With Material Inserted into It	117
33	Induced Eddy Currents in a Solenoid . . .	121
34	Conduction Through an Infinite Plane Wall	138
35	Temperature-vs-Width for an Infinite Plane Wall under Steady State Conditions	140
36	Steady State Conduction Through an Infinite Composite Wall	142
37	Temperature-vs-Width for a Steady State Infinite Composite Wall	144
38	Heat Generation in an Infinite Composite Wall	146

LIST OF FIGURES
(continued)

<u>FIGURE</u>		<u>PAGE</u>
39	Temperature-vs-Width for a Steady State Infinite Plane Wall with Heat Generation	148
40	Heat Generation in an Infinite Composite Cylinder	150
41	Heat Generation in an Infinite Composite Cylinder	152
42	Load Cell Stress-Strain Curve used in the Hydraulic System Calibration of the Hot Press	161
43	Certificate of Conformance for Grade 8 Bolts Used in the Hydraulic Press Construction	162
44	Block Diagram of the Induction Hot Press System	165
45	Induction Hot Press System	166
46	Hydraulic Press with Water Cooling Lines	168
47	Generator Control Panel	169
48	Operation Control Panel	172
49	Front View of Hydraulic Press	179
50	Side View of the Hydraulic Press	180
51	Front View of Hydraulic Press without the Hydraulic Cylinder Support Structure	181

LIST OF FIGURES
(continued)

<u>FIGURE</u>		<u>PAGE</u>
52	Side View of the Hydraulic Press without the Hydraulic Cylinder Support Structure	182
53	Hydraulic Press Support Table (Units in Inches)	183
54	Section #1 of the Hydraulic Press Support Table, Material AISI 1020 HR Steel, One Plate Total (Units in Inches)	184
55	Section #2 of the Hydraulic Press Support Table, W 6X25 I-Beam, Four Total (Units in Inches)	185
56	Section #3 of the Hydraulic Press Support Table, Angle Beam L 8X4X1/2, Two Total (Units in Inches)	186
57	Section #4 of the Hydraulic Press Support Table, W 6X25 I-Beam, Four Total (Units in Inches)	187
58	Section #5 of the Hydraulic Press Support Table, Material AISI 1020 HR Steel, Twenty Plates Total (Units in Inches)	188
59	Section #6 of the Hydraulic Press Support Table, W 6X25 I-Beam, Two Total (Units in Inches)	189
60	Section #7 of the Hydraulic Press Support Table, Angle Beam L 4X4X1/2 I-Beam, Four Brackets Totals (Units in Inches)	190
61	The Hydraulic Press Carriage	191

LIST OF FIGURES
(continued)

<u>FIGURE</u>		<u>PAGE</u>
62	Section #1 of the Hydraulic Press Carriage, Material AISI 1020 HR Steel, Four Uprights Total (Units in Inches)	192
63	Section #2 of the Hydraulic Press Carriage, W 6X25 I-Beam, One I-Beam Total (Units in Inches).	193
64	Section #3 of the Hydraulic Press Carriage, Material AISI 1020 HR Steel, One Plate Total (Units in Inches) . . .	194
65	Roller Housing for the Carriage	195
66	Section A of the Carriage Roller Housing, L 2.5X2.5X1/2, Four Beams Total (Units in Inches)	196
67	Section B of the Carriage Roller Housing, Material AISI 1020 HR Steel, Two Total. (Units in Inches)	197
68	Components for Carriage Roller Housing, Material As Specified, Two of Each Component. (Units in Inches)	198
69	Induction Hot Press Top Plate, Material Stainless Steel. (Units in Inches)	199
70	Induction Hot Press Top Plate Ram, Material Stainless. (Units in Inches)	200

LIST OF FIGURES
(continued)

<u>FIGURE</u>		<u>PAGE</u>
71	Top Plate Water Channel Cover Plate, Material Stainless Steel, One Total (Units in Inches)	201
72	Top Plate Ram Guide, Material Stainless Steel, One Total (Units in Inches)	202
73	Induction Hot Press Base Plate, Material Stainless Steel, One Total (Units in Inches)	203
74	Base Plate Water Cooling Channel Ring, Material Stainless Steel, One Total (Units in Inches)	204
75	Base Plate Cylinder Stand, Material Stainless Steel, One Total (Units in Inches)	205
76	Induction Hot Press without Designations	206
77	Induction Hot Press with Induction Stack	207

LIST OF TABLES

<u>TABLE</u>		<u>PAGE</u>
1	Temperature Measurement Data From Insulation Configuration Set 1	72
2	Temperature Measurement Data From Insulation Configuration Set 2	79
3	Surface Temperature Regression Data for Insulation Configuration Set 1	89
4	Surface Temperature Regression Data for Insulation Configuration Set 2	94
5	Error Analysis Data for Insulation Configuration Set 1	99
6	Error Analysis Data for Insulation Configuration Set 2	101
7	Energy Balance Data	107
8	Lotus Spreadsheet for Heat Generation Calculations	157

LIST OF SYMBOLS

A	Cross sectional area of graphite die, m^2
A_1	Induction coil resistance divided by N^2 , Ohms
A_2	Graphite die resistance divided by N^2 , Ohms
A_3	Induction coil resistance divided by N^2 , Ohms
A_4	Induction coil resistance divided by N^2 , Ohms
A_5	Air gap reactance divided by N^2 , Ohms
B	Magnetic induction vector, T, H A/ m^2
b_1	Induction coil inside diameter, m
d_1	Reference depth for inductor coil, m
d_2	Reference depth for graphite die, m
C_p	Specific heat at constant pressure, J/kg K
E	Electric intensity, V/m
\dot{E}_{gen}	Rate of energy generation in a control volume, W
\dot{E}_{inflow}	Rate of energy into a control volume, W
E_L	Voltage across induction coils, V
\dot{E}_{out}	Rate of energy out of a control volume, W
\dot{E}_{st}	Rate of energy stored in a control volume, W
FS	Factor of safety
Gr_L	Grashof number
h	Convection heat transfer coefficient, W/ m^2 K
g	Acceleration of gravity, m/s^2

LIST OF SYMBOLS
(continued)

H	Magnetic intensity vector, A/m
H_o	Magnetic Intensity just outside the die, A/m
HP	Horse power
J	Current density vector, A/m ²
k	Thermal conductivity, W/m K
L	Axial height of graphite die
M	Magnetic moment per volume, A m ² /m ³
N	Number of induction coil turns
n	N per unit length of coil, m ⁻¹
Nu_L	Nusselt number
P^-	Power dissipated in the die per unit height, W/m
P_L	Power dissipated in the graphite die, W
Pr	Prandtl number
P_s	Power at the induction terminals, W
RPM	Revolutions per minute, s ⁻¹
R_o	Cylinder radius, m
R	Electrical resistance, Ohms
Ra_L	Rayleigh number
s	Induction penetration term, m
r, ϕ , z	Cylindrical coordinates
T_{inlet}	Inlet cooling water temperature, K

LIST OF SYMBOLS
(continued)

T_{outlet}	Outlet cooling water temperature, K
T_s	Surface temperature of the quartz cylinder, K
T_∞	Temperature at infinity, K
Q	Mass flow rate of cooling water, kg/s
$Q(r)$	Heat generation function, W/m ³
q''_x	Heat Flux, W/m ²
q	Rate of energy generation per unit volume, W/m ³
q_{cyl}	Total rate of energy loss from quartz cylinder, W
q_{cooling}	Total rate of energy loss from cooling water, W
q_{gen}	Total rate of energy generation in graphite die, W

Greek and Scripted Letters

α	Space factor for the induction coil, m
α	Thermal diffusivity, m ² /s
β	Volumetric thermal expansion coefficient, K ⁻¹
\mathcal{E}	Electromagnetic force (EMF), V
μ_0	Permeability of free space, H/m
ν	Kinematic viscosity, m ² /s
ρ	Mass density, kg/m ³
ρ	Electrical resistivity, Ohms m/m ²

LIST OF SYMBOLS
(continued)

ρ_1	Electrical resistivity of coil, Ohms m/m ²
ρ_2	Electrical resistivity of die, Ohms m/m ²
η	Systems induction heating efficiency
σ	Graphite die's electrical conductivity, m/Ohms
σ	Compressive stress, N/m ²
ϕ_m	Magnetic flux, weber (Wb), T m ² , H A
χ_m	Magnetic susceptibility
τ_{max}	The maximum shearing stress, N/m ²

ACKNOWLEDGMENTS

I would like to thank the Coors Ceramic Company for supporting this work through the Colorado Center for Advanced Ceramics. The hydraulic system and vacuum pump were purchased with funds provided by the Colorado Advanced Materials Institute through the Engineered Materials Processing Center.

I would like to thank Dr. Robert Hansen for his consulting on the hydraulic press design and for fabricating the calibration load cell for the hydraulic system.

I would like to thank Dr. David Munoz for his heat transfer consulting. I would to thank Dr. Robert Frost for reviewing this thesis, and Dr. Chester Van Tyne for assistance with the finite element aspects of this project and the help with the use of the MechMet Research Network.

I would like to thank Dr. Gerald DePoorter for the opportunity to continue my academic career at the Colorado Center for Advanced Ceramics and for being my advisor. He has been an excellent example of professionalism.

I would like to thank Nagendra Palle for the assistance he has given me over the last two years on this project.

Finally, I would like to thank my beloved Heidi for her love and support in helping me through the most difficult period of my life. I dedicate this work and my life to her.

CHAPTER I

INTRODUCTION

1.1 Introduction

The scope of this project is to develop induction hot pressing capabilities in the Colorado Center for Advanced Ceramics (CCAC). The intention is to be able to duplicate production cycles on a laboratory scale for investigating and developing a basis for processing parameters. The experimental parameters to be measured and modeled are temperature and stress distribution in the material being processed. From this detailed information on temperature and stress distributions during pressing, production cycles can be obtained. Determining temperature distributions is the emphasis of this work.

1.2 Aim of the Present Work

The objectives for this project were to design and construct an induction hot press and to determine the temperature profile within the hot press die.

The induction hot press system consists of several components:

- 1) Hot press stack and package,

- 2) The hydraulic press and hydraulic system,
- 3) Radio frequency generator and induction coil,
and,
- 4) Vacuum system.

The hydraulic press and hydraulic system provide the pressing force to be applied to the hot press stack. The hot press stack consists of the graphite die and punches. The hot press package encases the hot press stack and provides either a vacuum or controlled atmosphere for the graphite die as well as providing a means of transmitting the force to the stack. The hot press package also provides support for the induction coil. Figure 1 is a block diagram showing the positioning of these various components in the laboratory and indicates utility requirements.

The first step in this project was to design, construct or buy, and assemble all of the components of the induction hot press system described above. Simultaneously, the problem of calculating the temperature profile in the graphite die of the hot press stack was addressed.

Calculating the temperature profile in the hot press stack consisted of constructing a numerical model of the system with experimental verification. Temperatures were calculated using finite element method (FEM) techniques. These temperatures were then compared to experimental data.

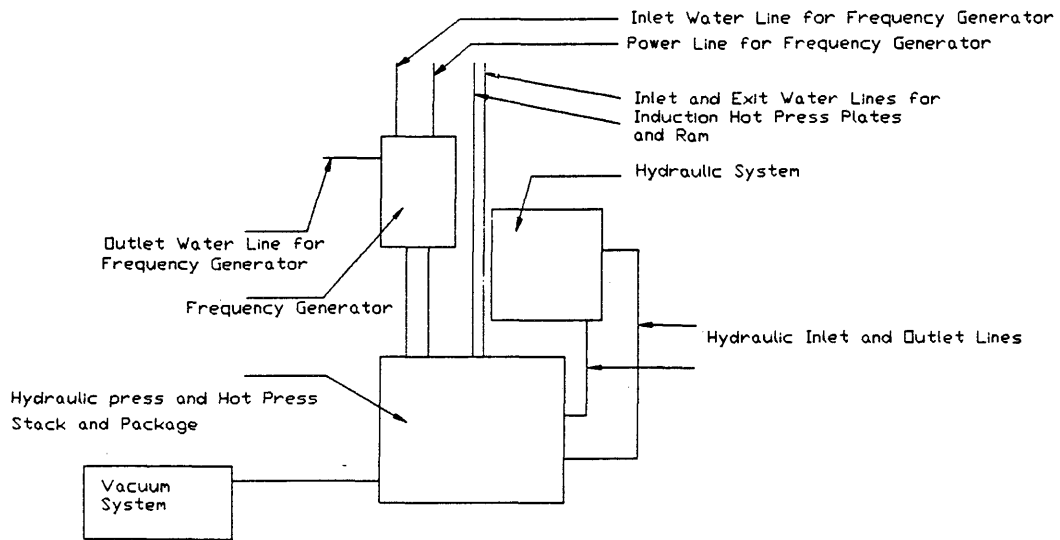


Figure 1 Block Diagram of the Induction Hot Press System

1.3 Outline of Presentation

A literature survey discussing the subject of induction heating is the first topic presented.

Next an overview of the induction hot press system design and construction is given. Yield criteria of loaded members and schematics of the electrical and hydraulic systems are provided.

An energy balance in the system is developed which is designed as a verification of the numerical model. This energy balance includes the heat generation term, water cooling heat losses, radiative heat loss and convective heat loss. Each of these components have been treated in detail for the verification of the finite element model. A detailed development of the finite element model is then presented. It includes the formulation of the heat diffusion equations, the geometry of the model, and boundary conditions. It has a section on material properties and method of verification. It also discusses the finite element code used in this analysis and provides sample input for examples.

A discussion of the results from the modeling and experiments compares the predicted temperature profile to the measured profile. This section is followed by a summary and the conclusions of this research.

CHAPTER II
BACKGROUND AND LITERATURE SURVEY

2.1 Relevance and Application to this Work

The importance of finite element modeling is that complicated problems that do not have closed form analytical solutions can be analyzed. Induction heating has been heavily studied for over 70 years. It is used in many industrial applications ranging from heat treating steel components to hot pressing. It is a cost effective method of energy deposition. The first types of models dealt with describing the resistivity ratios of AC to DC in terms of Bessel functions. Because of the complexity of the heat generation term, approximations are made for special cases. In these cases, the heat generation term is modeled with an exponential curve as a function of skin depth. As finite element methods became popular, modeling of magnetic fields became easier. The result is that fewer assumptions have to be made and a greater variety of problems can be solved. Eddy current calculations became feasible in complicated geometries.

This project uses the Bessel function solution to determine the heat generation and numerical integration in the calculation of a temperature profile. It combines

established principles from electricity and magnetism with new computational methods for modeling an established process with a higher degree of accuracy than previously possible.

This chapter presents the development of induction heating. This development has ranged over 70 years and has incorporated many analytical and numerical techniques. In addition, this chapter presents a discussion on how previous work was used in this analysis.

2.2 Classical Approach to Induction Heating Problems

One of the earliest works is by H. B. Dwight (1) where he presented a method for calculating the skin effect resistance ratios of an inductively heated tube. The resistance ratio is the AC resistance divided by the DC resistance. This is a normalizing method of measuring the variation in induction heating in a body. This variation in induction is known as the skin effect. After several more papers, H. B. Dwight (2) presented a solution to skin effect in isolated tubes in the form of Bessel equations. N. R. Stansel (3) presented a graphical representation of the magnetic flux distribution in a solid iron core for constant frequencies. It illustrated that as the frequency increases, the effective distribution of the magnetic flux

becomes less uniform and more intense at the surface of the core. As the magnetic flux changes distribution, it causes the current density to change its distribution. The shape of this distribution is similar to an exponential decay as a function of skin depth. J. Greig (4) modeled an infinite cylinder as series of cylindrical shells where the current density in any one shell is considered uniform. The thickness of these shells is calculated by a penetration formula. The Bessel function solutions are approximated by sine functions. R. M. Baker (5) presents graphical solutions for the calculation of the heat generation term in a inductively heated infinite cylinder of non-magnetic material. H. F. Storm (6) approximated the heat generation term in an infinite cylinder with an exponential curve as a function of the radial direction. His formulation is based upon vector analysis of a uniform magnetic field. This is the first time that the heat generation is considered quantitatively. The uniform magnetic field assumption is a commonly applied criteria for the partial differential equation analysis using Bessel functions. Another criteria is that the penetration term must be small in comparison to the radius of the charge. If the depth of the penetration is 5% of the radius then this approximation is within 3.6% of the evaluation by Bessel functions. The graphical

solution to the heat generation term as analyzed by Bessel functions is given by N. R. Stansel (7). A detailed treatment of the design and calculation of induction efficiency is given by J. T. Vaughan and J. W. Williamson (8).

2.3 Finite Element Modeling of Magnetic Fields

G. H. Costache (9) constructed a finite element analysis of the induced current density in a nonmagnetic body by a variational formulation of the magnetic vector potential. He then compared his solutions for the real and imaginary components of the current density to analytical solutions for a simple case. M. Fabiano (10) presented the first analysis of the induced electromagnetic fields and eddy current losses in a nonmagnetic conducting cylinder of rectangular cross-section placed in a coaxial finite length circular coil. K. Preis, H. Stogner and K. R. Richter (11) introduced a finite element package for two-dimensional plane and axisymmetric electromagnetic field calculations for nonlinear material properties. Three dimensional field computation is completed using finite element methods by C. W. Trowbridge (12). The topics covered are algorithms for integral and differential methods for solution to three-dimensional magnetostatic

fields. C. W. Trowbridge also provides a brief summary of the work in progress on the solution of three-dimensional eddy currents using differential finite elements. A. Konrad, M. V. K. Chari and Z. J. Csendes (13) discuss new techniques for the analysis of linear, steady-state, skin effect phenomena in multi-conductor systems by finite element method. The first technique is based on a linear superposition principle for the field solution and the second is based on integrodifferential equation field formulation. The calculation of losses in coils carrying alternating currents is discussed by M. G. Reynolds (14). This paper combined analytical expressions and numerical solution using finite element method. By using finite element analysis to model the coil, a magnetic field distribution in the coil is obtained from which the total power per unit length of the load is calculated.

In this analysis, the efficiency calculations from J. T. Vaughan and J. W. Williamson (8) were used to estimate the total amount of heat generated in a graphite die. The heat generation term in the induction process was then derived based upon the estimate total amount of heat being generated in the graphite die.

CHAPTER III

DESIGN AND CONSTRUCTION OF HOT PRESS SYSTEM

3.1 Introduction

The components of the hot press system were listed in Section 1.2. The essence of hot pressing is the simultaneous application of heat and pressure to the ceramic being processed. This is accomplished in the hot press stack which is encased by the hot press package as illustrated in Figure 2. The starting place in the design of the system is the hot press stack.

3.2 Hot Press Stack

Graphite is used for the hot press punch and die material because it couples well with the radio frequency field for heat generation, and it retains its strength at high temperatures. The graphite used had a compressive strength of 26,000 psi (15). Figure 3 shows the location of the graphite punch in the hot press stack.

3.2.1 Design Criteria

The criteria for failure used in this design was the Tresca-Saint Venant yield hypothesis, P. Boresi (16). Using this criteria prevents plastic deformation of the hydraulic press components. This criteria produces a yield

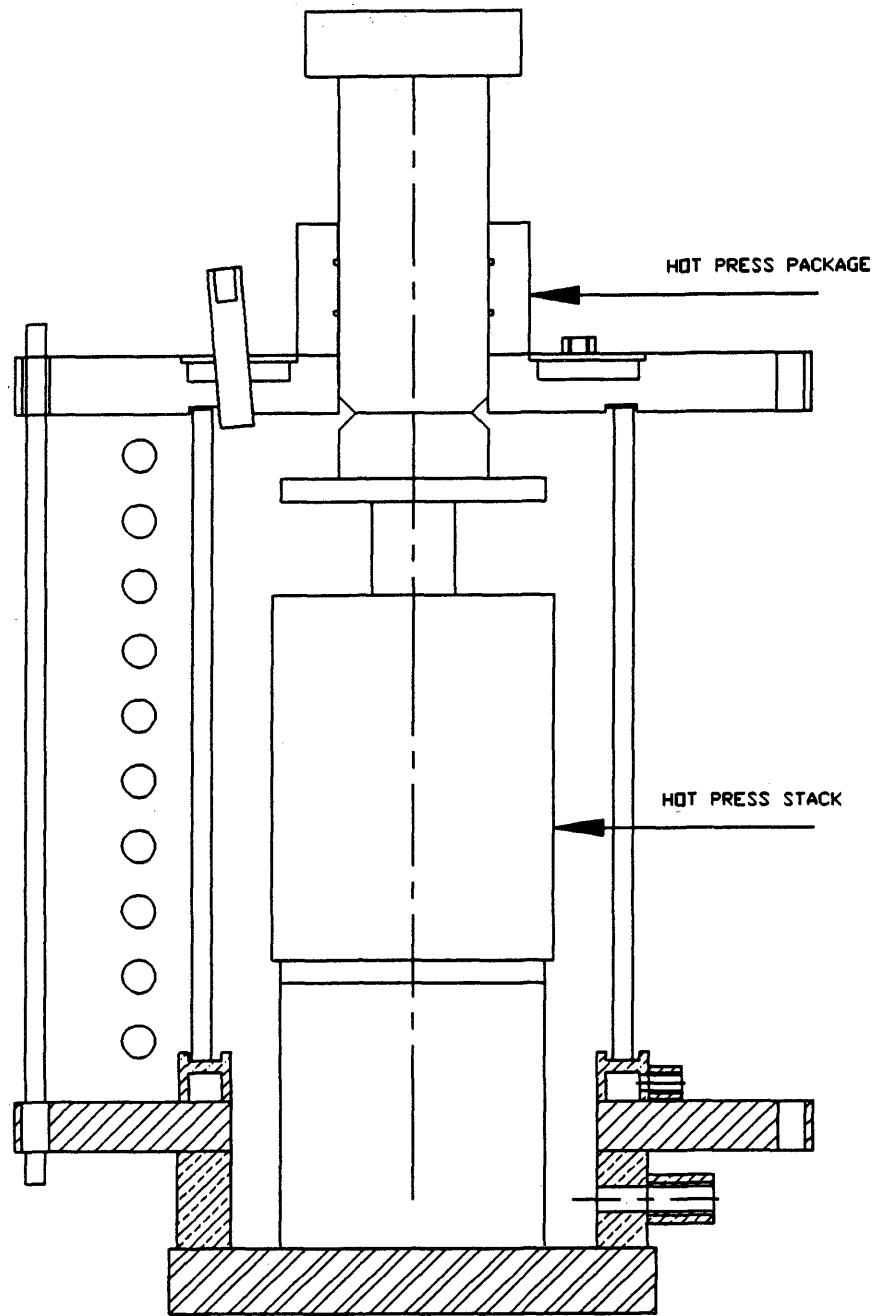


Figure 2 Simplified Model of Hot press Stack and Hot Press Package

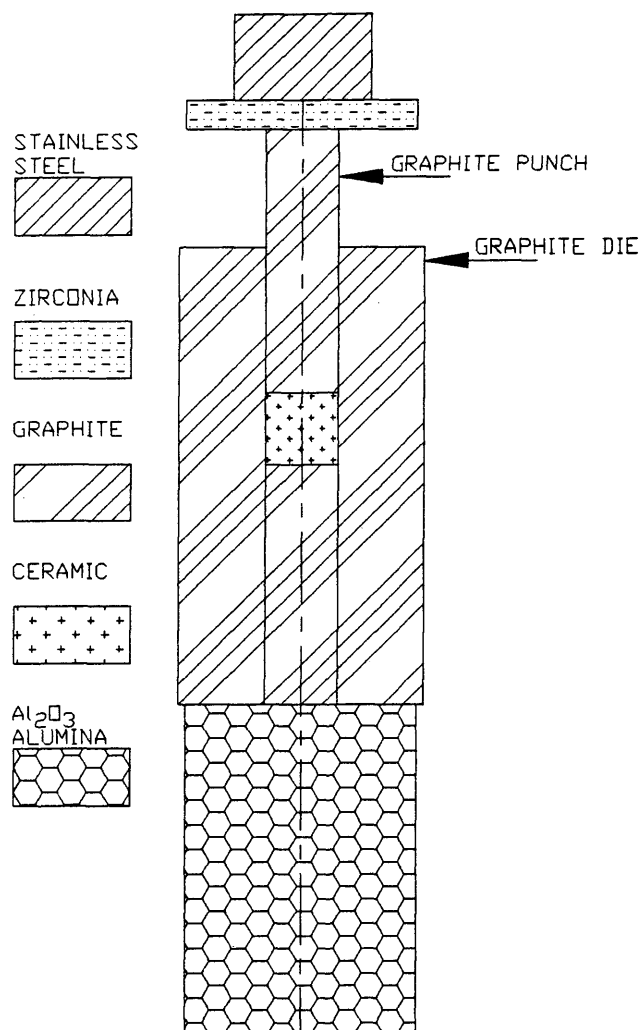


FIGURE 3 Hot Press Stack

locus that is a regular hexagon in the (x,y) plane for a plane stress state. The maximum yield stress criteria predicts failure of a specimen when it is subject to any combination of loads that produces a maximum shearing stress, τ_{\max} , at a point equal to half the uniaxial yield stress, σ_y . The yield stress is a material property that is determined in a compression or tension test. The maximum shearing stress can be calculated for a point by:

$$\tau_{\max} = \sqrt{\left(\frac{\sigma_x - \sigma_y}{2}\right)^2 + \tau_{xy}^2} \quad (1)$$

3.2.2 Graphite Punch

Figure 4 is a free body diagram of the graphite punch. For a punch diameter of two inches and using the yield stress criteria for failure with a working load of 31,000 pounds the factor of safety for yield is 2.6. The actual hot press punch diameter is 1 inch reducing the working load to 7,500 pounds for the same factor of safety.

3.3 Hot Press Package

The hot press package had been designed to facilitate a variety of graphite dies. Figure 5 is a drawing of the hot press package. The hot press package consists of an induction coil, two stainless steel plates, stainless steel

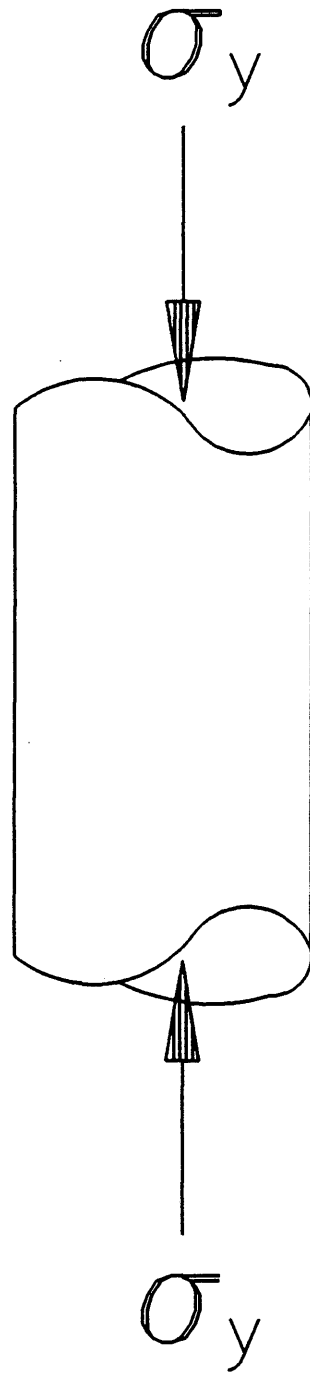


FIGURE 4 Graphite Punch

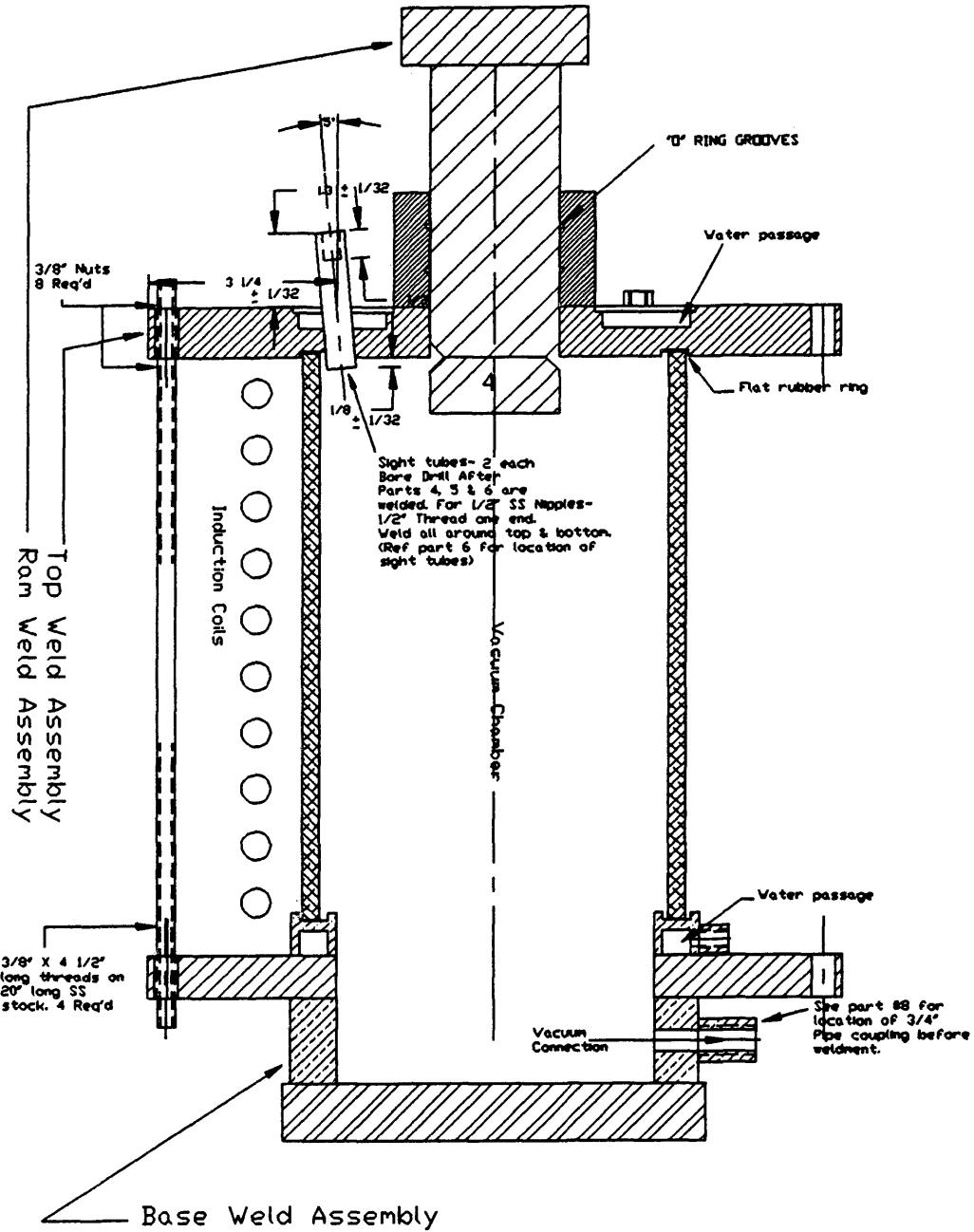


Figure 5 Hot Press Package

ram, quartz tube and a graphite die and punch. The ram transmits the hydraulic load to the graphite punch thereby compressing the ceramic. The coil induces eddy currents in the die producing heat from the I^2R power deposition in the die. This heat is transferred from the die to the surrounding environment of the die. The plates and quartz tube enclose the die in a vacuum, reducing convection to a negligible amount. Radiation shields lining the interior of the quartz tube reduce the power loss due to radiation. The plates are water cooled, as is the ram, subsequently, a large component of the heat loss is due to mass transport in the water cooled channels of these components. To reduce eccentricity between the ram and graphite punch, the ram is aligned with a guide that has two O-rings for maintaining a vacuum. The top plate has provision for an optical pyrometer sight port for measuring a reference temperature on the graphite die. The bottom plate has several ports for a vacuum hose and thermocouples.

3.4 Hydraulic Press

Figure 6 is a drawing of the hydraulic press. The hydraulic press was designed and constructed using the yield stress criteria for failure. The specifications for the hydraulic press were short and long range mobility and a

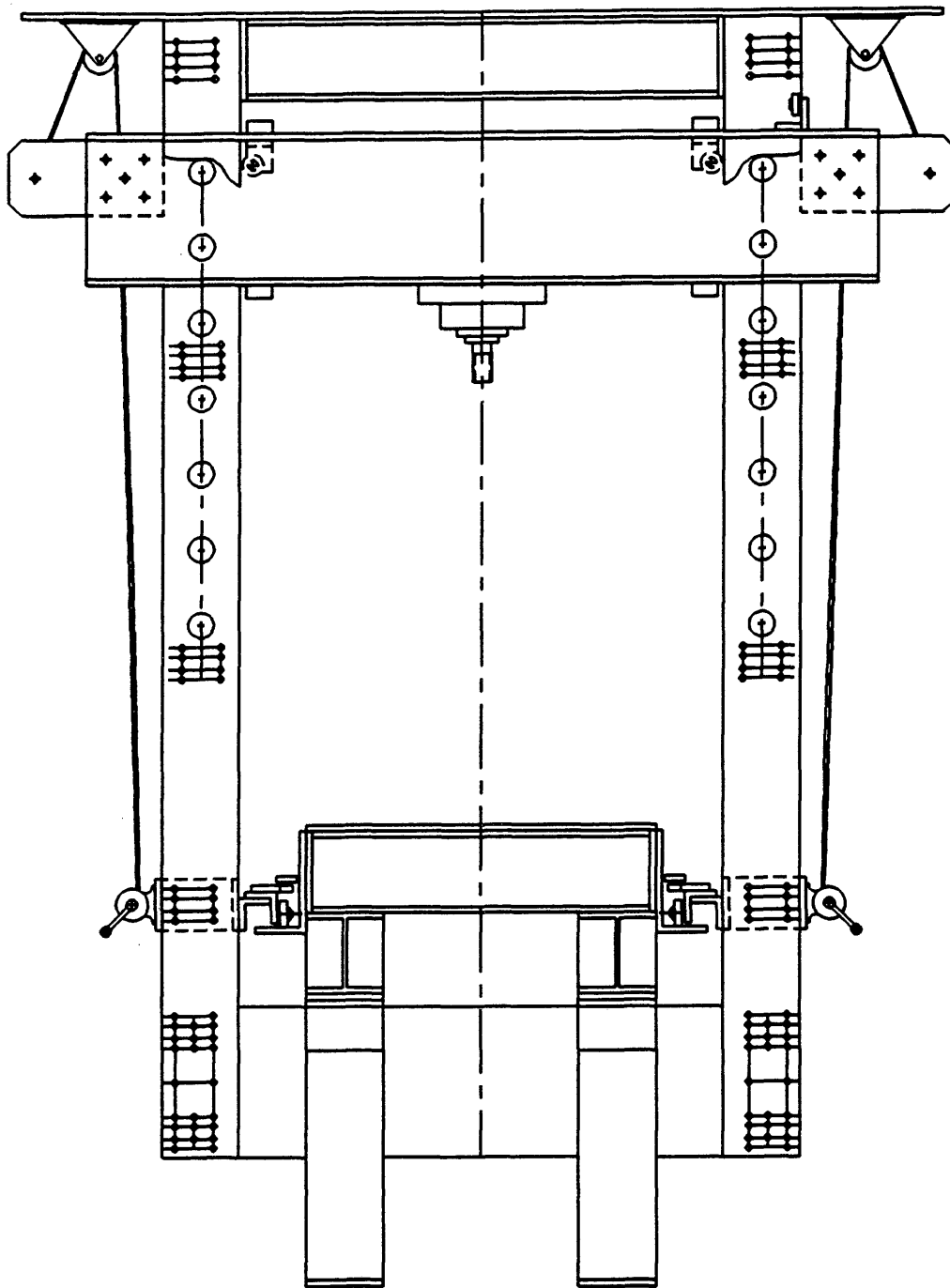


FIGURE 6 Hydraulic Press

required load deliverability. In addition, it had to be of practical size and configuration for laboratory work.

The short range mobility was accomplished by using rollers. The long range mobility was accomplished by making the hydraulic press easy to disassemble. This meant that bolts were extensively used. Appendix V has Documentation that was procured insuring the quality of the grade 8 bolts used in the hydraulic press. The hydraulic press was designed for a working load defined by the graphite punch using yield stress criteria for failure.

3.4.1 Hydraulic Press Support Table

Figure 7 is a drawing of the hydraulic press support table. The hot press rests on this table during operation. The first step in designing this structure was to size the cross beams, Section #2 of Figure 7. It was assumed that the total 31,000 pounds would be supported by one beam and that the steel plate, Section #1 of Figure 7, offered no support. This conservative estimate simplified the calculations substantially. The result was that a W 6X25 I-beam would produce a factor of safety of 2.13. The next step was to check the steel plate, Section #2 of Figure 7, for a load applied between the I-beams. The assumption was made that the plate only transmitted the hydraulic load

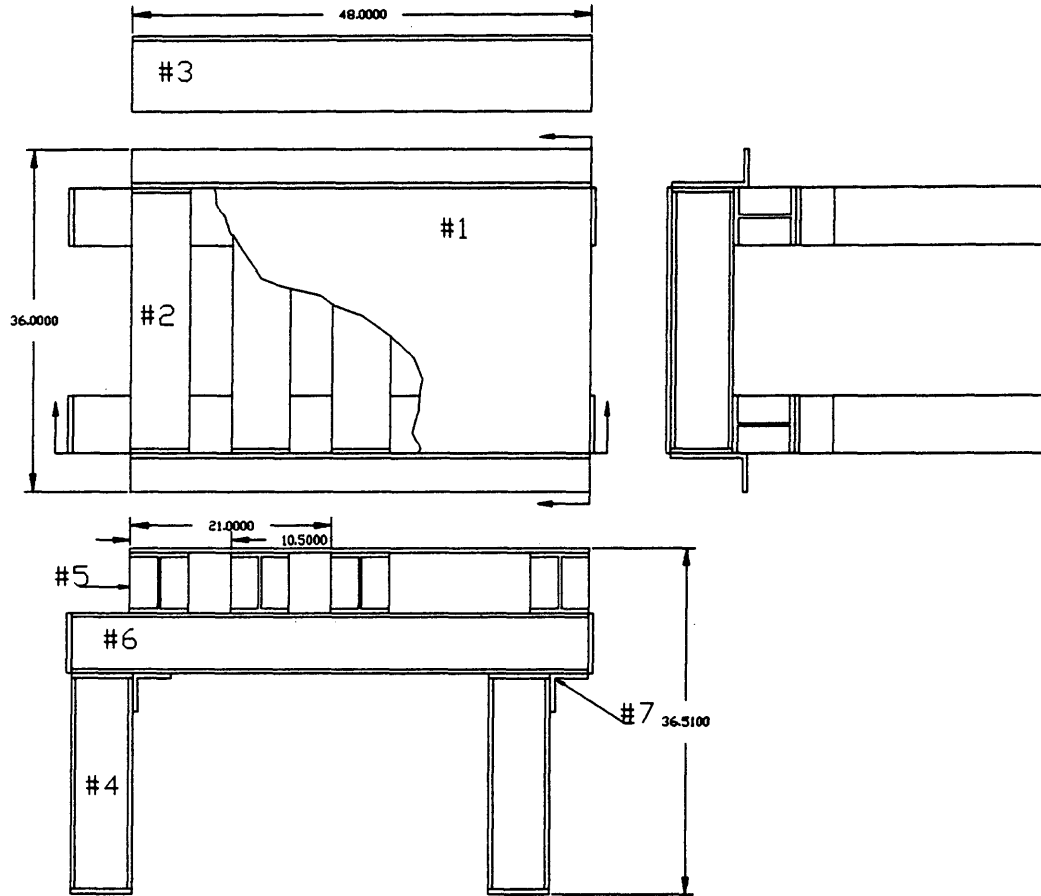


Figure 7 Hydraulic Press Support Table
(units are in inches)

torsionally to the I-beams which resulted in a of 1.3. Since the plate would absorb some of the load this become an acceptable. The rigidity of the I-beams were increased by welding plates, Section #5 of Figure 7, to there ends. This was done in the event of load misalignment. The final check was to assume that the plate was simply supported and was independent of the I-beams. The resulting factor of safety was 3.1. The rest of the base structure was designed with very few additional calculations due to the low stresses being applied.

3.4.2 Hydraulic Press Carriage

Figure 8 illustrates the hydraulic press carriage. It is referred to as the carriage because of its ability to be moved back and forth relative to the support table. An estimated maximum load of 31,000 pounds was used in designing the carriage. This load was applied uniaxially to four reinforced plates with the cross sectional dimensions of 1 inch by 6 inch, Section #1 of Figure 8. The plates were made of AISI HR 1010 steel with a yield strength of 42,000 psi. The resulting factor of safety is 12.3. This included a pin hole concentration factor of 2.6. The non-reinforced Section with cross sectional was analyzed and possessed a factor of safety of 16.

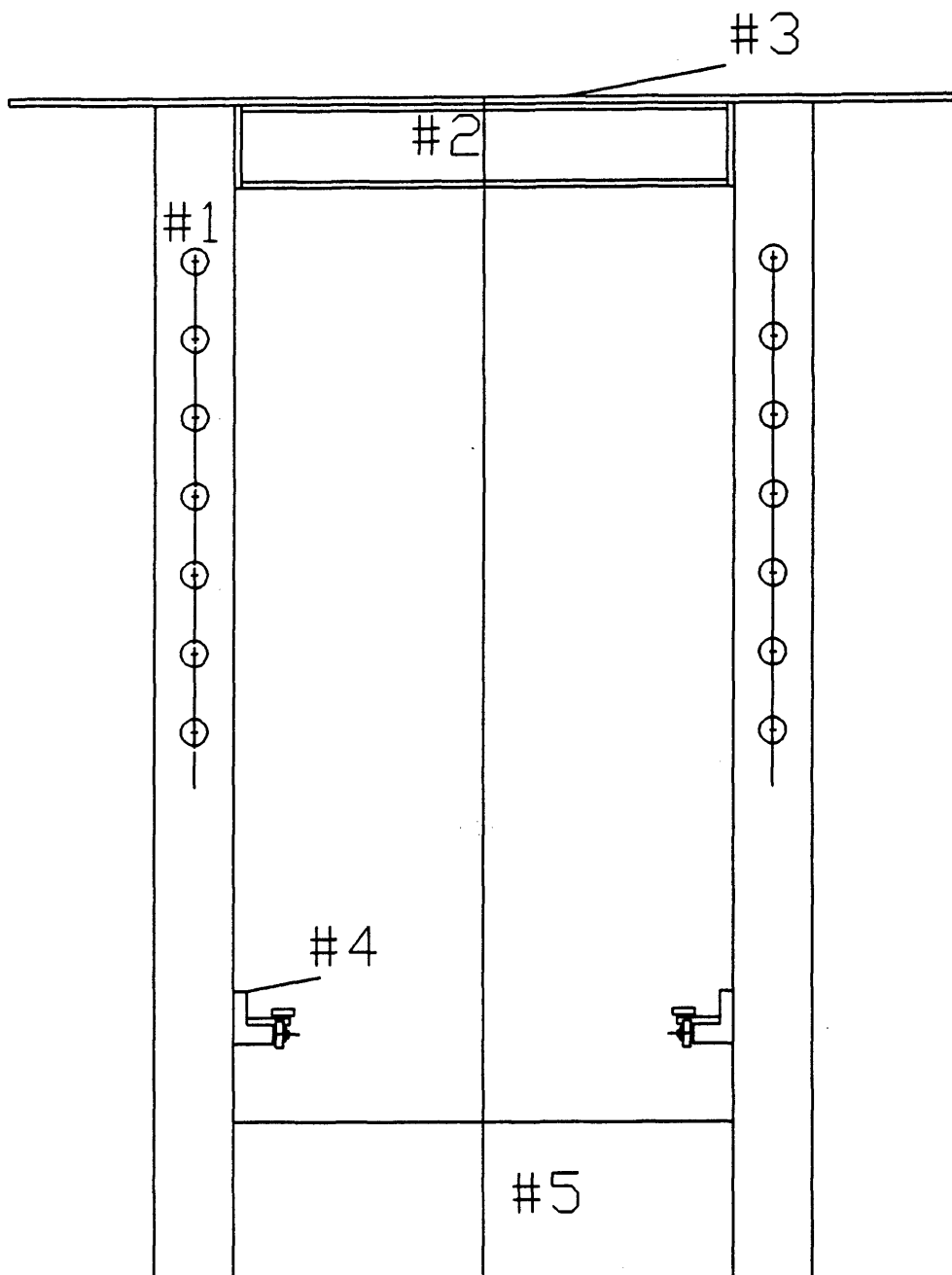


Figure 8 The Hydraulic Press Carriage
(units are in inches)

The tear out at the pins was designed with a method of A. D. Deutscham, W. J. Michels and C. E. Wilson (17) which illustrates how this problem could be modeled as a rivet. The analysis resulted in a factor of safety of 5.4.

The first design of the roller component, Section #4 of Figure 8, required pins, wheels and washers that were to be machined. Dr. Robert Hansen suggested that ball bearings be used as wheels, thereby reducing machining time substantially. The design was checked for tear out at the bolts that held the ball bearings, bolt strength in bending, bearing load capacity, bushing strength under the induced torsional component, shear on the bolts that held the ball bearings, and the compression on the bolts used to raise the carriage and the alignment rollers.

The assumption was made that half of the carriage load would be shared by each roller component. The estimated weight of the carriage was 1000 pounds. The lowest design factor of safety was 2.5.

The last Section of the carriage to be designed was Section #5 of Figure 8. This Section is the cross beams that transferred the hydraulic load from the upright supports to the hydraulic support table. From the support

table, the load is transferred to the induction hot press completing the load loop. The beams were modeled in bending with a resulting factor of safety of 4.3. The grade 8 bolts were treated as rivets and resulted in a factor of safety of 8.3.

3.4.3 Hydraulic Cylinder Support Structure

The hydraulic cylinder support structure was the last feature designed on the hydraulic press. Figure 6 shows how this structure holds the hydraulic cylinder in place. This structure was made of two C 12 inch X 20.7 inch channel beams bolted back to back by four 1 inch X 2 inch sections of stock steel. The hydraulic cylinder was mounted on the under side of the channel beams so that when the cylinder was engaged, the load would not be absorbed by the bolts. The four sections of stock are used to hold the two channel beams together. This ensures that the eccentricity of the structure can be considered negligible. This is accomplished by changing the beams from two independent structures, to one with a center of gravity through the load line. The hydraulic cylinder support structure was attached to the carriage by the use of four steel pins of 1 1/2 inch diameter. The assumption that only two pins would be engage at one time was made and resulted in a factor of safety for

the pins of 3.0 The factor of safety against tear out on the channel beams is 5.4. The channel beams were checked for bending resulting in a factor of safety of 4.0.

3.5 Hydraulic System

The hydraulic flow circuit of this hydraulic system is illustrated in Figure 9. The 5 HP 1200 RPM motor supplies the required hydraulic pressure for displacing the cylinder. The maximum hydraulic pressure is set at 3000 psi which results in applied load of 59,000 pounds. The pressure relief valve is set to 381 psi. This insures that a maximum load of 7500 pounds is delivered to the graphite punch. One of the features of this system is the power supply relief valve that allows modulation of the hydraulic pressure and ultimately, the load to the graphite punch of the induction hot press. The system is equipped with a directional valve that is coupled to a electronic control panel. This allows for displacement control of the cylinder. The flow control module allows for direction independent-displacement rates of the cylinder. The check valve is set for the maximum pressure of the system to insure that the maximum load capacity of the graphite die is not exceeded. The heat exchanger serves to remove excessive power not used in displacing the cylinder. This is very important during the

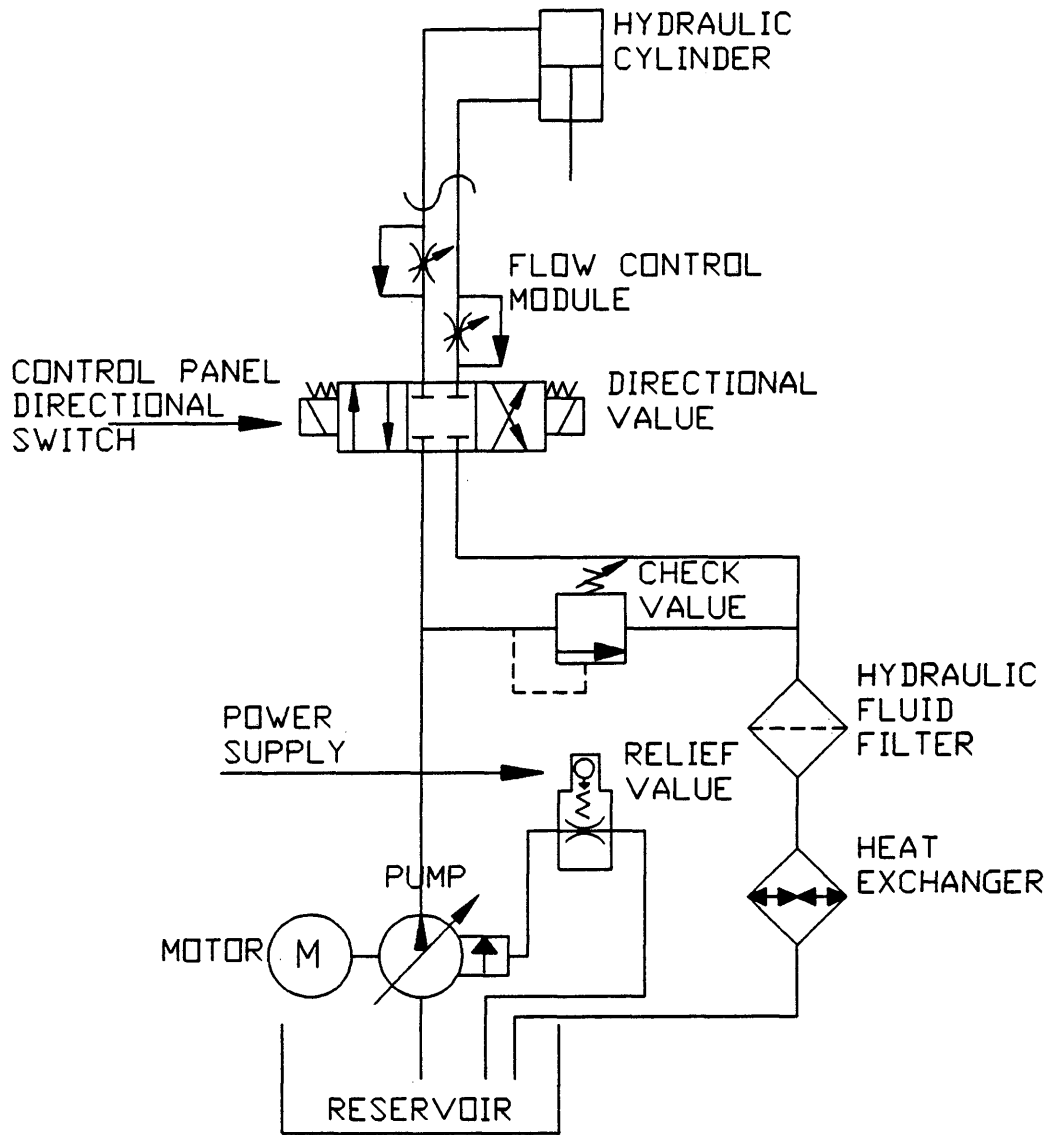


FIGURE 9 Hydraulic Flow Circuit

quasi-static portion of the load cycle in the ceramic densification. The reservoir serves as a retainer for the hydraulic fluid.

3.6 Electrical Schematic

Figure 10 is a schematic of the electronic control panel. The panel was designed to operate the vacuum system, the hydraulic cylinder directional valve, an interlock switch and the pressure control power supply. The interlock switch prevents excessive damage to the induction hot press in the case of punch failure.

3.7 Vacuum System

The vacuum system serves two purposes. The first is to reduce the convection loss from the die to a negligible amount. The second is to prevent oxidation of the graphite die. The system can be operated in vacuum or back filled with inert gas.

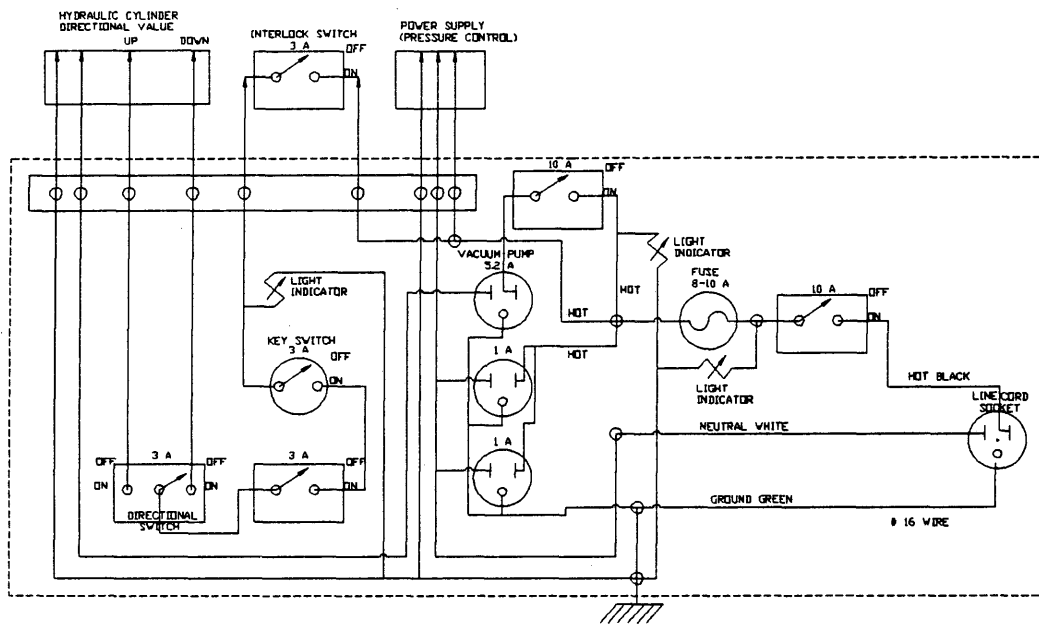


Figure 10 Electrical Control Panel

CHAPTER IV

ENERGY BALANCE IN THE EXPERIMENT

4.1 Introduction

The global energy balance was used as a method of verifying the numerical modeling. The modeling of the induction hot press required an analytical description of the heat generation in the graphite die. The heat generation term was derived from fundamental principles of electricity and magnetism. This term was then incorporated in the finite element model as the forcing function for the model. This analysis is done for steady state so that the heat generated in the system could be equated to the heat losses from the system. These losses are in the form of convection and radiation from the quartz containment cylinder and the heat removed by the cooling water. The water cooled components are the upper and lower stainless steel plates and the stainless steel ram as illustrated in Figure 5.

4.2 The Heat Equation

The heat equation is derived from an energy balance on a differential volume where Fourier's law, Equation (2), describes the heat flux across the surfaces of the volume.

$$q''_x = -k \frac{dT}{dx} \quad (2)$$

q''_x Heat flux in the x direction, W/m²

k Coefficient of conduction, W/m K

T Temperature, C

The first law of thermodynamics states that energy can not be created or destroyed. In other words, energy is conserved. Conservation of energy written in a time differential form is

$$\dot{E}_{inflow} + \dot{E}_{gen} - \dot{E}_{out} = \dot{E}_{st} \quad (3)$$

\dot{E}_{inflow} Power into the control volume, W

\dot{E}_{gen} Power generated in the control volume, W

\dot{E}_{out} Power out of the control volume, W

\dot{E}_{st} Power stored in the control volume, W

This equation states that the heat inflow into a control volume along with the heat generated in that volume equals the out flow of heat from that volume and the heat stored in that volume. Applying these equations to a cylindrical coordinate system the diffusion equation can be derived.

$$\rho C_p \frac{\partial T}{\partial t} = \frac{1}{r} \frac{\partial}{\partial r} \left(kr \frac{\partial T}{\partial r} \right) + \frac{1}{r^2} \frac{\partial}{\partial \phi} \left(K \frac{\partial T}{\partial \phi} \right) + \frac{\partial}{\partial z} \left(k \frac{\partial T}{\partial z} \right) + \dot{q}(r) \quad (4)$$

r, ϕ, z	Cylindrical coordinates
ρ	Density, kg/m ³
C_p	Specific Heat for constant pressure, J/kg K
$\dot{q}(r)$	Heat generation as a function of radius, W/m ³

For the steady state solution with axisymmetry, the heat diffusion equation can be written as a two dimensional differential equation with heat generation.

$$\frac{1}{r} \frac{\partial}{\partial r} (kr \frac{\partial T}{\partial r}) + \frac{\partial}{\partial z} (k \frac{\partial T}{\partial z}) + \dot{q}(r) = 0 \quad (5)$$

4.3 The Total Heat Generated in the System

In Appendix I it is shown that the magnetic intensity in a cylindrical charge placed in a magnetic field can be written in the form of Bessel's equation.

$$\frac{d^2 \mathbf{H}}{dr^2} + \frac{1}{r} \frac{d\mathbf{H}}{dr} - \frac{2i\mathbf{H}}{S^2} = 0 \quad (6)$$

\mathbf{H}	Magnetic intensity vector, A/m
S	Induction penetration term, m
i	Square root of minus one

The solution to this equation is written in the form of the Bessel real, ber, and Bessel imaginary, bei, terms.

$$\mathbf{H} = A [ber(\frac{\sqrt{2}r}{S}) + ibei(\frac{\sqrt{2}r}{S})] \quad (7)$$

The electric intensity can be found by differentiating

the magnetic intensity with respect to the radius and using surface boundary condition to evaluate the proportionality constant A, as shown in Appendix I. The surface boundary condition is the assumption that the magnetic intensity just outside the surface is equal to the magnetic intensity just inside the surface of the graphite die. The absolute value of the electric intensity then becomes

$$E = \left[\frac{-\sqrt{2} 2 H_o}{\sigma S} \right] \sqrt{\frac{[ber(\frac{\sqrt{2}r}{S})]^2 + [bei(\frac{\sqrt{2}r}{S})]^2}{[ber(\frac{\sqrt{2}a}{S})]^2 + [bei(\frac{\sqrt{2}a}{S})]^2}} \quad (8)$$

The power induced in the load per unit volume as a function of position can be found by

$$\dot{q}(r) = E^2 \sigma \quad (9)$$

σ Electrical conductivity, 1/(Ohms m)

The total power generated in a body can be found by integrating the heat generation function over the volume of that body.

$$Q_{gen} = \int_{r=0}^{r=a} E^2 \sigma L 2 \pi r dr \quad (10)$$

4.4 The Heat Convected from the Quartz Containing Vessel

The heat loss due to free convection from the quartz tube represents a fraction of the total heat loss in the system. This value can be summed with the other heat losses to verify the calculation of the total power dissipated in the graphite die. This is important because the total power dissipated in the system was used in calculating the heat generation term. The first number that needs to be calculated is the Rayleigh number

$$Ra_L = \frac{g\beta (T_s - T_\infty) L^3}{\nu \alpha} \quad (11)$$

g	Acceleration of gravity, m/s ²
β	Volumetric thermal expansion coefficient, K ⁻¹
L	Cylinder length, m
T	Temperature, C
ν	Kinematic viscosity, m ² /s
α	Thermal diffusivity, m ² /s

The volumetric thermal expansion coefficient for constant pressure is defined as

$$\beta = -\frac{1}{\rho} \left(\frac{\partial \rho}{\partial T} \right)_P \quad (12)$$

Since this free convection is for the outside surface of the quartz cylinder, the air can be assumed to be a perfect gas.

For a perfect gas, the expansion coefficient simply becomes the inverse of the absolute film temperature. The film temperature is the average between the surface temperature and the temperature at ambient. The Rayleigh number can also be expressed as

$$Ra_L = Gr_L Pr \quad (13)$$

Pr Prandtl number
 Gr_L Grashof number

The Grashof number is the ratio of buoyancy to viscous forces. This dimensionless number serves the purpose in natural convection that the Reynolds number serves in forced convection. This number allows the prediction of laminar or turbulent flow. F. P. Incropera and D. P. DeWitt (18) state that for cylinders, the vertical wall assumption can be used, if the boundary layer thickness is much less than the cylinder diameter. This is satisfied when

$$\frac{D}{L} \geq \frac{35}{Gr_L^{1/4}} \quad (14)$$

D Cylinder diameter, m
 L Cylinder length, m

Once this condition is met, the Rayleigh number is calculated. Then the Nusselt number can be calculated by

$$\overline{Nu}_L = 0.68 + \frac{0.67 Ra_L^{\frac{1}{4}}}{[1 + (\frac{0.492}{Pr})^{\frac{9}{16}}]^{\frac{4}{9}}} \quad (0 < Ra_L < 10^9) \quad (15)$$

This parameter is equal to the dimensionless temperature gradient at the surface and provides a measure of convection heat transfer occurring at the surface. The average convection coefficient defined as

$$\bar{h} = \frac{\overline{Nu}_L k}{L} \quad (16)$$

The total heat convected from the surface of a vertical wall is

$$q_{vw} = A\bar{h}(T_s - T_\infty) \quad (17)$$

For the case of a vertical cylinder that does not match the criteria given in equation (14), the total heat flux due to convection can be adjusted for the nonsimilarity. A local nonsimilarity solution method has been outlined by Minkowycz & Sparrow (19). This method gives numerical approximations for the ratio of the Nusselt numbers as an adjustment of the heat flux from a vertical wall, to the heat flux from a vertical cylinder.

$$q_{cyl} = q_{vw} * \left(\frac{\overline{(Nu_x)}_{cyl}}{\overline{(Nu_x)}_{fp}} \right) \quad (18)$$

4.5 The Total Heat Radiated from the System

The radiated heat loss from the quartz cylinder can be calculated using

$$q_{rad} = \sigma \epsilon (T_s^4 - T_\infty^4) \quad (19)$$

ϵ emissivity

σ Stefan-Boltzmann constant

T_∞ Temperature at infinity, C

where the emissivity of graphite is 0.8.

4.6 The Total Heat Removed from the System by Mass Transport

The heat removed by mass transport can be calculated from the change in the cooling water temperature and its mass flow rate (Q).

$$q_{cooling} = Q (T_{outlet} - T_{inlet}) C_p \quad (20)$$

T_{outlet} Final temperature of cooling water, C

T_{inlet} Inial temperature of cooling water, C

There are three locations where heat is removed by mass transport. The first is the stainless steel ram and the other two locations are the stainless steel plates.

4.7 The Energy Balance of the System

The total heat loss from the system should equal the total heat generated in the system. The two losses are the convected and radiated heat from the quartz tube and the heat transported by the cooling water. The summation of these terms should account for most of the heat loss from the system. Since the heat generation term is based on a calculated efficiency of heat dissipation in the graphite die, this is one of the way for verifying the heat generation with experimental data. Therefore, the energy balance of the system can be expressed as

$$Q_{gen} = Q_{cyl} + Q_{cooling} + Q_{rad} \quad (21)$$

The accuracy of this equality will reflect the accuracy of the power efficiency calculations. If the measured power loss is much greater than the assumed heat generation, then a larger value can be assumed for the heat generation. This would increase the accuracy of the heat generation term to be within the experimental error of this model.

CHAPTER V
DESIGN OF THE FINITE ELEMENT MODEL

5.1 Introduction

The Determination of Temperature, Dot, program was developed by Polivka and Wilson (20) at the University of California, Berkeley. The code was designed for the analysis of heat transfer problems. The Dot code models nonlinear, transient and steady state heat conduction with either 2-D planar or axisymmetric elements. It handles material properties as a function of time and temperature. It also models radiation and convection as boundary conditions along with cooling pipes.

Classical problems with closed form solutions were initially analyzed with Dot. The verifications were performed to determine the accuracy of Dot. The verification results are represented graphically by PostDot. The solutions and graphical representations are presented in Appendix II. The Dot results are well within the experimental error of this analysis.

5.2 Geometry of the Finite Element Model

Figure 2 is a drawing of the induction hot press package and stack. The FEM model is used to predicted the temperature distributions in the hot press stack during the

hot pressing process. The stack is composed of various components. Figure 11 shows these components in detail. There is a stainless steel ram, a graphite die and punch, zirconia insulating disk, alumina stand, and the material being formed. The material in this case is ceramic, specifically spinel. The alumina serves as a refractory and as a rigid support for the graphite die.

The purpose of a thermal analysis of the hot press package is to calculate the 2-D temperature profile in the graphite die and the material being pressed. This profile aids in the estimation of the forming temperature of the material being processed in the hot press stack.

Figure 12 is a drawing of the FEM mesh used to model the stack with the hot press stack also shown for reference. This figure illustrates the node locations on the FEM mesh that correspond to thermocouple locations in the graphite die. These locations are designated by letters. This identification is used through out this document.

Two considerations were used in formulating this mesh. The first was to optimize the FEM mesh for full consideration of the material properties and mechanistic processes while minimizing the computation time. The second was to ensure a 7:1 maximum element size ratio. K. J. Bathe (21) states that using this as a maximum ratio will reduce

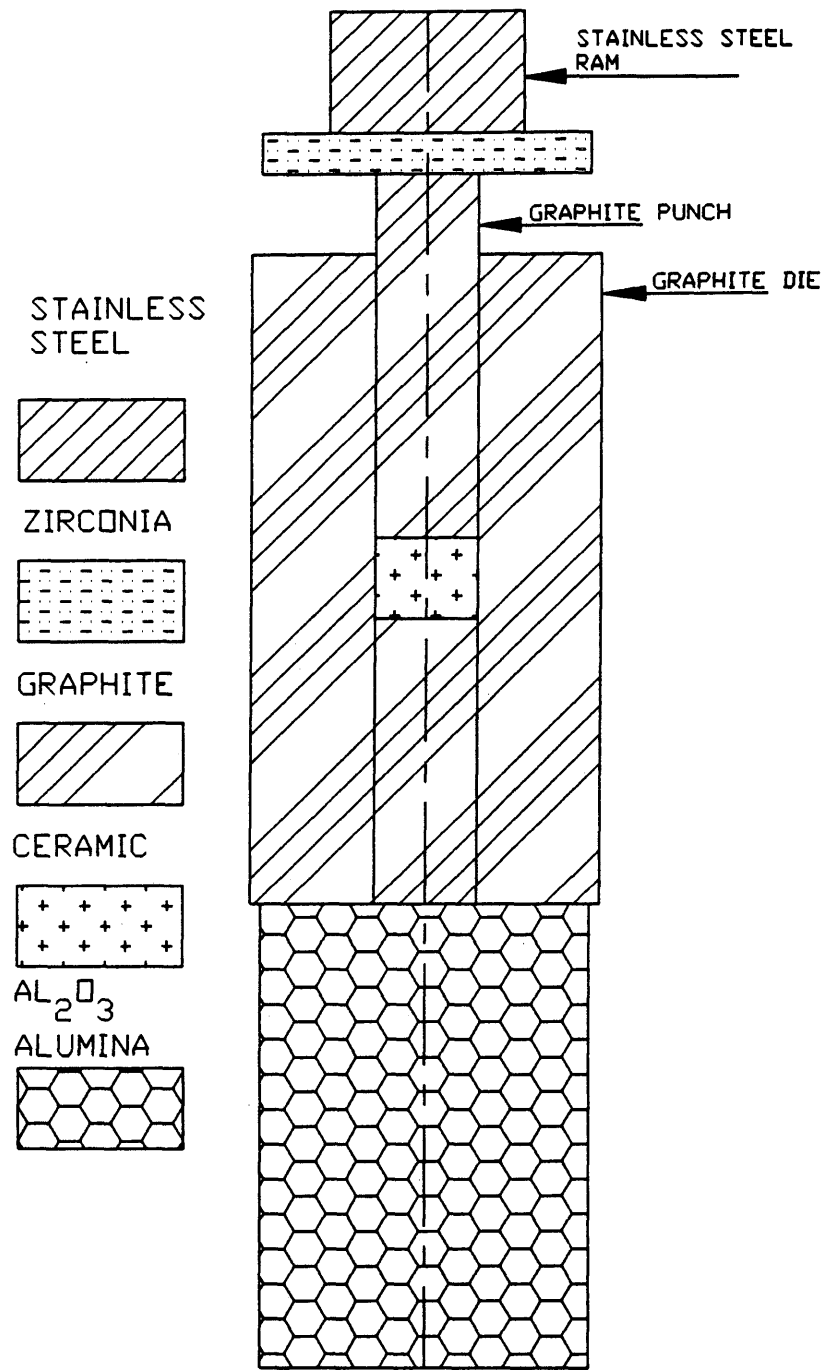


Figure 11 Hot Press Stack

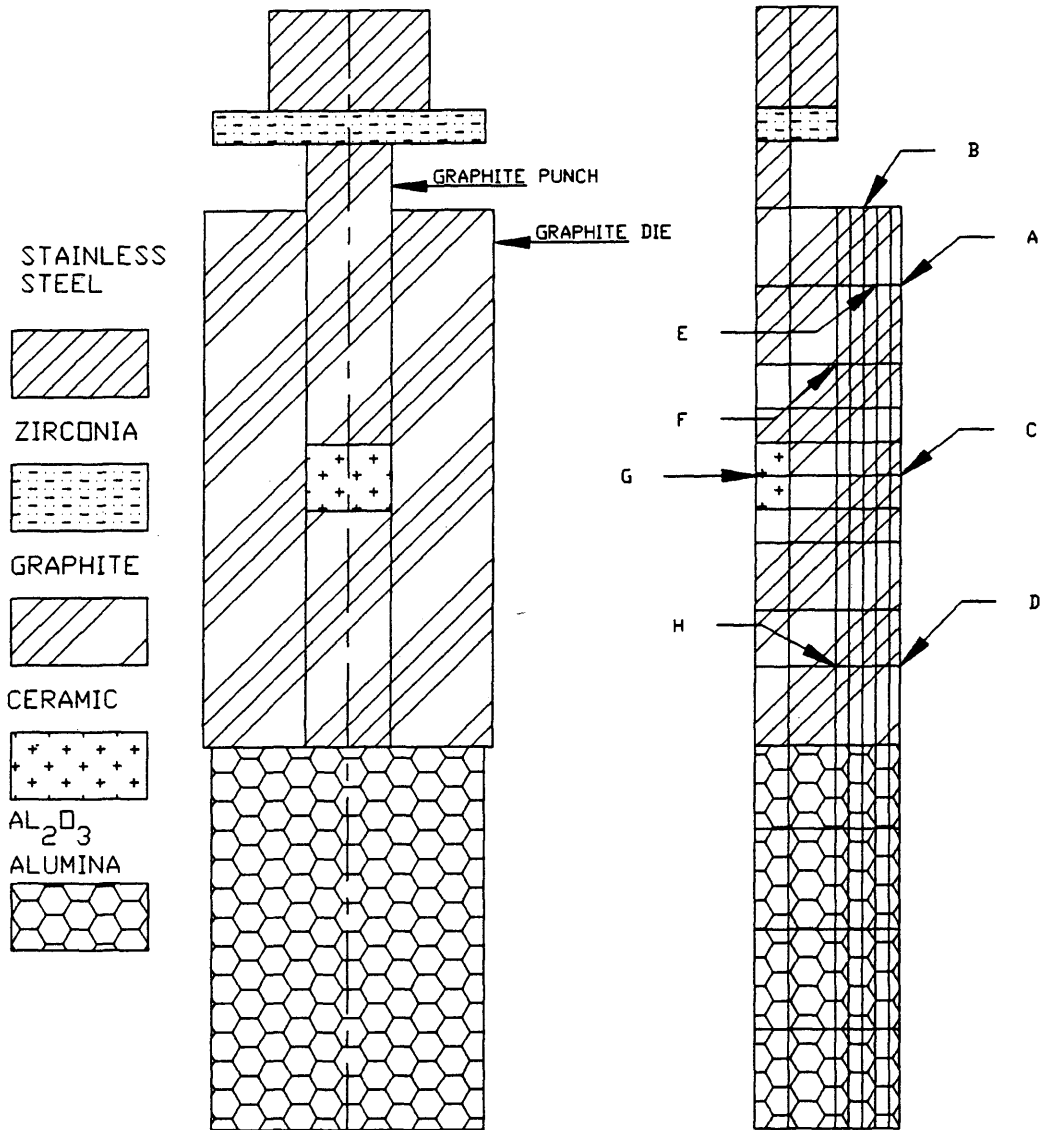


Figure 12 Discretization Mesh for the Finite Element Model of the Induction Hot Press Stack

numerical instabilities. Figure 13 illustrates the numbering of the nodes in this model. The mesh is distorted to show the node numbering and its dimension. To establish boundary conditions for the FEM model, thermocouples were placed on the surface of the hot press stack to measure the axial surface temperature profile. Figures 14 and 15 illustrate the various thermocouple locations. Figure 16 shows the positions of these known temperature points on the FEM mesh.

5.3 Material Properties

The graphite material properties were taken from W. H. Brixius (15). The temperature dependence of the graphite electrical resistivity was investigated for the purpose of calculating an average resistivity value while introducing negligible error.

In the steady state working range of the graphite die, the temperature varies from 1000 °C to 1500 °C. An average resistivity was calculated for this range of values. A value of $1.12 \cdot 10^{-3}$ Ohm-cm was assumed for the graphite resistivity. Because of the small geometry of this model, the unit cm is used to define length dimensions and material properties. The maximum error associated with this assumption is 3.8%. The copper resistivity at room

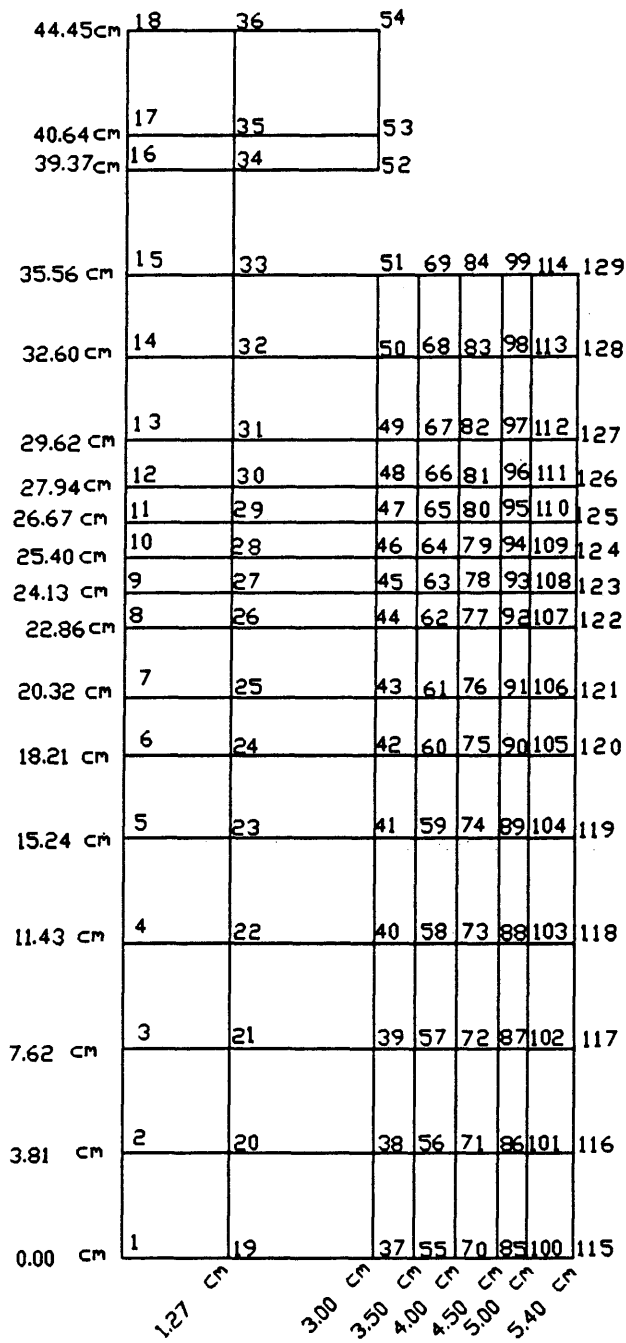


Figure 13 FEM Mesh for the Hot Press Stack with Node Numbers Specified Along with Dimensions

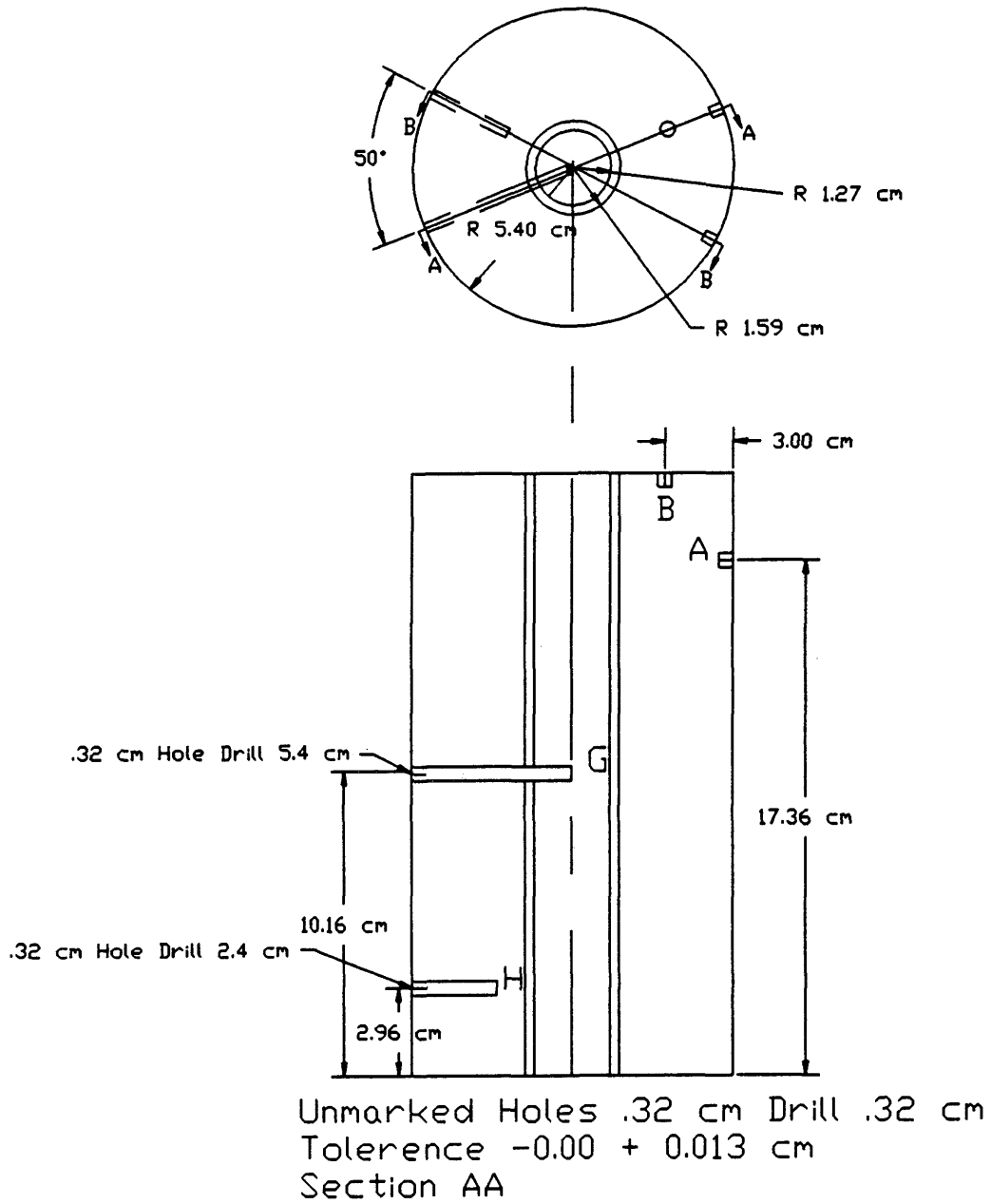


Figure 14 Diagram of Section AA of the Graphite Die with Thermocouple Locations Specified

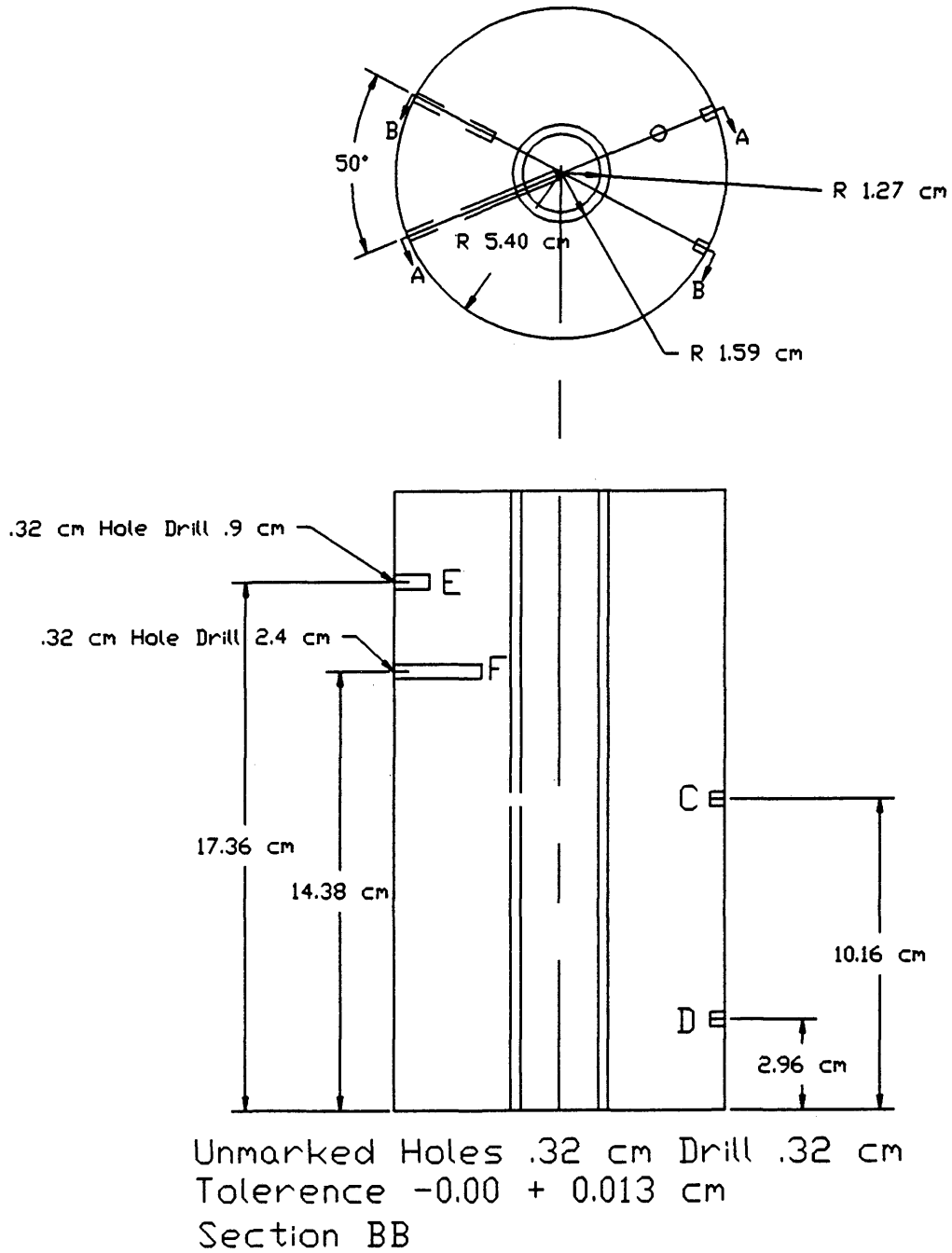


Figure 15 Diagram of Section BB of the Graphite Die with Thermocouple Locations Specified

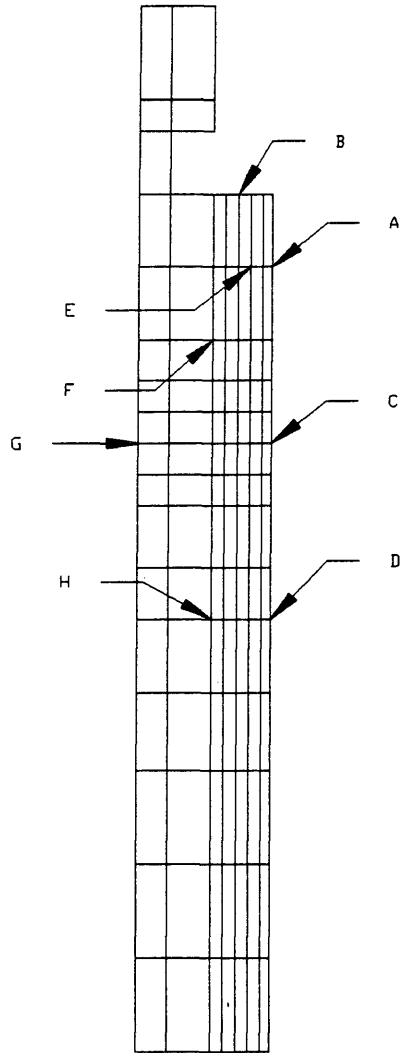


Figure 16 Finite Element Mesh of the Induction Hot Press Stack with Thermocouple Locations Specified

temperature was found in the work of, R. C. Weast, M. J. Astle and W. H. Beyer (22). This value is $1.68 \cdot 10^{-6}$ Ohm-cm. The copper resistivity was only considered at room temperature because the coils are water cooled. These values were used in the efficiency calculations for the power delivered to the load.

The thermal properties of the stainless steel were obtained from F. P. Incropera and D. P. DeWitt (18). The values of $0.25 \text{ W}/(^{\circ}\text{K cm})$ for the thermal conductivity and $0.480 \text{ J}/(\text{g } ^{\circ}\text{K})$ for the heat capacity were assumed.

The C_p and the k of the graphite were estimated the same way as the graphite electrical resistivity. Average values of k and C_p for the graphite were calculated for the temperature range of the graphite in this process. As the temperature range becomes small accuracy of the properties increases. In the limit of an infinitely small temperature range, there would be no approximation error. In this application, the error associated with this approximation is within the experimental error of the system.

The two types of insulating material used in the induction press are zirconia and alumina. The range in the insulation temperatures are small such that average values for the k and the C_p are assumed with negligible error. For the zirconia the k and the C_p are $0.0242 \text{ W}/(^{\circ}\text{K cm})$, and 202

J/(kg °K), (23), and for the alumina the k and the C_p are 0.0627 W/(°K cm) and 244 J/(kg °K), (22).

The hot press can be used to compact a variety of materials. The first to be considered was spinel. The k and C_p for the spinel are 0.03798 W/(K cm) and 175 J/(kg °K), (22).

5.4 FEM Formulation of the 2-D Heat Diffusion Equation

The hot press package was analyzed for an energy dissipation efficiency by means of a Lotus spread sheet which resulted in an efficiency of 0.89. This efficiency is the fraction of the power measured at the induction coil that is dissipated in the graphite die. This is also the fraction of the induction circuit impedance that is due to the graphite electrical resistance. A copy of this spreadsheet is located in Appendix III. The power to the coil for this application is 5000 watts. This results in a power of 4430 watts being delivered to the load. The equation for the heat generation term as a function of position in the die is

$$P = \sigma E^2 \quad (22)$$

σ Graphite conductivity, m/Ohms

E Electric intensity, V/m

The electrical intensity is defined again as

$$E = \frac{\sqrt{2} 2 H_0}{\sigma s} \sqrt{\frac{[\text{ber}'(\frac{\sqrt{2} I}{s})]^2 + [\text{bei}'(\frac{\sqrt{2} I}{s})]^2}{[\text{ber}(\frac{\sqrt{2} a}{s})]^2 + [\text{bei}(\frac{\sqrt{2} a}{s})]^2}} \quad (23)$$

H_0 Magnetic intensity, A/m

s Penetration term, m

The variable H_0 is assumed to have the value of the magnetic intensity just outside the graphite die. The penetration term defined as

$$s = \frac{1}{2\pi} \sqrt{\frac{\rho 10^9}{2\mu\nu}} \quad (24)$$

ρ Graphite density

μ Magnetic permeability

ν Radio frequency

The heat generation, as a function position, has the shape of the smooth curve shown in Figure 17. The step function in Figure 17 is an approximation of the heat generation curve. This step function is incorporated in the numerical model. The area under both curves are within 2.2% of each other. The effect of this approximation is discussed in Chapter 7. Figure 18 illustrates the element numbering of the FEM mesh. The columns of elements in Figure 18 corresponding to the graphite die domain were assigned the

HEAT GENERATION-VS-RADIUS OF GRAPHITE DIE

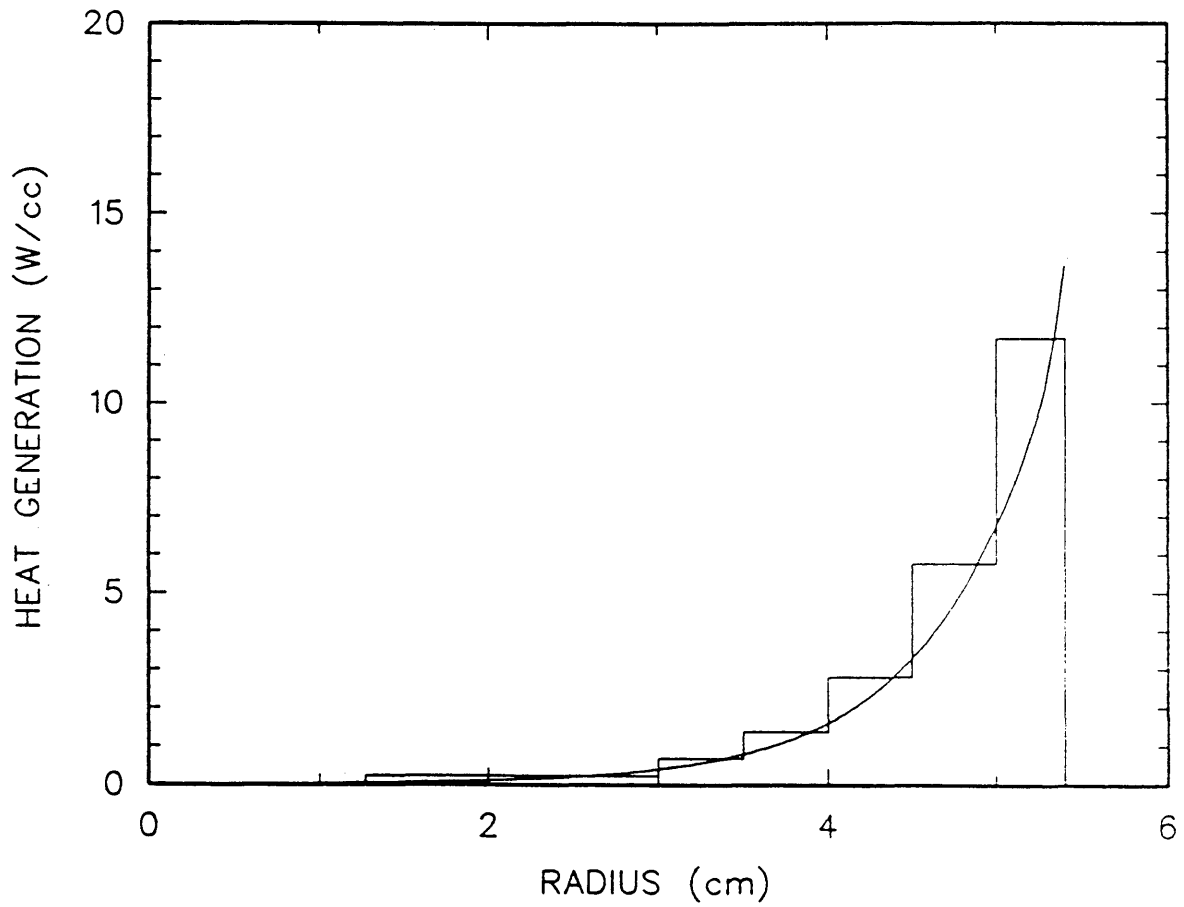


Figure 17 The Heat Generation Term as a Function of Position in the Graphite Die

	18	36	54						
	17	33							
17	16	32							53
	15								
									114 129
	14	31	47	61	75	89	103		128
	13	30	46	60	74	88	102		
	12	29	45	59	73	87	101		
	11	28	44	58	72	86	100		
	10	27	43	57	71	85	99		
	9	26	42	56	70	84	98		
	8	25	41	55	69	83	97		
	7	24	40	54	68	82	96		
	6	23	39	53	67	81	95		
	5	22	38	52	66	80	94		
	4	21	37	51	65	79	93		
	3	20	36	50	64	78	92		
	2	19	35	49	63	77	91		
2	20							101	116
	1	18	34	48	62	76	90		
1	19							100	115

Figure 18 FEM Model Element Designations

varying average heat generation term values. The average heat generation term value are calculated using Lotus spreadsheet located in Appendix III. These values are then assigned as individual material properties in a working FEM model. The discretization of the graphite domain considered the temperature dependent material properties and the heat generation term. These considerations, along with the length to height constraints, formed the basis for the optimization of the FEM mesh.

5.5.1 The First Dot Input File

This analysis used two sets of insulation configurations. The first consisted of a radiation shield made of graphite foil. The emissivity of this graphite is 0.8. The second was a graphite radiation shield and alumina felt insulator. The insulation surrounded the entire graphite die in the annulus between the die and the quartz vacuum tube. The result of these two types of insulation was two sets of temperature boundary conditions, and two temperature profiles. The first set of data are analyzed in this section while the alumina felt and radiation shield data are analyzed in the next section.

Since the Dot code was written when cards were used to input lines of text all the cards can referred to as lines.

The first line of the Dot input file is a quality assurance card. This sequence of symbols must always be placed first or the file will not be processed by the code.

420--05C-02

The next line of code is a title card. This line is used to designate one input file from another.

```
START Model of Induction Hot Press 11/11/90
```

The next line is the master control card where the total number of nodal points, element groups, storage designation, execution mode, and interface control flag are identified. The number of nodal points is the total number of nodes in the FEM mesh. In this instance that number is 129. The element groups are defined as axisymmetric, planar, convection, or radiation. This analysis uses axisymmetric elements because of the axisymmetry of the graphite die. It does not use the other types of elements because temperatures are being used as the boundary conditions.

The default for high speed storage locations is a 0. The next number is the execution mode where 0 is a data

check, and 1 is an execution. Hence the third line in the impute file is:

```
129    1    0    1
```

The lines that follow give node numbers, x coordinates, y coordinates, and the number difference between generated nodes. If the last number does not appear, no nodes will be generated.

```

1          0          0          1
5          0      15.24
6          0      18.20
7          0      20.32
8          0      22.86          1
12         0      27.94
13         0      29.62
14         0      32.60
15         0      35.56
16         0      39.37
17         0      40.64
18         0      44.45
19        1.27          0          1
23        1.27      15.24
24        1.27      18.20
25        1.27      20.32
26        1.27      22.86          1
30        1.27      27.94
31        1.27      29.62
32        1.27      32.60
33        1.27      35.56
34        1.27      39.37
35        1.27      40.64
36        1.27      44.45
37        3.00          0          1
41        3.00      15.24
42        3.00      18.20
43        3.00      20.32

```

44	3.00	22.86	1
48	3.00	27.94	
49	3.00	29.62	
50	3.00	32.60	
51	3.00	35.56	
52	3.00	39.37	
53	3.00	40.64	
54	3.00	44.45	
55	3.50	0	1
59	3.50	15.24	
60	3.50	18.20	
61	3.50	20.32	
62	3.50	22.86	1
66	3.50	27.94	
67	3.50	29.62	
68	3.50	32.60	
69	3.50	35.56	
70	4.00	0	1
74	4.00	15.24	
75	4.00	18.20	
76	4.00	20.32	
77	4.00	22.86	1
81	4.00	27.94	
82	4.00	29.62	
83	4.00	32.60	
84	4.00	35.56	
85	4.50	0	1
89	4.50	15.24	
90	4.50	18.20	
91	4.50	20.32	
92	4.50	22.86	1
96	4.50	27.94	
97	4.50	29.62	
98	4.50	32.60	
99	4.50	35.56	
100	5.00	0	1
104	5.00	15.24	
105	5.00	18.20	
106	5.00	20.32	
107	5.00	22.86	1
111	5.00	27.94	
112	5.00	29.62	
113	5.00	32.60	
114	5.00	35.56	
115	5.40	0	1
119	5.40	15.24	
120	5.40	18.20	

121	5.40	20.32	
122	5.40	22.86	1
126	5.40	27.94	
127	5.40	29.62	
128	5.40	32.60	
129	5.40	35.56	

The first number on the next line of input code designates if the analysis is steady state. A -1 indicates a steady state analysis, whereas a 0 indicates a transient analysis. This number is followed by the required number of time steps which defaults to 1 if left blank this is true even for steady state analysis. The time increment between time steps is given next. The choice of this number was arbitrary for a steady state analysis. The following number is time at start. This is followed by the ambient temperature which was chosen to 25 °C. The next number is not shown because it defaults to zero. This variable is the number of times that the conductivity matrix is reformed. The last number in the line is the time interval for writing out files for steady state this is set to one.

-1 1 30 0 25 1

The next line of code specifies the number of boundary condition functions, data points for each function, and the

total number of nodal points which have boundary conditions assigned to them. In this analysis, the boundary conditions were not a function of time and therefore no functions were specified. There are 25 nodal points that have temperatures assigned to them. These temperatures are extrapolated from the measured temperatures on the graphite die. This was accomplished by assuming smooth temperature variations from one measured point to another.

0 0 2

The next set of lines give the boundary condition number, the node number, the boundary condition type, and the value of the condition. The types of boundary conditions are temperatures designated with a 1, or a flux designated with a 0. The value used in this problem is the temperature at that node.

Chapter VI discusses how these temperature boundary conditions were obtained and the results of this analysis.

1	1	1	60.0
2	19	1	60.0
3	37	1	60.0
4	55	1	60.0
5	70	1	60.0
6	85	1	60.0
7	100	1	60.0
8	115	1	60.0

9	119	1	883.6
10	120	1	933.2
11	121	1	957.4
12	122	1	974.4
13	123	1	978.0
14	124	1	978.2
15	125	1	975.1
16	126	1	968.7
17	127	1	955.2
18	128	1	916.9
19	129	1	860.8
20	114	1	830.0
21	99	1	800.0
22	84	1	762.1
23	69	1	762.1
24	51	1	762.1
25	33	1	60.0
26	36	1	60.0
27	54	1	60.0

The next line specifies if all the nodes are initially set to ambient conditions. This is only important in transient problems. The number given is the number of nodes not set to ambient conditions. In this analysis all the nodes are set to ambient.

0

There are three types of element groups that can be considered in this program. They are 2-D finite elements. These are either planer or axisymmetric. Another type of element group is convection and radiation elements, and the last type is cooling pipe elements. The only type used in this analysis is 2-D axisymmetric quadrilateral elements. The first number in the next line is the element group indicator. For this analysis that number is 1. The next

number gives the total number of elements in this group which is 103 for this analysis. The first element number in this group is given next. This is very important in the case of multiple element groups. The user can not specify two elements with the same number even if the elements are not part of the same group. The next number for this type of element group designates if the 2-D elements are planar or axisymmetric. For this case, all the elements are axisymmetric and is designated with a 0. The maximum number of nodes for any element is given next. All elements in this analysis are given four nodes. The next number is the number of Gauss integration points. For the case of four node elements 2 Gauss points will give an reasonable results, J. N. Node (24). The number of material property sets is given next. Material property sets are designed for all materials exhibit either a difference in thermal properties such as graphite and steel. Material property sets are designated to materials with different heat generation values such as the graphite in the die at various points in the domain. In this analysis, eleven property sets were designated. Property sets were designated for the stainless steel, alumina, ceramic, zirconia, and seven sets for the graphite. These sets for the graphite allowed for the close approximation of the heat generation variation in

the graphite die. The next number of temperature points in the material table. This allows for the material properties temperature dependence to be considered. Since this analysis is steady state only one point was used. That value is one for material properties at all temperatures. The last number is the heat generation flag. If this number is 0, there is no heat generation in the system. If this value is 1, there is heat generation.

1 103 1 0 4 2 11 1 1

The next sets of lines designate the individual thermal properties for material property set. A set consists of two lines of input data. The first line of a set contains the material property number, the number of temperature points describing the material, heat generation function number, and the heat generation value.

The second line of the set has the thermal conductivity in the x direction and the y direction. These numbers are followed by conductivity in the xy direction which is zero because of physical constraints. The last number is the specific heat for the material.

The heat generation function number allows the heat generation to vary with time. Since this is steady state that value is set to zero.

The heat generation terms were approximated by sectioning the graphite die into consecutive cylinder shells. Each shell was given an average heat generation term. These average heat generation terms were estimated for the various shells of the graphite die by assuming a linear variation of the heat generation within each shell. This averaging process has the effect of linearizing the plot in Figure 17. The heat generation values for the inside diameter and outside diameter of the various shells were obtained from Appendix III. An input power to the coil of 5000 W was used in the experiments reported here. These values were averaged and assumed for the domain within the shell.

The first seven material properties were defined for the various regions of the graphite. The set was defined for the stainless steel. The sets after that were for the alumina, zirconia, and the ceramic.

1		1	0	11.7	
	.480	.480		0	1975
2		1	0	5.78	
	.480	.480		0	1975
3		1	0	2.81	
	.480	.480		0	1975

4		1	0	1.38	
	.480		.480	0	1975
5		1	0	.690	
	.480		.480	0	1975
6		1	0	.226	
	.480		.480	0	1975
7		1	0	.020	
	.480		.480	0	1975
8		1	0	0	
	.25		.25	0	480
9		1	0	0	
	.0627		.0627	0	244
10		1	0	0	
	.0242		.0242	0	202.2
11		1	0	0	
	.0380		.0380	0	175.1

The next set of input data defines the elements that make up the mesh. The first number of each line designates the element number. This is followed by the node numbers that define that element. Nodes that define an element are listed in a specific order. The first node in this order is the upper right hand node of the element. This is followed by the upper left hand set node in the element. The next node is the lower left hand node of the element which is followed by the lower right hand node of the element. Figure 19 illustrates the node numbering sequence. The next number is the material property number.

The next number specifies the number of nodes describing that element. This is followed by the number increment for element generation. This number is the increase in global numbers for the local coordinates in the

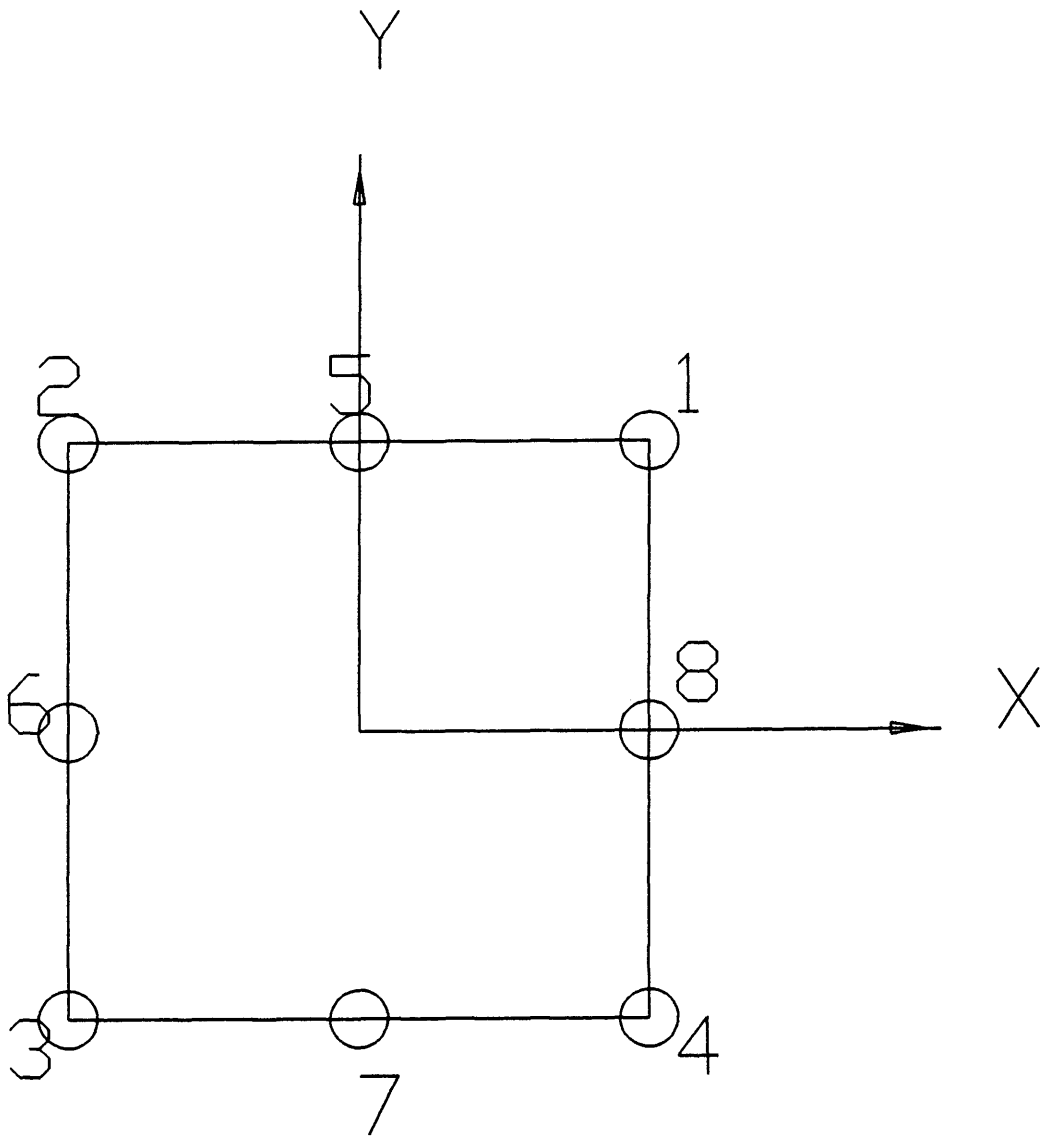


Figure 19 Master Element Nodal Numbering Sequence

master element for successively generated elements.

1	20	2	1	19	9	1	1
4	23	5	4	22	9	4	
5	24	6	5	23	7	4	
6	25	7	6	24	7	4	
7	26	8	7	25	7	4	
8	27	9	8	26	7	4	
9	28	10	9	27	7	4	
10	29	11	10	28	7	4	
11	30	12	11	29	7	4	
12	31	13	12	30	7	4	
13	32	14	13	31	7	4	
14	33	15	14	32	7	4	
15	34	16	15	33	3	4	
16	35	17	16	34	10	4	
17	36	18	17	35	8	4	
18	38	20	19	37	9	4	1
21	41	23	22	40	9	4	
22	42	24	23	41	6	4	
23	43	25	24	42	6	4	
24	44	26	25	43	6	4	
25	45	27	26	44	6	1	1
28	48	30	29	47	6	4	
29	49	31	30	48	6	4	
30	50	32	31	49	6	4	
31	51	33	32	50	6	4	
32	53	35	34	52	10	4	
33	54	36	35	53	8	4	
34	56	38	37	55	9	4	1
37	59	41	40	58	9	4	
38	60	42	41	59	5	4	
39	61	43	42	60	5	4	
40	62	44	43	61	5	4	
41	63	45	44	62	5	4	1
44	66	44	47	65	5	4	
45	67	49	48	66	5	4	
46	68	50	49	67	5	4	
47	69	51	50	68	5	4	
48	71	56	55	70	9	4	1
51	74	59	58	73	9	4	
52	75	60	59	74	4	4	
53	76	61	60	75	4	4	
54	77	62	61	76	4	4	
55	78	63	62	77	4	4	1
56	81	66	65	80	4	4	
59	82	67	66	81	4	4	

60	83	68	67	82	4	4	
61	84	69	68	83	4	4	
62	86	71	70	85	9	4	1
65	89	74	73	88	9	4	
66	90	75	74	89	3	4	
67	91	76	75	90	3	4	
68	92	77	76	91	3	4	
69	93	78	77	92	3	4	1
70	96	81	80	95	3	4	
73	97	82	81	96	3	4	
74	98	83	82	97	3	4	
75	99	84	83	98	3	4	
76	101	86	85	100	9	4	1
79	104	89	88	103	9	4	
80	105	90	89	104	2	4	
81	106	91	90	105	2	4	
82	107	92	91	106	2	4	
83	108	93	92	107	2	4	1
86	111	96	95	110	2	4	
87	112	97	96	111	2	4	
88	113	98	97	112	2	4	
89	114	99	98	113	2	4	
90	116	101	100	115	9	4	1
93	119	104	103	118	9	4	
94	120	105	104	119	1	4	
95	121	106	105	120	1	4	
96	122	107	106	121	1	4	
97	123	108	107	122	1	4	.1
100	126	111	110	125	1	4	
101	127	112	111	126	1	4	
102	128	113	112	127	1	4	
103	129	114	113	128	1	4	

STOP

5.5.2 The Second Dot Input File

The second analysis was identical to the first except for the temperature boundary conditions. These boundary values are provided in this section. The temperature correlation to obtain these boundary temperatures and the

results of the analysis will be discussed in the next chapter.

1	1	1	60.0
2	19	1	60.0
3	37	1	60.0
4	55	1	60.0
5	70	1	60.0
6	85	1	60.0
7	100	1	60.0
8	115	1	60.0
9	119	1	1465.4
10	120	1	1484.0
11	121	1	1491.9
12	122	1	1495.5
13	123	1	1494.9
14	124	1	1492.6
15	125	1	1488.7
16	126	1	1483.3
17	127	1	1473.6
18	128	1	1449.4
19	129	1	1440.0
20	114	1	1430.0
21	99	1	1420.0
22	84	1	1416.6
23	69	1	1416.6
24	51	1	1416.6
25	18	1	60.0
26	36	1	60.0
27	54	1	60.0

5.6 Correlation of the FEM Model to Experimental Data

Thermocouples were placed inside the graphite die of the hot press stack to record temperatures to compare with the numerical solution and verify the model. Figure 12 shows the internal points where temperature were measured. Another verification of the model came from the calculation

of the total heat loss from the system. This was accomplished by placing thermocouples at the water cooling ports and using the flow rates given by the flow meters to calculate heat transported away by the cooling water. Measurement of external temperatures were taken for convective heat loss calculations.

CHAPTER VI

RESULTS

6.1 INTRODUCTION

The Dot analysis was completed on two sets of temperature boundary conditions, both with 5000 W power input. The first set was obtained from an insulation configuration that only consisted of a radiation shield inside the quartz cylinder. Figure 20 illustrates this configuration. The radiation shield was a sheet of graphite foil wrapped around the graphite die in the annulus between the die and the inside wall of the quartz cylinder. The second set of boundary conditions were obtained from an insulation configuration that consisted of the graphite radiation shield and an alumina felt insulating refractory that was wrapped around the outside of the graphite foil. Figure 21 illustrates the second insulation configuration. The insulation configuration drastically affected the heating characteristics of the graphite die.

6.2 THERMOCOUPLE EMPLACEMENT

The thermocouples were placed in the configuration given in Figures 14 and 15. The locations on the FEM mesh that correspond to locations in the graphite die where temperature measurements were made are shown in

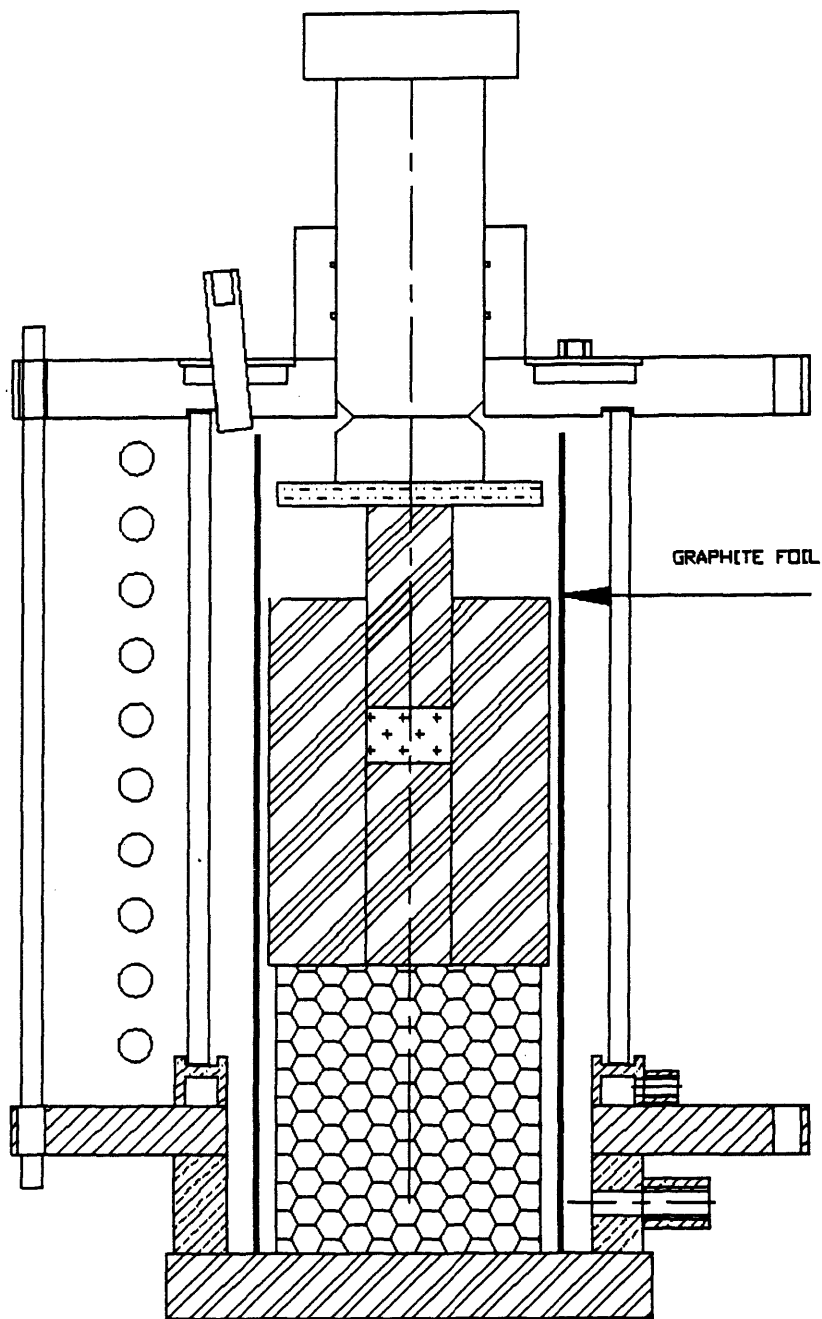


Figure 20 Induction Press with Insulation Configuration Set 1

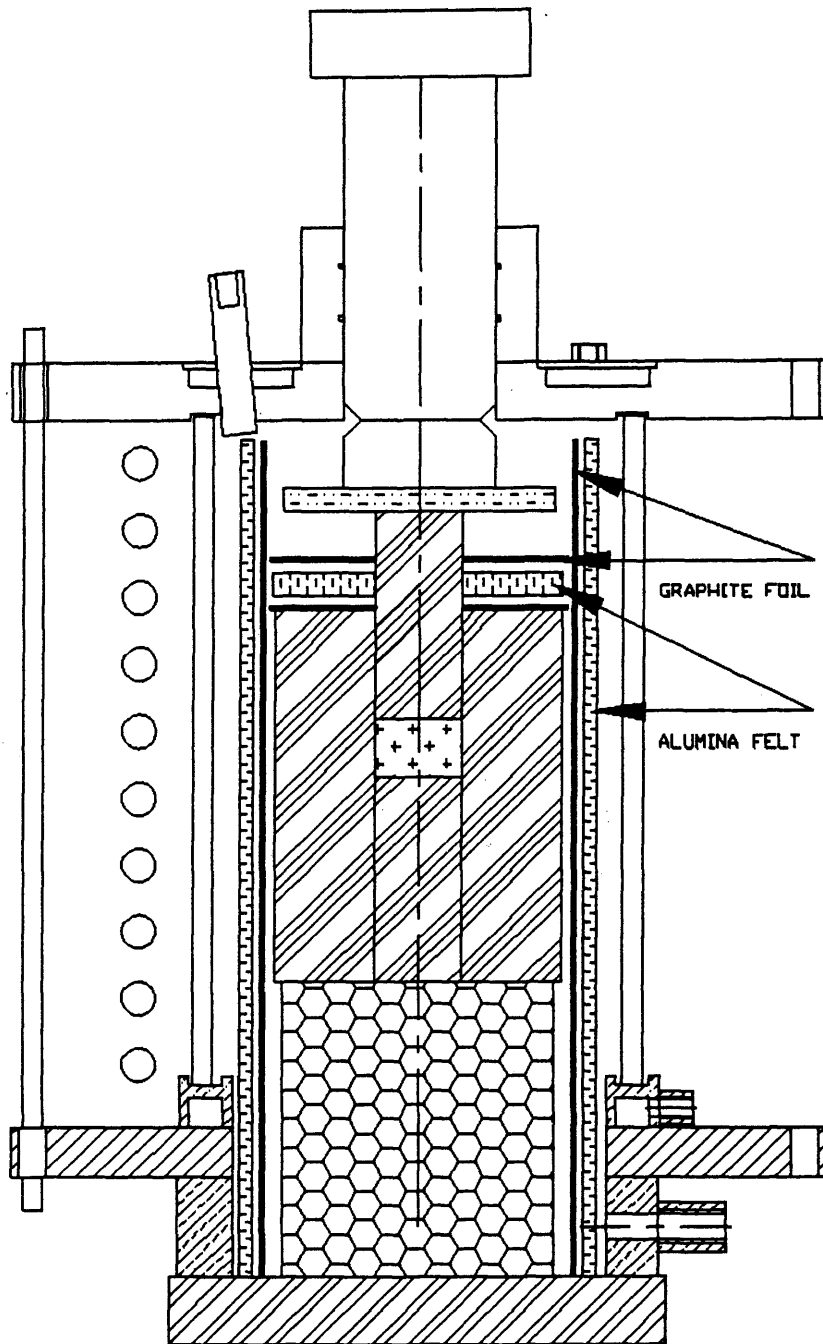


Figure 21 Induction Hot Press with Insulation Set 2

Figure 16. Thermocouples A, B, C, and D measured temperatures that were used as boundary conditions for the FEM model. While, thermocouples E, F, G, and H measured temperatures that verified the model.

The thermocouples were mounted with MgO insulation to insure no direct contact with the graphite. This insured that the thermocouples would not become contaminated by carbon diffusion.

It was observed that the thermocouples did not couple with the radio frequency from the induction coils, since there was no rapid change in the measured temperature after the radio frequency field was disengaged.

6.3 TEMPERATURE MEASUREMENTS

The temperatures were measured with tungsten-5% rhenium/ tungsten-26% rhenium thermocouples. Figure 22 is the reported voltage/temperature curve for this thermocouple. This curve was obtained from the Omega Temperature Measurement Handbook and Encyclopedia. The voltages generated by the thermocouples were measured, recorded and converted to temperatures. Table 1 is the measurements from the first insulation configuration.

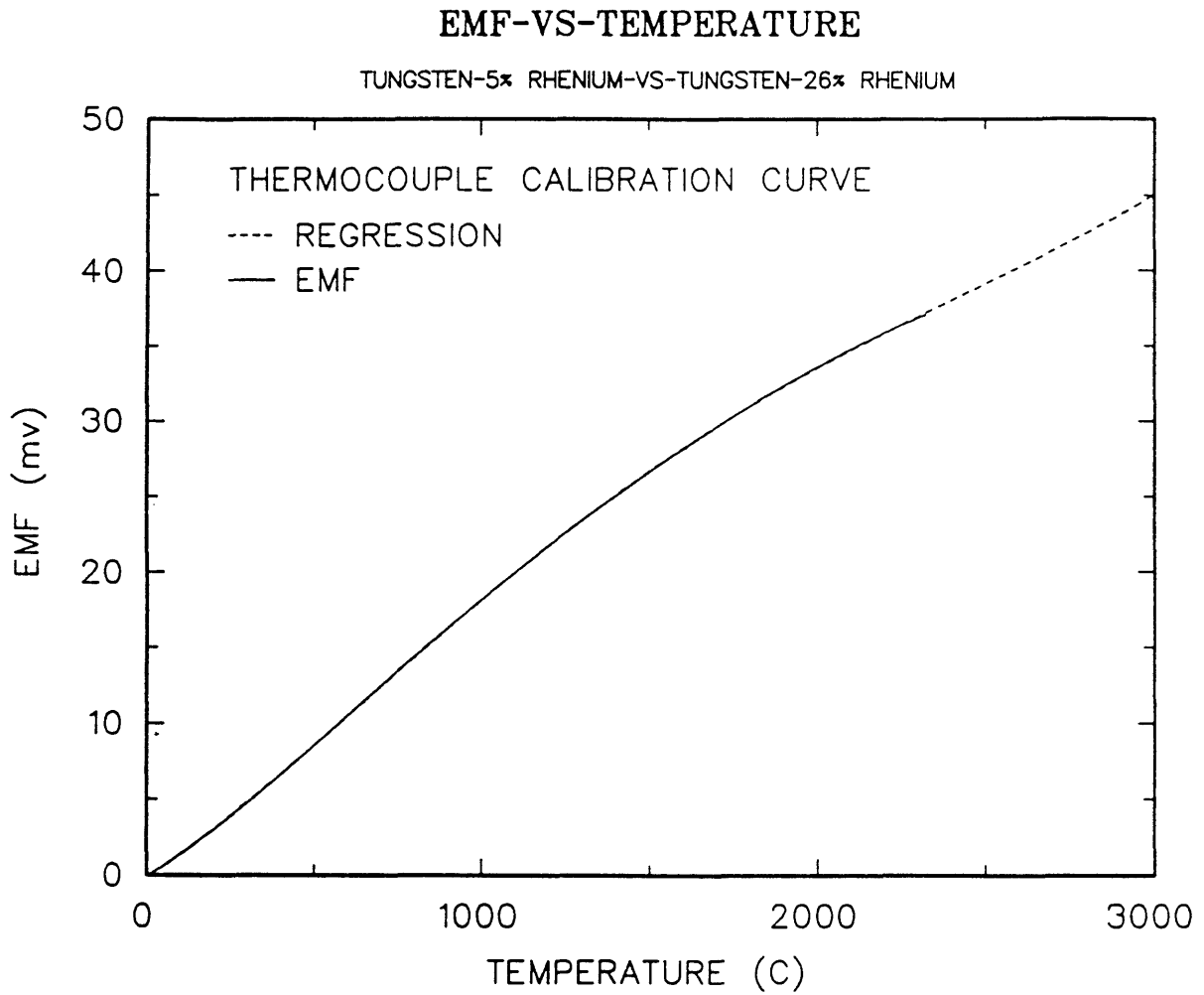


Figure 22 Tungsten-%5 Rhenium/Tungsten-26% Rhenium Thermocouple EMF-VS-Temperature Plot with a Second Order Best Fit Regression Curve

TABLE 1				
Temperature Measurement Data				
From Insulation Configuration Set 1				
TIME	A	A	B	B
min	mv	TEMP (C)	mv	TEMP (C)
0	0.11	20.90	0.11	20.90
10	7.24	430.53	6.74	403.70
20	10.93	623.60	10.16	583.86
30	13.23	741.54	12.34	695.97
40	14.65	814.34	13.71	766.12
50	15.55	860.69	14.57	810.23
60	16.01	884.48	15.02	833.37
70	16.26	897.45	15.29	847.28
80	16.47	908.37	15.45	855.53
90	16.59	914.61	15.54	860.17
110	16.61	915.65	15.54	860.17
130	16.61	915.65	15.54	860.17

TABLE 1				
Temperature Measurement Data				
From Insulation Configuration Set 1				
TIME	C	C	D	D
min	mv	TEMP (C)	mv	TEMP (C)
0	0.12	21.52	0.07	18.39
10	7.7	455.05	6.62	397.22
20	11.6	658.03	10.38	595.23
30	14.08	785.09	12.9	724.65
40	15.62	864.31	14.5	806.64
50	16.59	914.61	15.56	861.21
60	17.11	941.76	16.14	891.22
70	17.38	955.92	16.44	906.81
80	17.62	968.54	16.7	920.34
90	17.75	975.39	16.84	927.65
110	17.8	978.03	16.92	931.83
130	17.8	978.03	16.94	932.87

TABLE 1
Temperature Measurement Data
From Insulation Configuration Set 1

TIME	E	E	F	F
min	mv	TEMP (C)	mv	TEMP (C)
0	0.1	20.27	0.12	21.52
10	7.66	452.92	7.76	458.23
20	11.39	647.25	11.71	663.68
30	13.78	769.71	14.19	790.73
40	15.24	844.70	15.72	869.47
50	16.15	891.74	16.68	919.30
60	16.63	916.70	17.19	945.95
70	16.88	929.74	17.47	960.65
80	17.11	941.76	17.7	972.75
90	17.2	946.48	17.83	979.61
110	17.25	949.10	17.85	980.67
130	17.25	949.10	17.85	980.67

TABLE 1				
Temperature Measurement Data				
From Insulation Configuration Set 1				
TIME	G	G	H	H
min	mv	TEMP (C)	mv	TEMP (C)
0	0.13	22.15	0.12	21.52
10	5.9	358.12	7.37	437.48
20	9.96	573.50	11.26	640.57
30	13.07	733.35	13.81	771.25
40	15.13	839.03	15.43	854.50
50	16.4	904.73	16.49	909.41
60	17.06	939.15	17.06	939.15
70	17.41	957.49	17.38	955.92
80	17.67	971.17	17.64	969.59
90	17.83	979.61	17.78	976.97
110	17.91	983.84	17.86	981.19
130	17.91	983.84	17.86	981.19

Figure 23 is a plot of the temperature distribution of thermocouples A, B, C and D as a function of time for the first insulation configuration. Figure 24 is a plot of the Temperature distribution of thermocouples E, F, G and H as a function of time for the first insulation configuration.

The two important features in these plots are the time to reach steady state and the temperature distribution at the various thermocouples.

Table 2 shows the data obtained from the second insulation configuration. During the placement of the second insulation configuration, thermocouple E was damaged. The data obtained from this thermocouple is not included in Table 2.

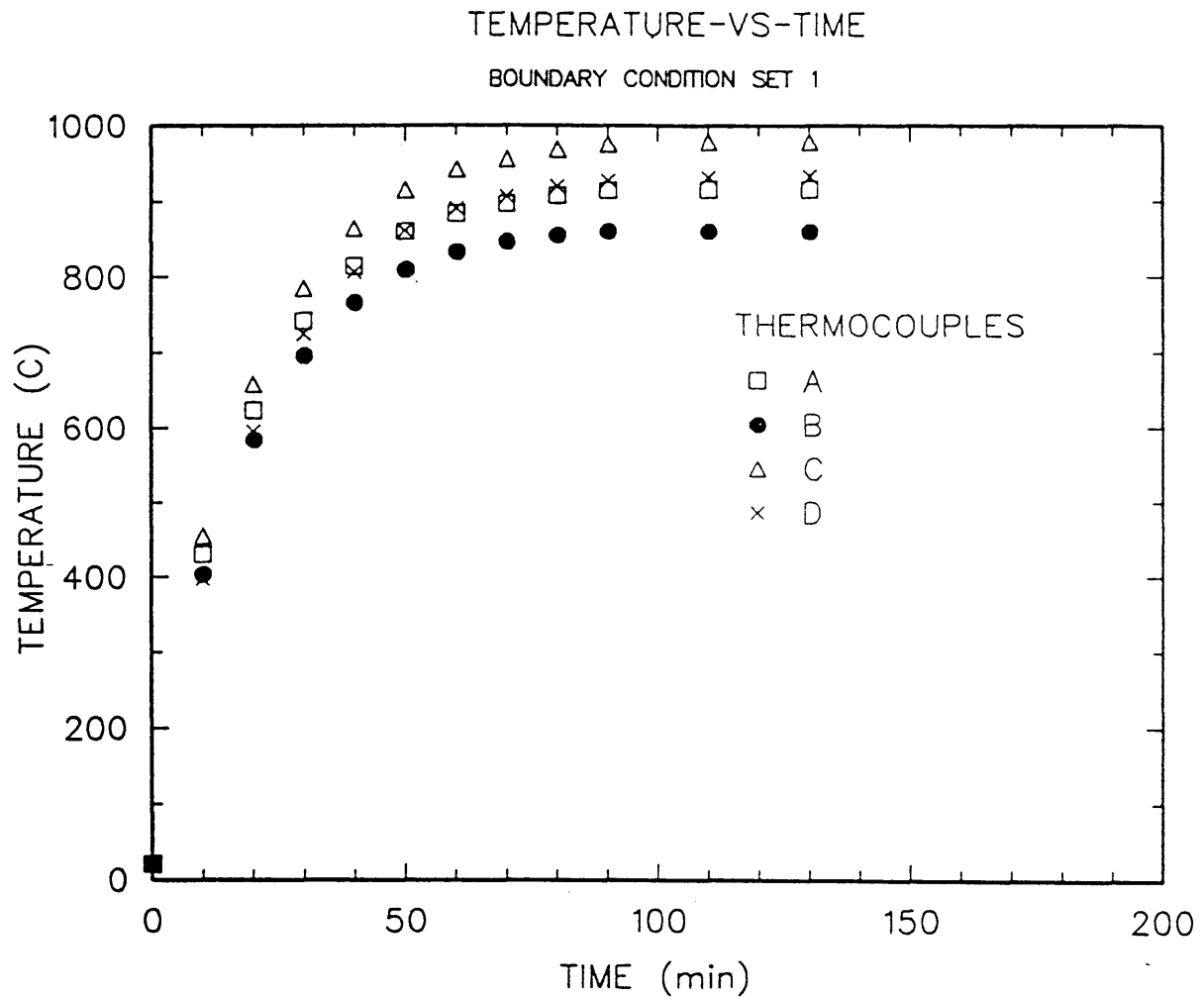


Figure 23 Boundary Condition Set 1 Temperature-VS-Time Plot For Graphite Surface Temperatures

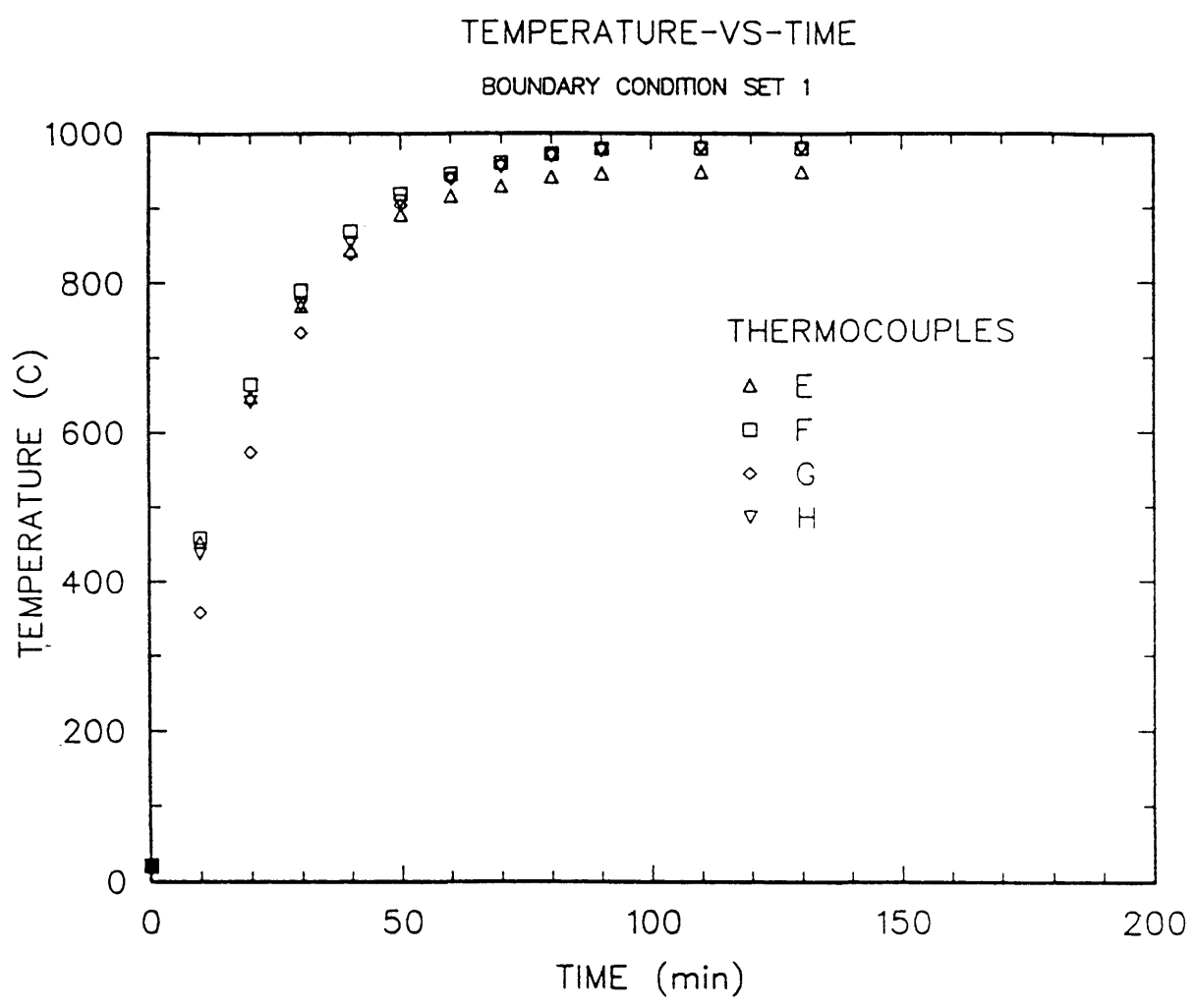


Figure 24 Boundary Condition Set 1 Temperature-VS-Time Plot for Graphite Internal Temperatures

TABLE 2
Temperature Measurement Data
From Insulation Configuration Set 2

TIME	A	A	B	B
min	mv	TEMP (C)	mv	TEMP (C)
0	0.11	20.90	0.11	20.90
5	4.70	291.80	4.73	293.48
15	10.53	602.98	10.51	601.95
25	14.49	806.12	14.45	804.07
35	17.41	957.49	17.3	951.72
45	19.72	1080.73	19.57	1072.60
55	21.3	1167.75	21.08	1155.47
65	22.49	1235.13	22.21	1219.12
75	23.38	1286.71	23.09	1269.79
85	24	1323.31	23.71	1306.12
95	24.52	1354.45	24.21	1335.83
105	24.93	1379.30	24.63	1361.09
115	25.25	1398.88	24.96	1381.13

TABLE 2				
Temperature Measurement Data				
From Insulation Configuration Set 2				
125	25.49	1413.68	25.19	1395.20
135	25.68	1425.47	25.35	1405.04
145	25.81	1433.57	25.46	1411.83
155	25.92	1440.45	25.51	1414.92
165	26.01	1446.09	25.58	1419.26
TIME	C	C	D	D
min	mv	TEMP (C)	mv	TEMP (C)
0	0.12	21.52	0.07	18.39
5	4.97	306.86	3.88	245.55
15	10.8	616.90	9.39	543.89
25	14.8	822.05	13.52	756.39
35	17.78	976.97	16.75	922.95
45	20.16	1104.71	19.3	1058.01
55	21.84	1198.11	21.16	1159.93
65	23.12	1271.53	22.58	1240.30

TABLE 2				
Temperature Measurement Data				
From Insulation Configuration Set 2				
75	24.06	1326.88	23.55	1296.69
85	24.75	1368.35	24.31	1341.82
95	25.29	1401.34	24.91	1378.08
105	25.74	1429.21	25.39	1407.50
115	26.08	1450.49	25.77	1431.08
125	26.31	1465.01	26.05	1448.61
135	26.49	1476.44	26.25	1461.21
145	26.6	1483.45	26.39	1470.08
155	26.7	1489.84	26.5	1477.07
165	26.78	1494.97	26.6	1483.45
TIME	F	F	G	G
min	mv	TEMP (C)	mv	TEMP (C)
0	0.12	21.52	0.13	22.15
5	4.96	306.30	3.54	226.13
15	10.95	624.63	9.12	529.81

25	14.98	831.31	13.38	749.22
35	18	988.60	16.91	931.30
45	20.36	1115.67	19.69	1079.10
55	22.03	1208.88	21.66	1187.95
65	23.3	1282.03	23.09	1269.79
75	24.26	1338.83	24.14	1331.65
85	24.92	1378.69	24.92	1378.69
95	25.47	1412.45	25.52	1415.54
105	25.91	1439.82	26.01	1446.09
115	26.27	1462.48	26.39	1470.08
125	26.52	1478.35	26.67	1487.92
135	26.72	1491.13	26.89	1502.05
145	26.83	1498.19	27.06	1513.02
155	26.92	1503.98	27.21	1522.75
165	27.01	1509.79	27.35	1531.88

TABLE 2
Temperature Measurement Data
From Insulation Configuration Set 2

TIME	H	H
min	mv	TEMP (C)
0	0.12	21.52
5	4.93	304.63
15	10.43	597.81
25	14.4	801.50
35	17.44	959.07
45	19.89	1089.97
55	21.69	1189.64
65	23.07	1268.62
75	24.12	1330.46
85	24.96	1381.13
95	25.58	1419.26
105	26.05	1448.61
115	26.4	1470.72

125	26.68	1488.56
135	26.88	1501.40
145	27.00	1509.14
155	27.09	1514.97
165	27.18	1520.80

Figure 25 is a plot of the temperature distribution of thermocouples A, B, C and D as a function of time for the second insulation configuration. Figure 26 is a plot of the Temperature distribution of thermocouples E, F, G and H as a function of time for the second insulation configuration.

The comparison of Figure 25 to Figure 23 shows that increasing the insulation causes a greater time to reach steady state temperatures and increase in the magnitude of these temperatures. This is important because the forming temperature will vary with insulation type creating difficulty in maintaining quality control of the product being formed.

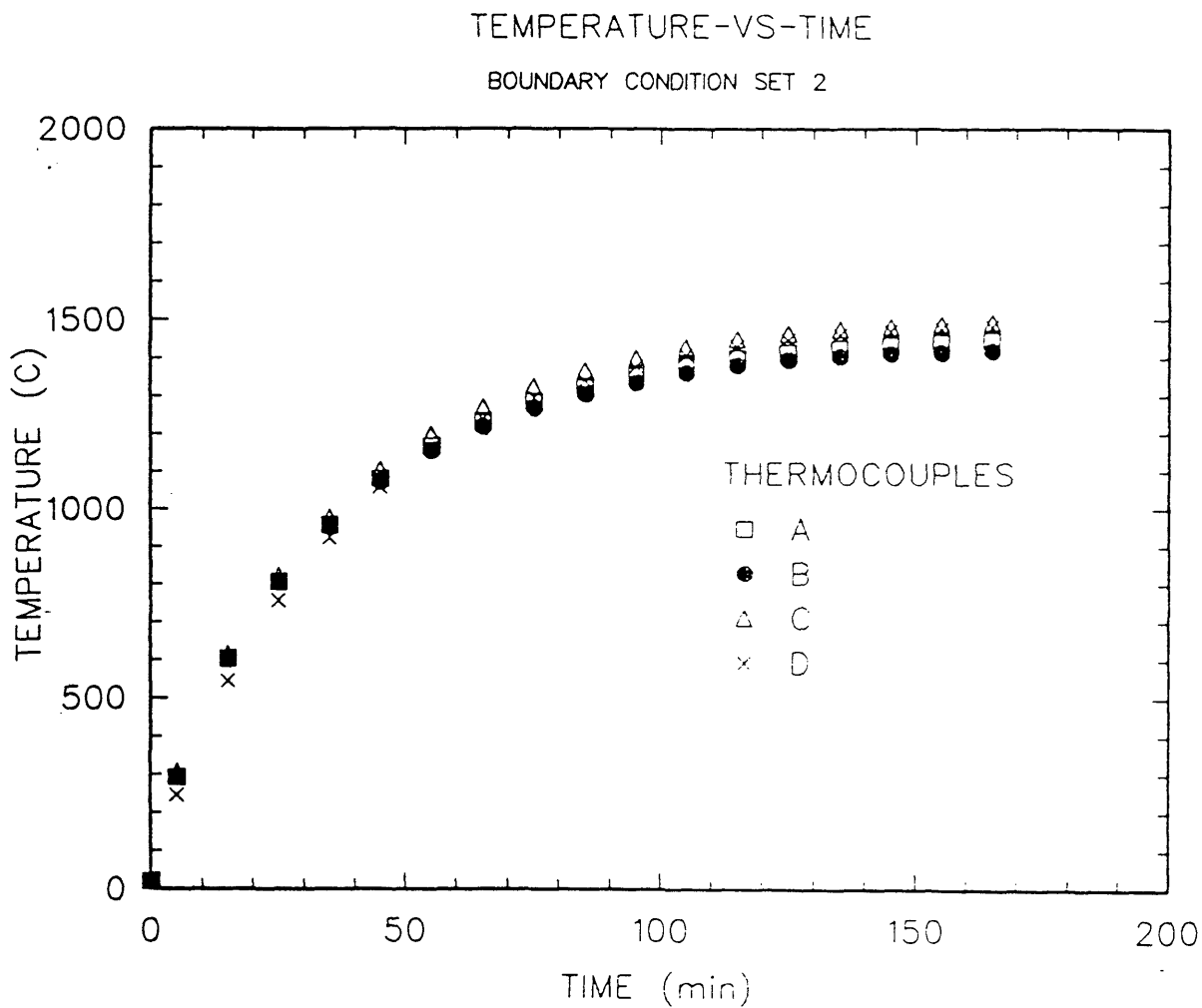


Figure 25 Boundary Condition Set 2 Temperature-VS-Time Plot for Graphite Surface Temperatures

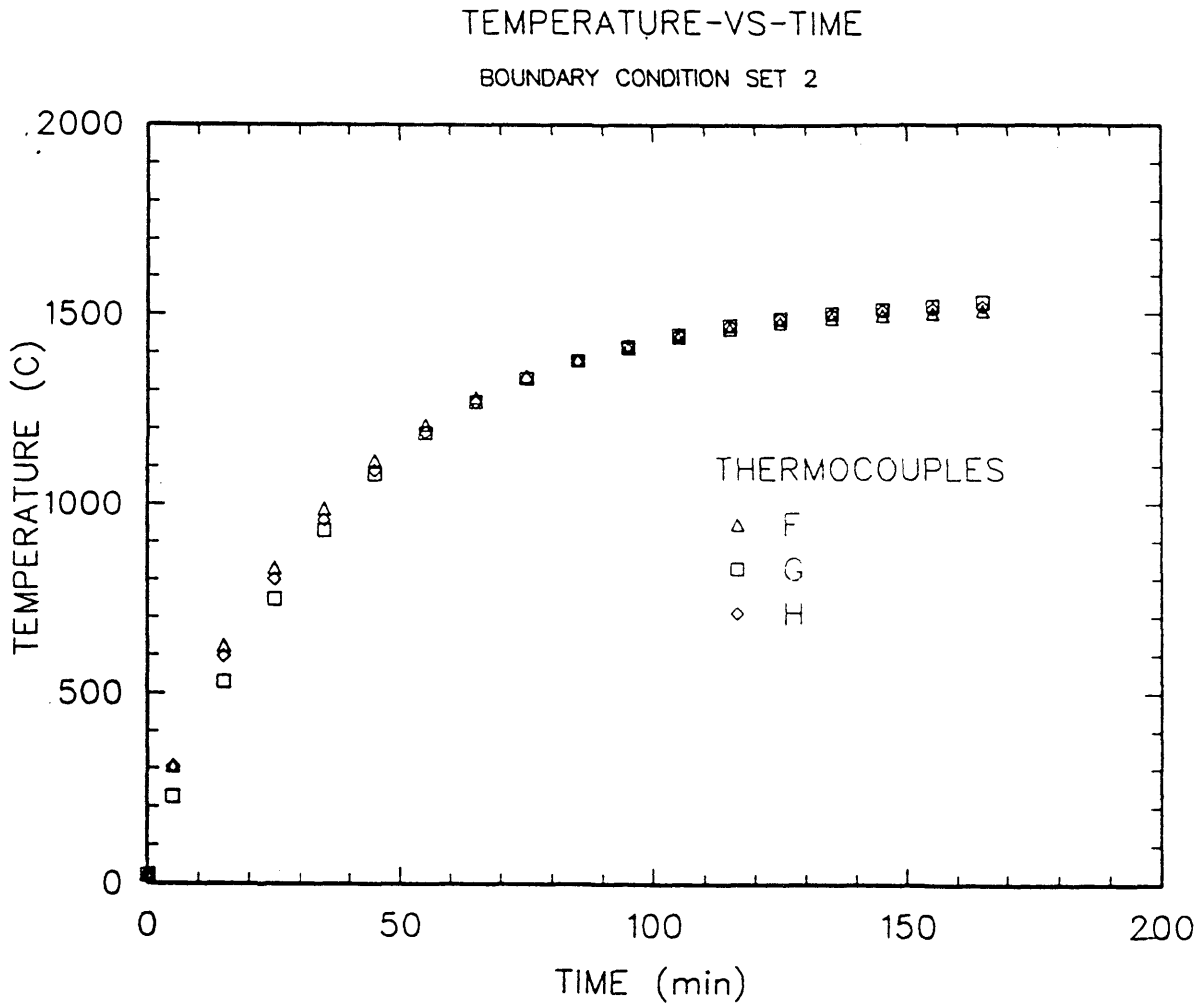


Figure 26 Boundary Condition Set 2 Temperature-VS-Time Plot for Graphite Internal Temperatures

6.4 Estimation of Additional Boundary Temperatures

The temperatures measured on the surface of the graphite die were plotted and fitted with a parabolic curve. The curve was then used to estimate the temperatures at other points on the surface of the graphite die. These estimated temperatures were then assigned to nodal points corresponding to these positions in the finite element mesh. Table 3 is the measured and estimated temperatures for the finite element boundary condition. This table is for boundary condition set 1.

TABLE 3			
Surface Temperature Regression Data for Insulation Configuration Set 1			
		TEMP	REGRESSION
Y	NODE	PARABOLA	BC 1
		BC 1	
39.37	34		762.11
35.56	84	860.17	860.80
32.6	128	915.65	916.90
29.62	127		955.19
27.94	126		968.74
26.67	125		975.13
25.4	124	978.03	978.21
24.13	123		977.98
22.86	122		974.43
20.32	121		957.41
18.21	120	932.87	933.18
15.24	119		883.59

11.43	118		677.70
7.62	117		471.80
3.81	116		265.90
0	115	60	60.00

Figure 27 is a plot of the measured temperatures as a function of position on the graphite die for boundary condition set 1.

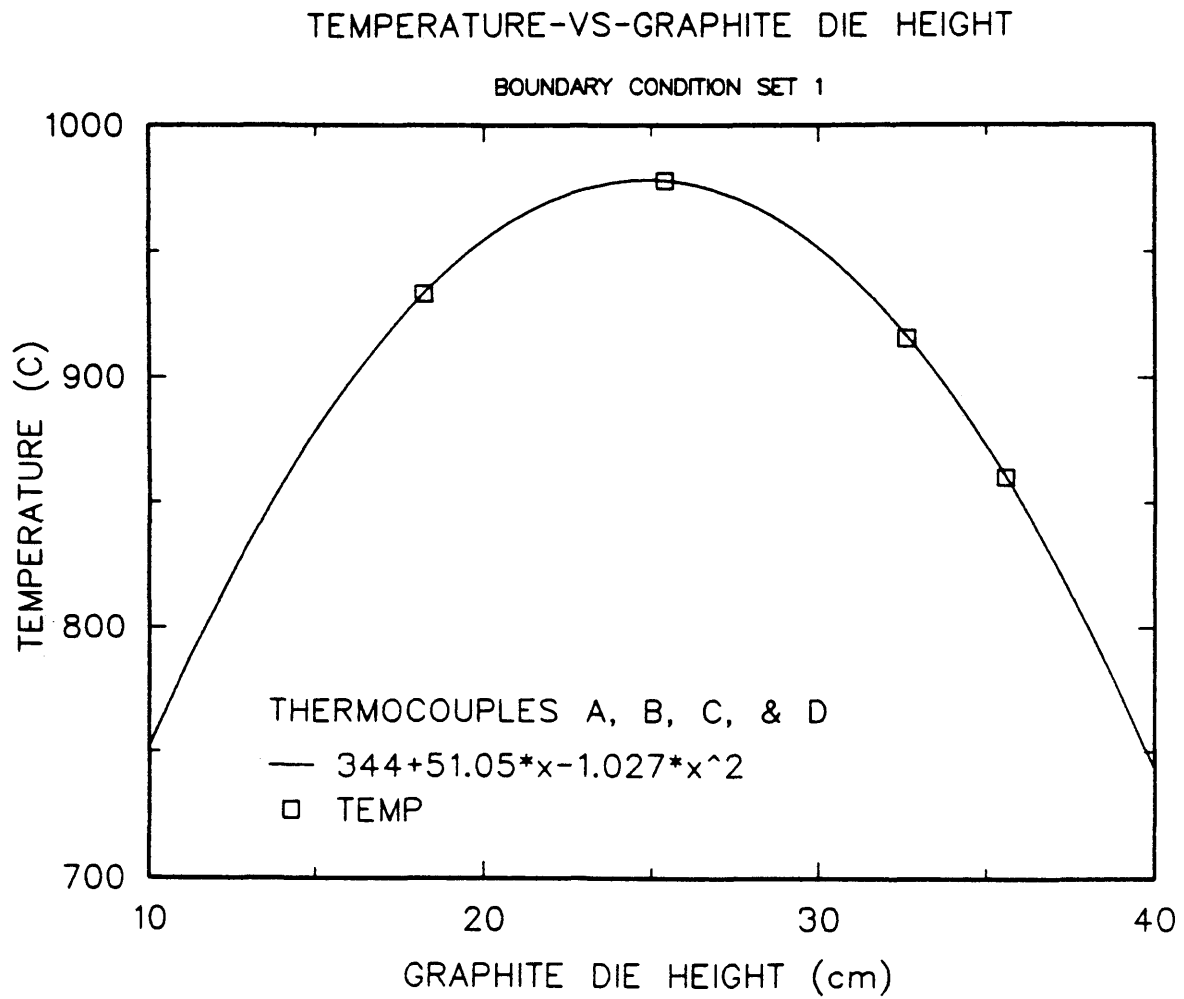


Figure 27 Temperature-VS- Graphite Die Height for Insulation Configuration Set 1

The best fit curve was used to calculate the remaining surface temperatures as given in Table 3.

Table 4 shows the data for the second insulation configuration set where the alumina felt was used.

TABLE 4			
Surface Temperature Regression Data for Insulation Configuration Set 2			
		TEMP	REGRESSION
Y	NODE	PARABOLA	BC 2
		BC 2	
39.37	34		1361.51
35.56	84	1419.26	1416.62
32.6	128	1446.09	1449.42
29.62	127		1473.59
27.94	126		1483.30
26.67	125		1488.77
25.4	124	1494.97	1492.62
24.13	123		1494.86
22.86	122		1495.49
20.32	121		1491.91
18.21	120	1483.45	1484.03
15.24	119		1465.39

11.43	118		1114.04
7.62	117		762.70
3.81	116		411.35
0	115		60.00

Figure 28 is a plot of the measured temperatures as a function of position on the graphite die for boundary condition set 2.

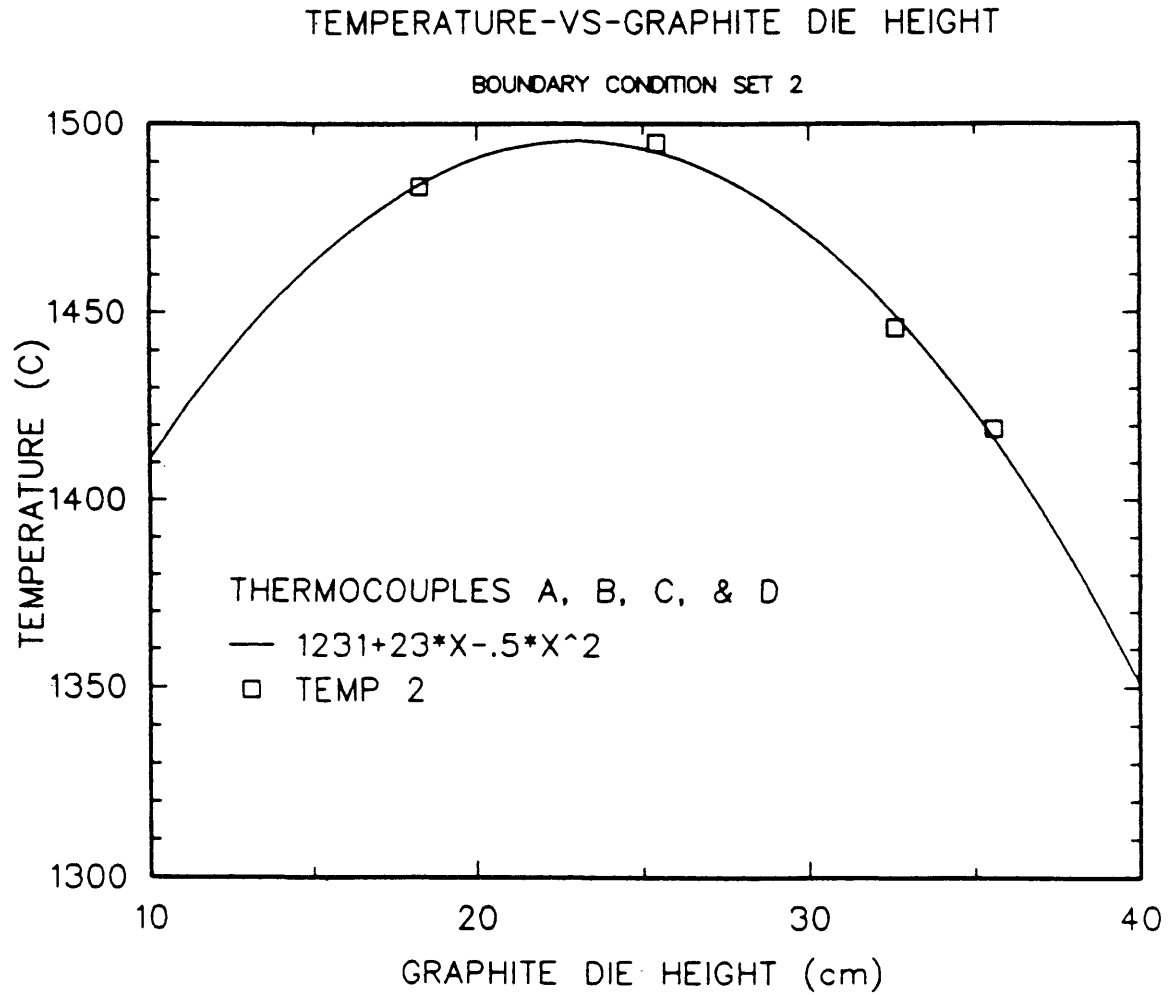


Figure 28 Temperature-VS-Graphite Die Height for Insulation Configuration Set 2

The best fit curve was used to calculate the remaining surface temperatures in this insulation configurations as given in Table 4.

6.5 Comparison of Dot Output to Measured Temperature Profile

Temperatures were measured at internal points in the graphite die. These temperatures were compared to the Dot predicted temperatures at nodal points corresponding to these positions in the finite element mesh. Table 5 has the results from the insulation configuration set 1. This table includes the Dot temperatures and the measured temperatures with an error calculation.

TABLE 5				
Error Analysis Data for				
Insulation Configuration Set 1				
		MEASURED	Dot	% ERROR
THERMO- COUPLE	NODE POINTS	TEMP (C)	TEMP (C)	
A	128	916	BC	N/A
B	84	860	BC	N/A
C	124	978	BC	N/A
D	120	933	BC	N/A
E	98	949	918	-3.28
F	49	981	955	-2.62
G	10	984	982	-0.19
H	42	981	954	-2.77

The accuracy ranges from $-.19\%$ to -3.28% with nodal point 10 being the most accurate. This is also the point where the maximum temperature was measured.

Table 6 shows the results from the insulation configuration set 2. This table also includes the Dot temperatures and the measured temperatures with an error calculation.

TABLE 6				
Error Analysis Data for				
Insulation Configuration Set 2				
		MEASURED	Dot	% ERROR
COUPLE	NODE	TEMP (C)	TEMP (C)	
A	128	1446	BC	N/A
B	84	1419	BC	N/A
C	124	1495	BC	N/A
D	120	1483	BC	N/A
F	49	1509	1460	-3.25
G	10	1532	1505	-1.76
H	42	1520	1501	-1.25

ARTHUR LAKES LIBRARY
 COLORADO SCHOOL of MINES
 GOLDEN, COLORADO 80401

6.6 PostDot Interpretations of Dot Output

The results from the Dot code were graphically presented by Postdot. This program was written as a compliment to the Dot program. The resulting temperature profile in the induction hot press stack for the first insulation configuration of just a radiation shield is illustrated in Figure 29. Figure 30 is the Postdot plot of the temperature profile in the hot press stack that was calculated by Dot for the second insulation configuration.

Generally the isothermal patterns are very similar in Figures 29 and 30. The important features are that the temperature variation is greatest where the insulation is the least, Figure 20. The range of temperatures in the insulation set 1 range from 800 °C to 990 °C as compared to 1425 °C to 1525 °C in the insulation set 2. This is very important feature because if components are formed in a stack there forming temperature may vary by 100 degrees or more. The forming temperature range of a single ceramic component is within a 15 degree variation. This can be see in Figures 29 and 30.

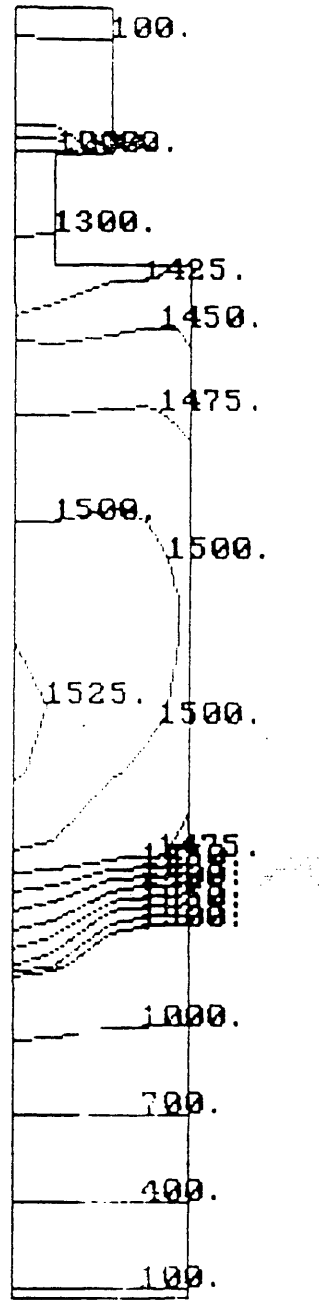


Figure 30 Postdot Temperature Isothermal Contour Plot in the Hot Press Stack for Insulation Configuration Set 2

6.7 Energy Balance of the Hot Press System

Table 7 shows the results of an energy balance for the hot press system where Case 1 corresponds to insulation configuration set 1, and Case 2 corresponds to insulation configuration set 2.

The purpose of this analysis was to investigate the reasonability of the heat generation term. The heat generation term was calculated assuming a value for the total power dissipated in the graphite die. For steady state heat generation, the power losses will equal the total heat generated within a body. If the heat generated is within experimental error of the heat losses, it can be assumed to be reasonable.

The heat losses from the hot press along with the heat generated in the graphite die of the hot press have been presented in Table 7. The cooling water flow rate to each of the hot press components was measured to be 1.5 gpm with an increase in temperature of 2.5 °C. This resulted in a power loss of .99 kW from each of these components. The quartz outside wall temperature was measured for the two insulation configurations. A temperature of 330 °C was measured for configuration set 1 and 284 °C for configuration set 2. The power losses for these two configurations were due to convection and radiation. The

convective losses were calculated to be 0.305 kW for configuration set 1 and .259 kW for configuration set 2. The radiation losses were calculated to be 1.02 kW for configuration set 1 and .729 kW for configuration set 2. The convection calculations were based upon natural convection from a plane vertical wall. The correction for a cylindrical body showed that at these temperatures the error associated with a plane wall analysis was negligible. The radiation was analyzed with a view factor of 1.0, a quartz emissivity of 0.87, and ambient temperature of 25 °C. The measured power loss for configuration set 1 was estimated to be 4.03 kW and for configuration set 2 4.40 kW. A calculated power of 4.4 kW was assumed to be dissipated in the graphite die. This value was derived in Appendix I. It was also used to calculate the heat generation term. An error analysis revealed that the measured power can only be reported to two significant figures with confidence. This represents an error of 10% for the two insulation conditions.

Since the assumed power dissipated in the hot press is within the experimental error of the measured power losses, it is reasonable to assumed that heat generation term used in this analysis is within experimental error.

TABLE 7					
ENERGY BALANCE DATA FOR HOT PRESS SYSTEM					
UNITS OF POWER kW	RAM	TOP PLATE	BOTTOM PLATE	QUARTZ TUBE	Σ LOSSES
FLOW RATE	1.5 gpm	1.5 gpm	1.5 gpm	Case 1 Case 2	
h_{wall}				5.5 W/°K m ²	
h_{cy}/h_{wall}				1.0	
Δ TEMP (°C)	2.5 2.5	2.5 2.5	2.5 2.5	284 330	
POWER LOSS WATER	.99 .99	.99 .99	.99 .99		2.98 2.98
POWER LOSS RAD.				.793 1.11	.793 1.11

POWER				.259	.259
LOSS				.305	.305
CONV.					
MEASURED					4.03
POWER					4.40
LOSSES					
GENERATED					4.40
HEAT					
ERROR					-9.2%
					0.0%

CHAPTER VII

CONCLUSIONS AND RECOMMENDATIONS

7.1 CONCLUSIONS

The thermal analysis of the hot press process is very sensitive to boundary conditions. The temperatures at the die surface drastically changed the calculated internal temperatures.

Surface temperatures can be estimated by curve fitting measured temperatures with a parabola. The equation to the parabola can then be used to estimate the temperatures at other positions on the surface of the die corresponding to nodal points in the finite element mesh.

The time required to reach steady state temperatures is a function of the insulation configuration. These steady state temperatures are also a function of insulation and position in the graphite die. The variation of these internal temperatures in the graphite die were noted to be substantial but decreased with increased insulation.

The temperature range for configuration set 1 was about 200 °C, where as for configuration set 2 it was only about 100 °C. Although the range in the internal temperatures of the graphite die varied substantially, the PostDot isothermal plots indicated that the variation in forming

temperature of any one ceramic component would be less than 15 °C.

The temperature distribution in an inductively heated hot press can be calculated using finite element techniques.

7.2 RECOMMENDATIONS

From a production point of view, these temperature variations represent variables in the quality control capabilities of multiple-component pressing. The next step is to investigate if a correlation can be established between insulation type, power to the load and external temperature profiles. A possible approach would be to choose a insulation configuration and vary the power levels while measuring temperature profiles. Once a set of boundary temperature curves has been established for a specific insulation configuration, they can be used to estimate boundary temperatures given one temperature point.

Along with this investigation, there needs to be improvement of the heat generation term. The improved model of the heat generation term should account for the shortness of the induction coil. The heat generation term should be numerically integrated over the domain of the elements. This would require a modification to the Dot program.

The combination of these steps will reduce the approximations in this model. The result of this should improve this model significantly and its industrial usefulness.

REFERENCES

1. H. B. Dwight, "Skin Effect in Tubular and Flat Conductors", A.I.E.E. Trans., Volume 41, pg. 189, 1922.
2. H. B. Dwight, "A Precise Method of Calculation of Skin Effect in Isolated Tubes", A.I.E.E. Jl., Volume 42, pg. 827, August, 1923.
3. N. R. Stansel, "Industrial Electric Heating", General Electric Review, Volume 37, pg. 440, 1936.
4. J. Greig, "An Introduction to the Theory of Eddy ~~Current~~ Heating", World Power, Volume 26, pg. 246, 1936.
5. R. M. Baker, "Heating of Nonmagnetic Electric Conductors by Magnetic Induction-Longitudinal Flux", Electrical Engineering Transactions, Volume 63, pg. 273, 1944.
6. H. F. Storm, "Surface Heating by Induction", Electrical Engineering Transactions, Volume 63, pg. 749, 1944.
7. N. R. Stansel, "Induction Heating-Selection of Frequency", A.I.E.E. Trans., Volume 63, pg. 755, 1944.
8. J. T. Vaughan and J. W. Williamson, "Design of Induction-Heating Coils for Cylindrical Nonmagnetic Loads", A.I.E.E. Trans., Volume 64, pg. 587, 1945.
9. G. H. Costache, "Calculation of Eddy Currents and Skin Effects in Nonmagnetic Conductors by the Finite Element Method", Rev. Roum. Sci. Techn-Electrotechn, Volume 21, pg. 357, 1976.
10. M. Fabiano, "Losses in Conducting Rectangular Cylinders Due to Finite Length Coils ", I.E.E.E. Transactions on Magnetism, Volume Mag-12, pg. 1062, 1976.

11. K. Preis, H. Stragner and K. R. Richter, "Finite Element Analysis of Anisotropic and Nonlinear Magnetic Circuits", I.E.E.E. Transactions on Magnetism, Volume Mag-17, No. 6, pg. 3396, 1981.
12. C W. Trowbridge, "Three-Dimensional Field Computation", I.E.E.E. Transactions on Magnetism, Volume Mag-18, pg. 293, 1982.
13. A. Konrad, M. V. K. Chari and Z. J. Csendes, "New Finite Element Techniques for Skin Effect Problems ", I.E.E.E. Transactions on Magnetism, Volume Mag-18, pg. 450, 1982.
14. M. G. Reynolds, "Power Loss in Tubular Conductors of Induction Heating Coils", I.E.E.E. Transactions of Power Apparatus and Systems, Volume PAS-103, pg. 923, 1984.
15. W. H. Brixius, Properties and Characteristics of Graphite. Decatur, Texas: Poco Graphite Incorporated, 1989.
16. P. Boresi and Omar M. Sidebottom, Stress-Strain-Temperature Relations. Chap. 2 in Advanced Mechanics of Materials. New York: John Wiley and Sons, 1985.
17. A. D. Deutschman, W. J. Michels and C. E. Wilson, Fasteners. Chap. 16 in Machine Design Theory and Practice. New York: Macmillan Publishing Company Incorporated, 1975.
18. F. P. Incropera and D. P. DeWitt, Free Convection. Chap. 9 in Fundamentals of Heat and Mass Transfer. New York: John Wiley and Sons, 1985.
19. W. J. Minkowycz and E. M. Sparrow, "Local Nonsimilar Solutions for Natural Convection on a Vertical Cylinder", Journal of Heat Transfer, Volume 96, pg. 178, 1974.
20. Polivka, R. M. and Wilson, E. L.. Finite Element Analysis of Nonlinear Heat Transfer Problems, UC SEM 76-2, Department of Civil Engineering, University of California, Berkeley, California, 1976.

22. R. C. Weast, M. J. Astle and W. H. Beyer, Handbook of Chemistry and Physics. Boca Raton, Florida: CRC Press Incorporated, 1989.
23. W. D. Kingery, Introduction to Ceramics. New York: John Wiley and Sons, 1985.
24. J. N. Reddy. Finite-Element Analysis of Two-Dimensional Problems. Chap. 4 in An Introduction to the Finite Element Method. New York: McGraw- Hill Book Company, 1984.
25. P. A. Tipler, Faraday's Law. Chap. 28 in Physics. Rochester, Michigan: Worth Publishers Incorporated, 1982.
26. N. W. McLachlan, Application of Ber and Bei Functions to the Resistance of Conductors to Alternating Current. Chap. 9 in Bessel Functions for Engineers. Oxford: Clarendon Press, 1934.
27. G. H. Brown, C. N. Hoyler and R. A. Bierwirth, Induced Currents in Cylindrical Conductors. Chap. 2 in Theory and Application of Radio-Frequency Heating. New York: D. Van Nostrand Company Incorporated, 1947.
28. M. Abramowitz and I. A. Stegun. Bessel Functions of Integer Order. Chap. 9 in Handbook of Mathematical Functions with Formulas, Graphs, and Mathematical Tables National Bureau of Standards, 1970.

APPENDIX I

Derivation of the Heat Generation Term

The magnetic flux ϕ_m of a magnetic field through a surface inside a solenoid, Figure 31, can be defined as

$$\phi_m = \int \mathbf{B} \cdot \mathbf{N} dA \quad (25)$$

B Magnetic intensity

N Normal vector

If the point of interest is far from the ends of the solenoid, the magnetic induction at the center line of the cylinder can be expressed as

$$B_o = \mu_o n I \quad (26)$$

The variables μ_o , n and I are the permeability of free space, coil turns per unit length and the coil current, respectively. If a material is inserted into the solenoid, there is an additional contribution to the magnetic-induction field due to the magnetization of this material as shown in Figure 32.

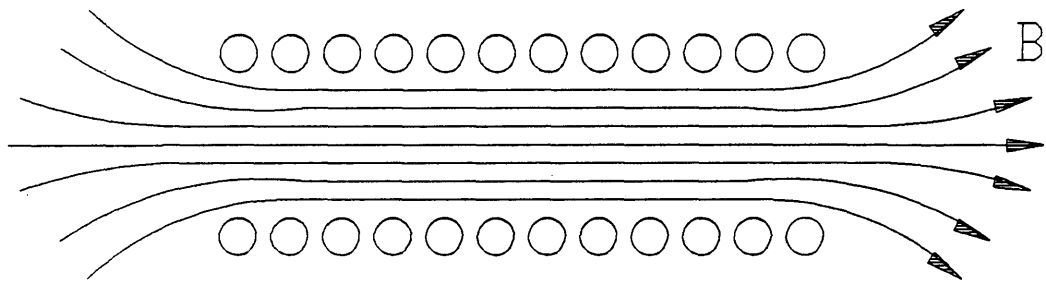
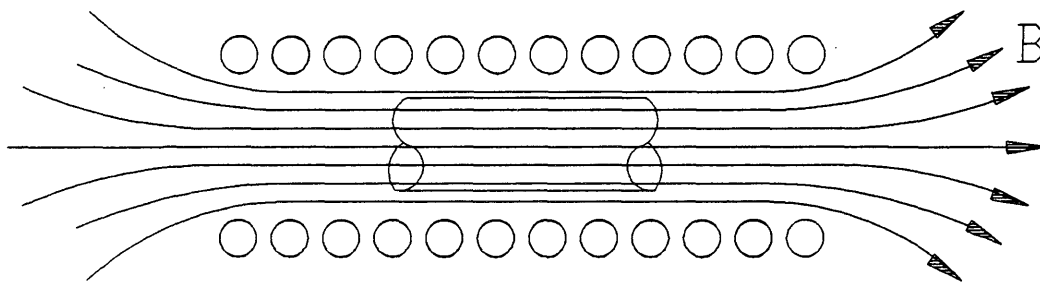


Figure 31 Magnetic field lines in a solenoid



**Figure 32 Magnetic Field Lines in a Solenoid with Material
Inserted into it.**

The induction field B_m is defined by equation (27).

$$B_m = \mu_o M \quad (27)$$

M Magnetic moment per volume

The amperian current per unit length replaces the current per unit length, nI . The total magnetic induction at the center of the solenoid is the vector sum of these separate fields.

$$B = B_o + \mu_o M \quad (28)$$

Dividing equation (28) by μ_o results in equation (29).

$$\frac{B}{\mu_o} = \frac{B_o}{\mu_o} + M \quad (29)$$

Rearranging equation (29) will result in defining a new term called the magnetic intensity vector.

$$\frac{B_o}{\mu_o} = \frac{B}{\mu_o} - M = H \quad (30)$$

The magnetic intensity vector is defined by

$$\mathbf{H} = \frac{\mathbf{B}}{\mu_0} - \mathbf{M} \quad (31)$$

For paramagnetic and diamagnetic materials, the magnetization, \mathbf{M} , and the magnetic intensity vector, \mathbf{H} , are proportional. The proportionality constant is a material property called the susceptibility, χ_m .

$$\mathbf{M} = \chi_m \mathbf{H} \quad (32)$$

By rearranging equation (32) and multiplying through by μ_0 , the magnetic induction can be defined in terms of the \mathbf{M} and \mathbf{H} .

$$\mathbf{B} = \mu_0 (\mathbf{H} + \mathbf{M}) \quad (33)$$

If \mathbf{M} is replaced by $\chi_m \mathbf{H}$, then equation (33) can be written as

$$\mathbf{B} = \mu_0 (1 + \chi_m) \mathbf{H} \quad (34)$$

The permeability inside a body can now be defined in terms of the permeability in a vacuum.

$$\mu = \mu_o(1+\chi_m) \quad (35)$$

Substituting equation (35) into equation (34) results in the following identity.

$$\mathbf{B} = \mu \mathbf{H} \quad (36)$$

By substituting equation (36) into equation (25), the magnetic flux through a surface, ϕ_m , in a solenoid, Figure 33, can be defined in terms of the magnetic intensity vector, \mathbf{H} .

$$\phi_m = \int \mathbf{H} \cdot \mathbf{N} da \quad (37)$$

If a slice of the solenoid is taken perpendicular to the axis of symmetry, an incremental width dr can be defined at a distance r from the center of the solenoid. This width then forms a band around the surface at a constant distance r from the center of the solenoid, Figure 31. It is assumed that the circumferential length around the inside of the band is approximately equal to the circumferential length around the outside of the band. The area of the band can be then be defined as $2\pi r dr$. Substituting this into equation (37) for the incremental area da and taking the constants outside the integral results in equation (38).

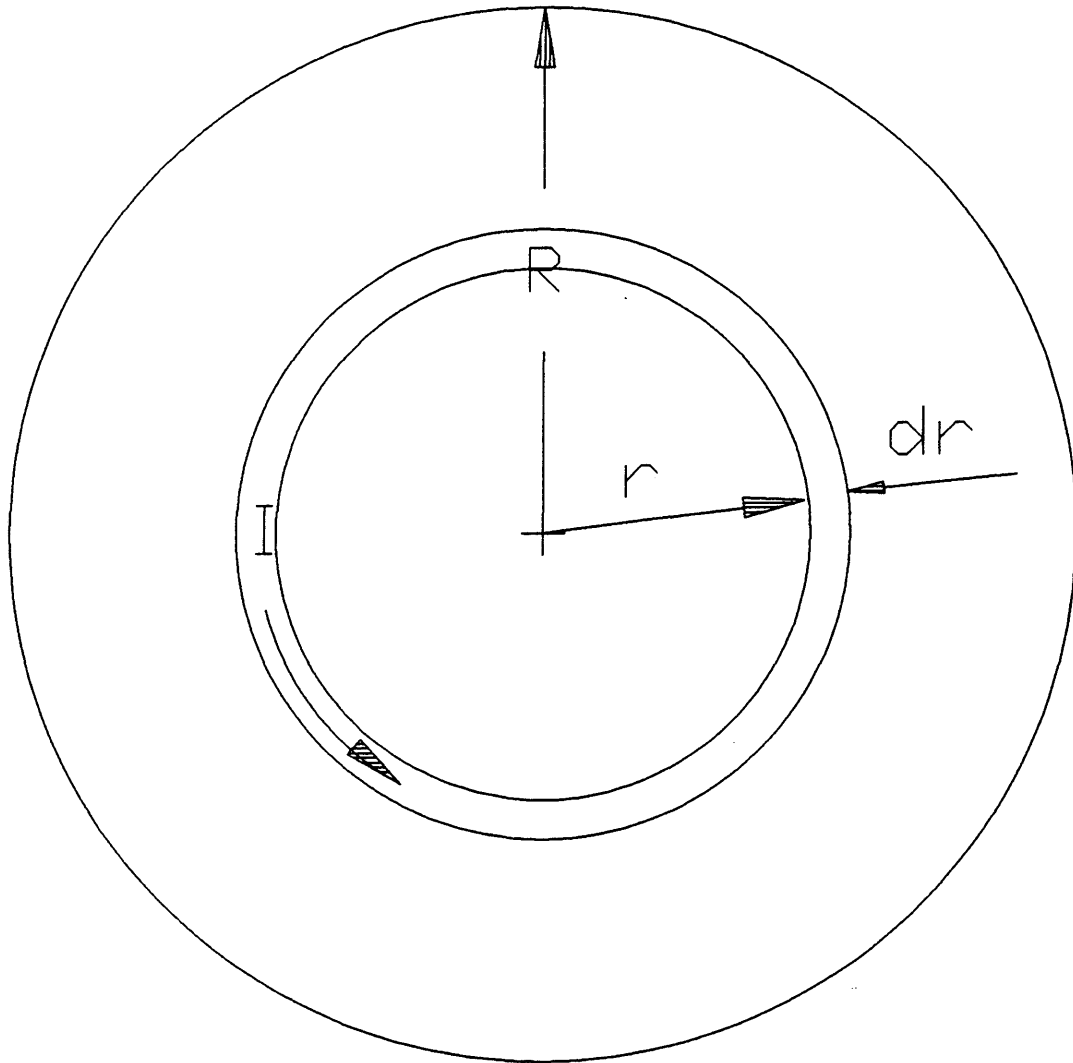


Figure 33 Induced Eddy Currents in a Solenoid

$$\phi_m = \mu 2 \pi \int H r dr \quad (38)$$

Faraday's law, P. A. Tipler (25), states that an electromotive force (emf) can be induced by the time rate change of a magnetic flux, ϕ_m .

$$\mathcal{E} = -\frac{d\phi_m}{dt} \quad (39)$$

Differentiating equation (39) with respect to time results in equation (40).

$$\mathcal{E} = -\frac{\partial}{\partial t} 2 \pi \mu \int_0^R r H dr \quad (40)$$

Taking the derivative inside the integral results in

$$\mathcal{E} = -2 \pi \mu \int_0^R r \frac{\partial H}{\partial t} dr \quad (41)$$

A materials resistivity is defined as follows

$$\rho = \frac{RL}{A} \quad (42)$$

where R , L , and A are the materials resistance to current flow, the length of current flow, and the area perpendicular to the current flow. By assuming current flowing in a circular circuit, such as in Figure 33, the length of the current flow can be defined as $2\pi r$. The area perpendicular to the current flow is hdr . Substituting these into equation (43) results in

$$R = \frac{\rho 2\pi r}{hdr} \quad (43)$$

Another term, called the conductivity, σ , is defined as the reciprocal of the resistivity, ρ . If unit depth is assumed, the h equals unity. By assuming unit depth and substituting the conductivity into equation (44), the resistance of a material can be defined as

$$R = \frac{2\pi r}{\sigma dr} \quad (44)$$

The current density can be defined as

$$J = \frac{I}{A} \quad (45)$$

Assuming unit depth for the incremental area perpendicular to the current flow, the total current flowing through an area hdr can be defined as

$$dI = Jdr \quad (46)$$

Ohm's law for an incremental current dI and constant electric resistance, R , can be written as

$$dI = \frac{dV}{R} \quad (47)$$

Integrating equations (46) and equations (47) and setting them equal to each other results in

$$\frac{V}{R} = \frac{\mathcal{E}}{R} = JR_o \quad (48)$$

Dividing equation (41) by R and substituting equation (48) for the emf/R results in equation (49).

$$JR_o = \frac{-2\pi\mu}{R} \int_0^{R_o} r \frac{\partial H}{\partial T} dr \quad (49)$$

Substituting equation (44) into equation (49) and reducing results in equation (50).

$$J = \frac{-\sigma \mu}{R_o} \int_0^{R_o} r \frac{\partial H}{\partial T} dr \quad (50)$$

Ampère's law, N. W. McLachlan (26), states that the magnetizing force within the ring due to eddy currents is

$$dH = -J dr \quad (51)$$

for cgs units; therefore, the current density can be defined as

$$J = \frac{-dH}{dr} \quad (52)$$

Since the flux varies sinusoidally, then the partial derivative of the magnetic intensity with respect to time can be written as

$$\frac{\partial H}{\partial T} = i \omega H \quad (53)$$

Substituting equation (52) and equation (53) into equation (50) results in

$$\frac{d\mathbf{H}}{dr} = \frac{\omega i \sigma \mu}{R_o} \int_0^{R_o} r \mathbf{H} dr \quad (54)$$

Rearranging equation (54) and doing the integration results in the following differential equation.

$$\frac{d^2\mathbf{H}}{dr^2} + \frac{1}{r} \frac{d\mathbf{H}}{dr} - \mu \omega i \sigma \mathbf{H} = 0 \quad (55)$$

If s is defined as the skin depth

$$s = \sqrt{\frac{2}{\sigma \mu \omega}} \quad (56)$$

and substituted into equation (55), the result is

$$\frac{d^2\mathbf{H}}{dr^2} + \frac{1}{r} \frac{d\mathbf{H}}{dr} - \frac{2i\mathbf{H}}{s^2} = 0 \quad (57)$$

Bessels equation in the general form can be written in the form of equation (58).

$$\frac{d^2y}{dz^2} + \frac{1}{z} \frac{dy}{dz} + \left(k_1^2 + \frac{n^2}{z^2}\right) y = 0 \quad (58)$$

If n is set equal to zero, then the resulting equation is the Bessel's equation zero order.

$$\frac{d^2y}{dz^2} + \frac{1}{z} \frac{dy}{dz} + k_1^2 y = 0 \quad (59)$$

This equation has the same form as equation (55). The solutions to equation (55) are the Bessel functions of the first kind, $J(H)$, and the second kind, $Y(H)$, also called Weber's function. Since $Y(H)$ goes to negative infinity at r equal to zero, it will be deleted from the solution. The magnetic intensity can be written as

$$H = A_1 J_0\left(\sqrt{-1} \frac{\sqrt{2} I}{S}\right) \quad (60)$$

The Bessels equation of the first kind zero order with a complex argument has a solution that is an infinite series of alternating real and imaginary components.

$$\begin{aligned}
 J_0(\sqrt{-1}x) = & 1 + j \frac{x^2}{2^2} - \frac{x^4}{2^2 4^2} - j \frac{x^6}{2^2 4^2 6^2} \\
 & + \frac{x^8}{2^2 4^2 6^2 8^2} + j \frac{x^{10}}{2^2 4^2 4^2 6^2 8^2 10^2} - \dots
 \end{aligned} \tag{61}$$

When the real and imaginary parts of this series are separated and summed they form two series. The real terms form a series which Lord Kelvin named Bessel real ($\text{ber}(x)$), and the imaginary part forms a series called the Bessel imaginary ($\text{bie}(x)$), N. W. McLachlan (26). The solution to equation (61) can be written in terms of the $\text{ber}(x)$ and $\text{bie}(x)$.

$$\mathbf{H} = A_1 \left[\text{ber}\left(\frac{\sqrt{2}r}{s}\right) + i \text{bei}\left(\frac{\sqrt{2}r}{s}\right) \right] \tag{62}$$

From equation (50), the current density, \mathbf{J} , can be found by differentiating equation (62) with respect to r and taking the negative of it.

$$\mathbf{J} = \frac{-\sqrt{2}A_1}{s} \left[\text{ber}'\left(\frac{\sqrt{2}r}{s}\right) + i \text{bei}'\left(\frac{\sqrt{2}r}{s}\right) \right] \tag{63}$$

By dividing the current density with the material conductivity the electric intensity can be calculated.

$$\mathbf{E} = \frac{-\sqrt{2}A_1}{s\sigma} \left[\text{ber}'\left(\frac{\sqrt{2}r}{s}\right) + i\text{bei}\left(\frac{\sqrt{2}r}{s}\right) \right] \quad (64)$$

The constant A_1 in equation (64) is evaluated by using the boundary condition at the surface of the cylinder. The magnetic intensity just outside the cylinder is made up of the impressed intensity, H_0 , and the added intensity set up by the eddy currents flowing within the cylinder. It can be shown that where the radius of the cylinder is small compared to the electromagnetic wave length, the added intensity just outside the cylinder is very nearly equal to the impressed intensity, N. W. McLachlan (26). Therefore, the total magnetic intensity just outside the cylinder is equal to $2H_0$. If equation (65) is evaluated at the surface of the cylinder, then A_1 can be evaluated.

$$2H_0 = A_1 \left[\text{ber}\left(\frac{\sqrt{2}a}{s}\right) + i\text{bei}\left(\frac{\sqrt{2}a}{s}\right) \right] \quad (65)$$

By isolating A_1 , it can be eliminated from equation (65) resulting in

$$\mathbf{H} = 2\mathbf{H}_o \frac{[\text{ber}(\frac{\sqrt{2}r}{s}) + i\text{bei}(\frac{\sqrt{2}r}{s})]}{[\text{ber}(\frac{\sqrt{2}a}{s}) + i\text{bei}(\frac{\sqrt{2}a}{s})]} \quad (66)$$

Whereas the electric intensity is

$$\mathbf{E} = \left[\frac{-\sqrt{2} 2\mathbf{H}_o}{\sigma s} \right] \frac{[\text{ber}(\frac{\sqrt{2}r}{s}) + i\text{bei}(\frac{\sqrt{2}r}{s})]}{[\text{ber}(\frac{\sqrt{2}a}{s}) + i\text{bei}(\frac{\sqrt{2}a}{s})]} \quad (67)$$

Equations (66) and (67) show the variation of the magnetic intensity and electric intensity as a function of position in the cylinder. The next step is to calculate the power generation as a function of position in the cylinder.

The absolute value of the electric intensity is given by equation (68).

$$E = \left[\frac{-\sqrt{2} 2H_0}{\sigma s} \right] \sqrt{\frac{[\text{ber}(\frac{\sqrt{2}r}{s})]^2 + [\text{bei}(\frac{\sqrt{2}r}{s})]^2}{[\text{ber}(\frac{\sqrt{2}a}{s})]^2 + [\text{bei}(\frac{\sqrt{2}a}{s})]^2}} \quad (68)$$

G. H. Brown, C. N. Hoyler and R. A. Bierwirth (27) shows the total power absorbed in the cylinder per unit length is given by

$$P = \int_{r=0}^{r=a} 2\pi E^2 \sigma dr \quad (69)$$

After squaring equation (68) and integrating it the power per unit height results

$$P = \frac{H_0^2 \pi 8\sqrt{2} a}{\sigma s} \frac{\text{ber}(\frac{\sqrt{2}a}{s}) \text{ber}'(\frac{\sqrt{2}a}{s}) + \text{bei}(\frac{\sqrt{2}a}{s}) \text{bei}'(\frac{\sqrt{2}a}{s})}{[\text{ber}(\frac{\sqrt{2}a}{s})]^2 + [\text{bei}(\frac{\sqrt{2}a}{s})]^2} \quad (70)$$

For arguments between -8 and 8, M Abromowitz and I. A. Stegun (28) gives polynomial approximations for the $\text{ber}(x)$, $\text{bei}(x)$, $\text{ber}'(x)$, and $\text{bei}'(x)$ that can be used with

negligible error. The following approximations are used to define the Bessel functions.

$$\begin{aligned} ber(x) = & 1 - 64(x/8)^4 + 113.777(x/8)^8 \\ & - 32.3634(x/8)^{12} + 2.64191(x/8)^{16} + \\ & - .08349(x/8)^{20} + .001225(x/8)^{24} \end{aligned} \quad (71)$$

$$\begin{aligned} bei(x) = & 16(x/8)^2 - 113.7777(x/8)^6 + 72.8177(x/8)^{10} \\ & - 10.5657(x/8)^{14} + .52185(x/8)^{18} \\ & - .01103(x/8)^{22} + .00011(x/8)^{26} \end{aligned} \quad (72)$$

$$\begin{aligned} ber'(x) = & x[-4(x/8)^2 + 14.22222(x/8)^6 \\ & - 6.06814(x/8)^{10} + .66047(x/8)^{14} \\ & - .02609(x/8)^{18} + .00045(x/8)^{22} \end{aligned} \quad (73)$$

$$\begin{aligned} bei'(x) = & x[1/2 - 10.66666(x/8)^4 + 11.37777(x/8)^8 \\ & - 2.31167(x/8)^{12} + .14677(x/8)^{16} \\ & - .00379(x/8)^{20} + .00004(x/8)^{24} \end{aligned} \quad (74)$$

The power delivered to a cylindrical load can be calculated from a derivation developed by J. T. Vaughan(8). In his paper, J. T. Vaughan develops two important equations. The first is the voltage drop across a set of induction coils, and the second is the efficiency of the induction coil at inducing power in the load. The coil resistance, A_1 , is defined as

$$A_1 = \frac{3.14 \rho_1 b_1}{\alpha L} \left[\frac{1}{d_1} + \frac{1}{b_1} \right] \quad (75)$$

where ρ_1 is equal to the resistivity of conductor material. The variables b_1 , α , and L are the inside diameter of the coil, space factor, and the axial length of the inductor coil, respectively. The d_1 term is the reference depth for the inductor, a measure of current penetration, and it is defined as

$$d_1 = 3,160 \sqrt{\frac{2 \pi \rho_1}{\omega \alpha}} \quad (76)$$

The next constant is A_2 , which is the load resistance divided by N^2 , where N is the total turns in coil and A_2 is defined by equation (77).

$$A_2 = \frac{3.14 \rho_2 a_o K_2 K_1^2}{L d_2} \quad (77)$$

where ρ_2 is the resistivity of the load material, and d_2 is the reference depth of the load material. K_1 and K_2 are constants based on the geometry of the induction press. The next constant A_3 is the internal reactance of the coil divided by N^2 . A_3 is defined as

$$A_3 = \frac{3.14 \rho_1 b_1}{\alpha L d_1} \quad (78)$$

A_4 , internal reactance of the load divided by N^2 , is defined as

$$A_4 = \frac{3.14 \rho_2 a_o K_1^2}{L D_2} \quad (79)$$

The final constant A_5 , air-gap reactance divided by N^2 , is defined as

$$A_5 = \frac{15.7 \omega (b_1^2 - a_o^2) K_1 10^{-8}}{2 \pi L} \quad (80)$$

For a set number of turns, geometry, and power input to the coil an expected voltage drop across the coil can be calculated from equation (81).

$$E_L = \frac{N}{\sqrt{\frac{A_1 + A_2}{P_L [(A_1 + A_2)^2 + (A_3 + A_4 + A_5)^2]}}} \quad (81)$$

The power dissipated to the load can be calculated by multiplying the power to the coil by the ratio of the resistance of the load, divided by the total resistance.

$$P_L = P_S \left[\frac{A_2}{A_1 + A_2} \right] \quad (82)$$

The efficiency of the system is defined as

$$\eta = \frac{A_2}{A_1 + A_2} \quad (83)$$

If equation (82) is divided by the height of the graphite cylinder, then the magnetic intensity, H_o , can be estimated.

$$\phi = \frac{\pi 8 \sqrt{2} a}{\sigma s} \frac{\text{ber}\left(\frac{\sqrt{2}a}{s}\right) \text{ber}'\left(\frac{\sqrt{2}a}{s}\right) + \text{bei}\left(\frac{\sqrt{2}a}{s}\right) \text{bei}'\left(\frac{\sqrt{2}a}{s}\right)}{\left[\text{ber}\left(\frac{\sqrt{2}a}{s}\right)\right]^2 + \left[\text{bei}\left(\frac{\sqrt{2}a}{s}\right)\right]^2} \quad (84)$$

$$H_o = \sqrt{\frac{P_L}{h\phi}} = \sqrt{\frac{P}{\phi}} \quad (85)$$

Once H_o is determined, then the electric intensity as a function of position can be determined from equation (68).

The heat generation as a function of position is then given by

$$\dot{Q}(r) = E^2 \sigma \quad (86)$$

The graphite cylinder can be segregated into thin walled cylinders. If the wall thickness is small enough, the variation of the heat generation term in that cylinder can be considered linear. Therefore, the heat generated in each cylinder can be estimated by calculating the heat generation value at the boundaries of the cylinder and averaging these values for the domain within the cylinder. If this average heat generation value is multiplied by the volume of the cylinder shell and summed over the entire body, the error associated with this approximation can be estimated. Provided that the error is acceptable, the individual heat generation terms can be interfaced with the finite element code as a material property for that domain of the total cylinder being inductively heated.

APPENDIX II

VERIFICATION OF THE Dot CODE USING SAMPLE PROBLEMS

Steady State Heat Conduction Through an Infinite Plane Wall

The Dot code was checked by analyzing problems where the analytical solutions were known. The first problem analyzed by the Dot code was conduction through a plane wall, Figure 34. In this problem, T_1 was set to 100 °C and T_2 was set to 0 °C. The thermal conductivity was 1 W/(cm °C). With the assumption of a steady state conduction through an infinite plane wall, the heat diffusion equation becomes:

$$\frac{dT}{dx} \left(k \frac{dT}{dx} \right) = 0 \quad (87)$$

T Temperature, C

X Length, m

Applying the boundary condition, results in the analytical solution:

$$T(x) = \left(\frac{T_2 - T_1}{L} \right) x + T_1 \quad (88)$$

T_1 Boundary temperature 1, C

T_2 Boundary temperature 2, C

L Total length, m

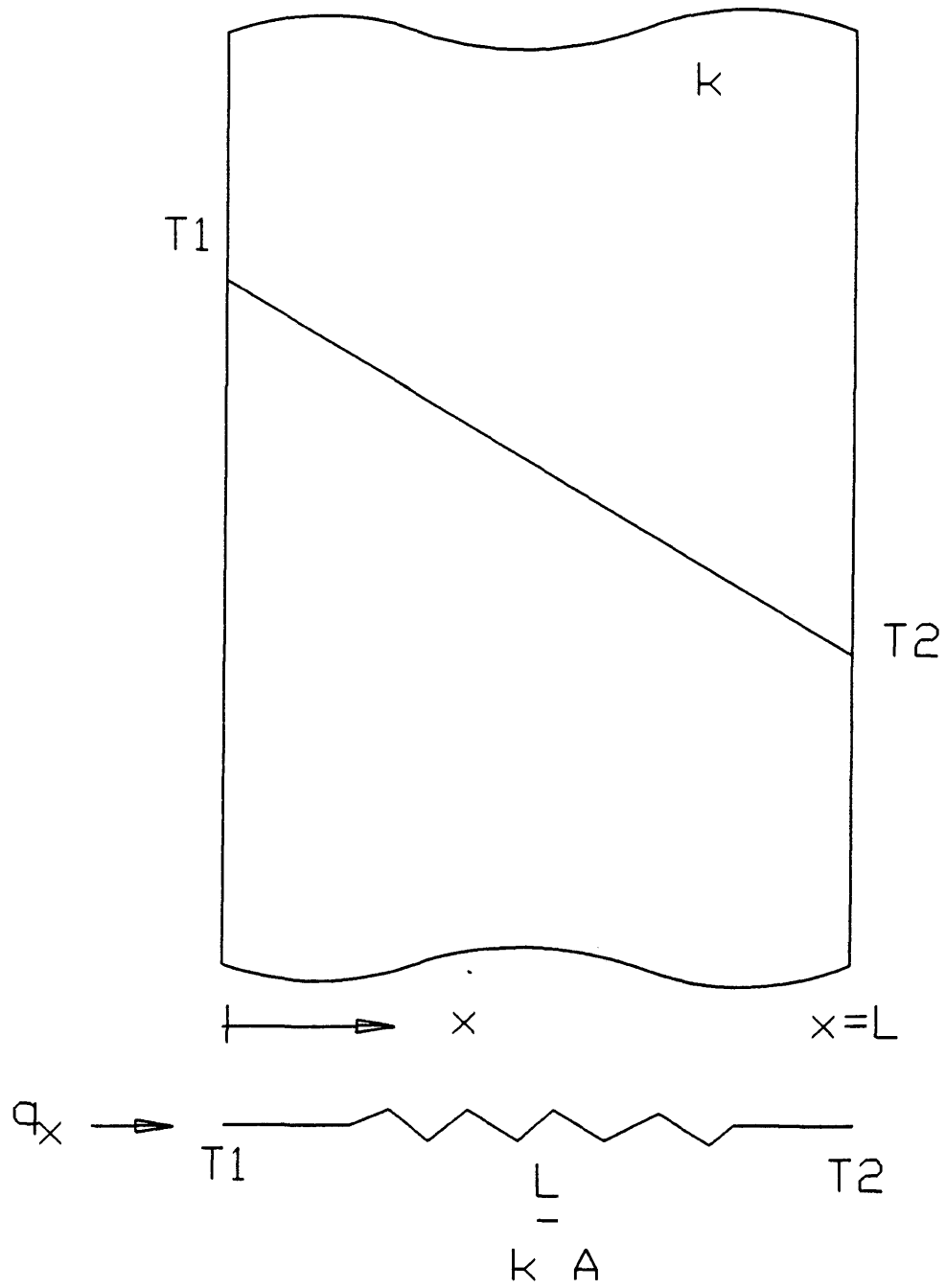


Figure 34 Conduction Through an Infinite Plane Wall

The Dot input data file was:

```

420--05C-02
START 11/4/90 SAMPLE PROBLEM 1 CONDUCTION IN A INFINITE
PLANE WALL
  22  1  0  1
  1
  11  10  0  1
  12  0  1  1
  22  10  1
 -1  1  30  0  25  1
  0  0  4
  1  1  1  100.0
  2  11  1  0.0
  3  12  1  100.0
  4  22  1  0.0
  0
  1  10  1  1  4  2  1  1  0
  1  1  0  0.0
  1  1  1  0  0
  1  13  12  1  2  1
 10  22  21  10  11  1
STOP

```

The format for this file is explained in the Dot manual. The results of the analytical and numerical solutions are presented in Figure 35. The agreement of the Dot values to the analytical values are within five significant figures.

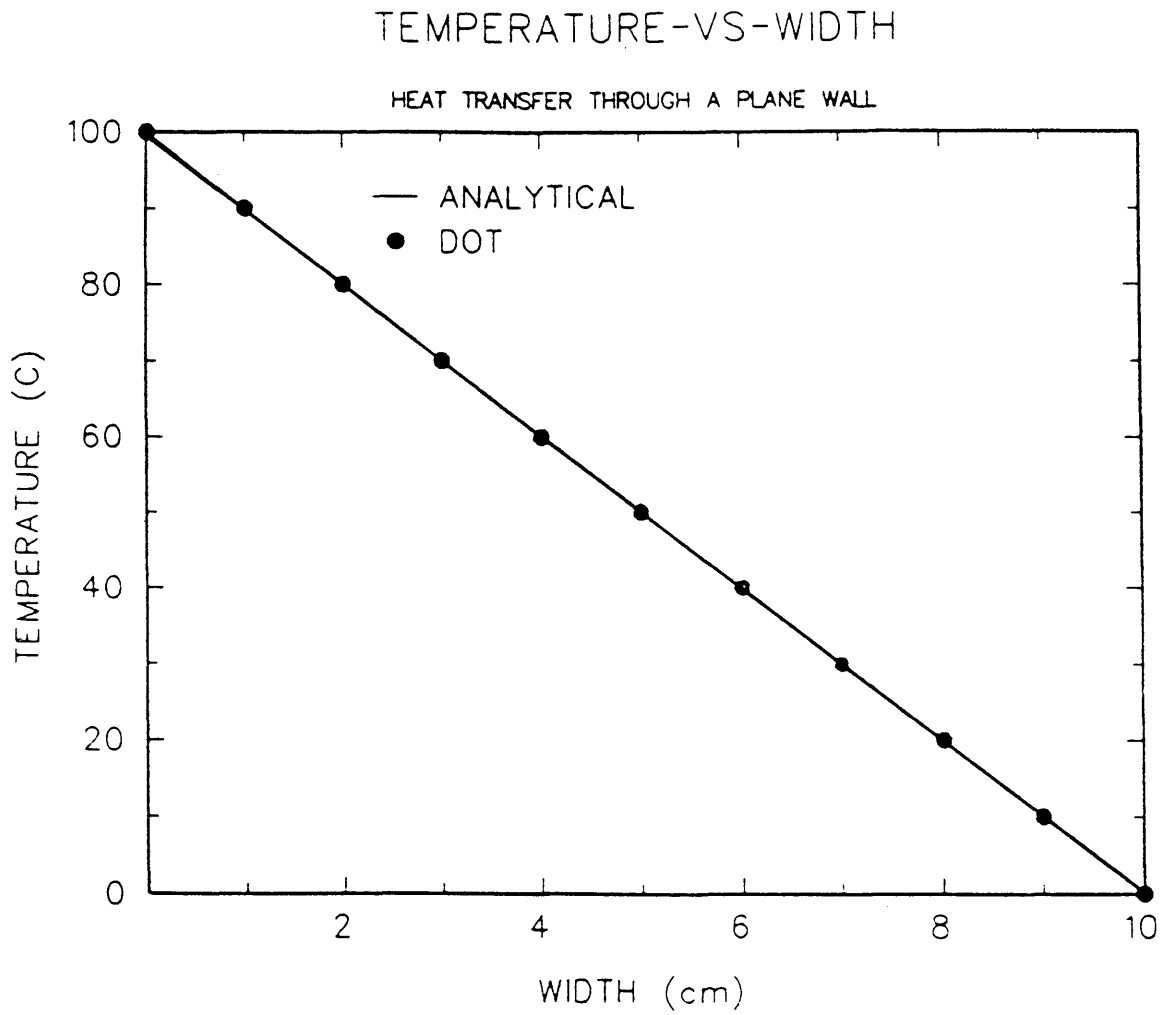


Figure 35 Temperature-vs-Width for an Infinite Plane Wall under Steady State Conditions.

Steady State Heat Conduction Through a Plane Composite Wall

The next problem analyzed by Dot was steady state conduction through an infinite plane composite wall, Figure 36. The thermal conductivity for section A was chosen to be 2 W/(cm °C). The thermal conductivity for section B was 1 W/(cm °C). The T_1 was set to 100 °C and T_3 was set to 0 °C. L_A was set equal to L_B which was 5 cm.

Applying the temperature boundary conditions and realizing that the heat flux at the material interface is constant, the following analytical solution is obtained:

$$T(x) = \left(\frac{T_2 - T_1}{L_A} \right) x + T_1 \quad 0 < x < L_A \quad (89)$$

$$T(x) = \left(\frac{T_3 - T_2}{L_B} \right) (x - L_A) + T_2 \quad L_A < x < (L_A + L_B) \quad (90)$$

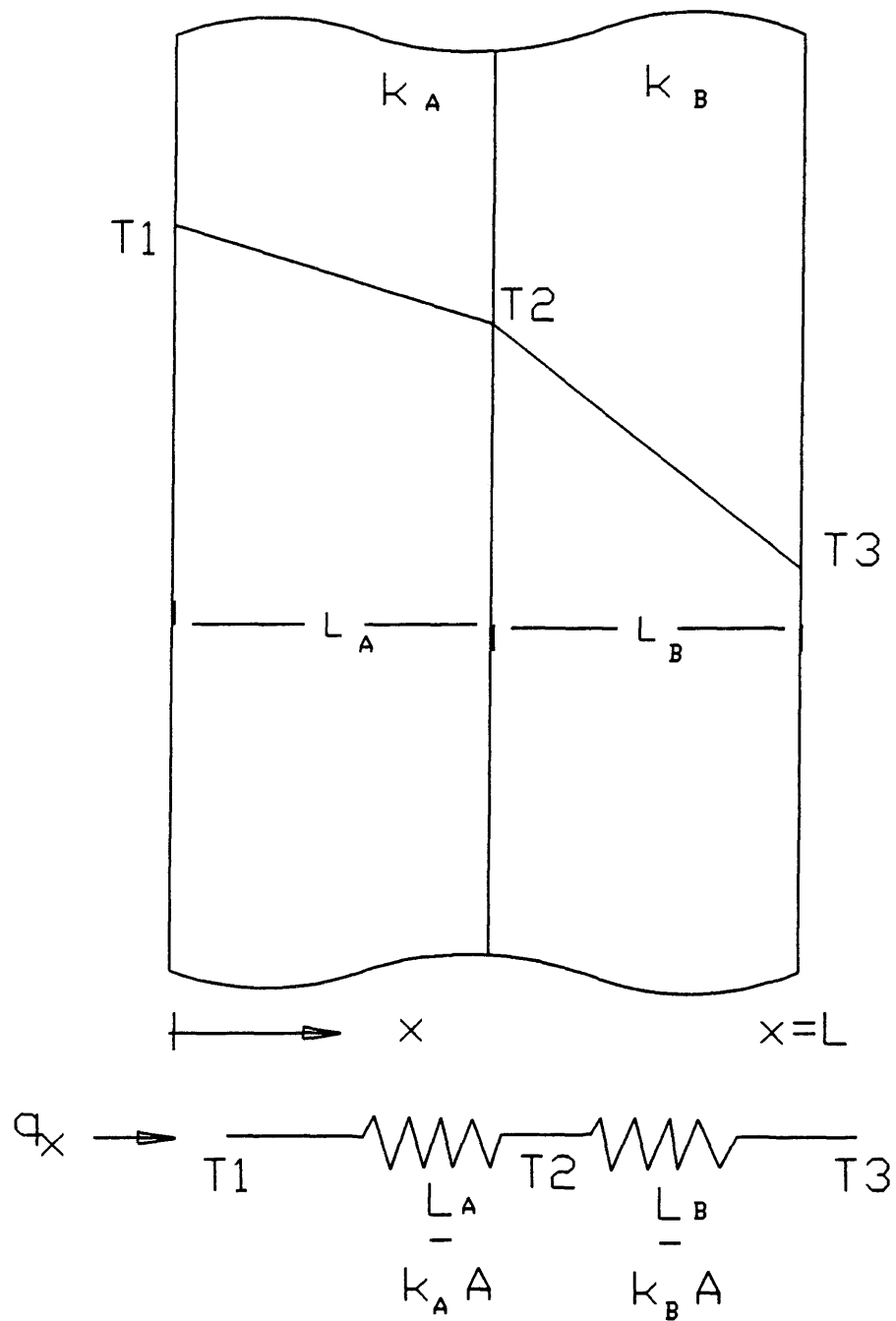


Figure 36 Steady State Conduction Through an Infinite Composite Wall.

The Dot input date file was:

420--05C-02

START 11/4/90 SAMPLE PROBLEM 2 CONDUCTION IN A INFINITE

PLANE COMPOSITE WALL

22	1	0	1						
1			0		0		1		
11			10		0				
12			0		1		1		
22			10		1				
-1	1		30		0		25		1
0	0	4							
1	1	1			100.0				
2	11	1			0.0				
3	12	1			100.0				
4	22	1			0.0				
0									
1	10	1	1	4	2	2	1	0	
1				1	0		0.0		
			2		2		0		0
2				1	0		0.0		
			1		1		0		0
1	13	12	1	2					1
5	17	16	5	6					1
6	18	17	6	7					2
10	22	21	10	11					2

STOP

The results of the analytical and numerical solutions are presented in Figure 37. The agreement of the Dot values to the analytical values are within five significant figures.

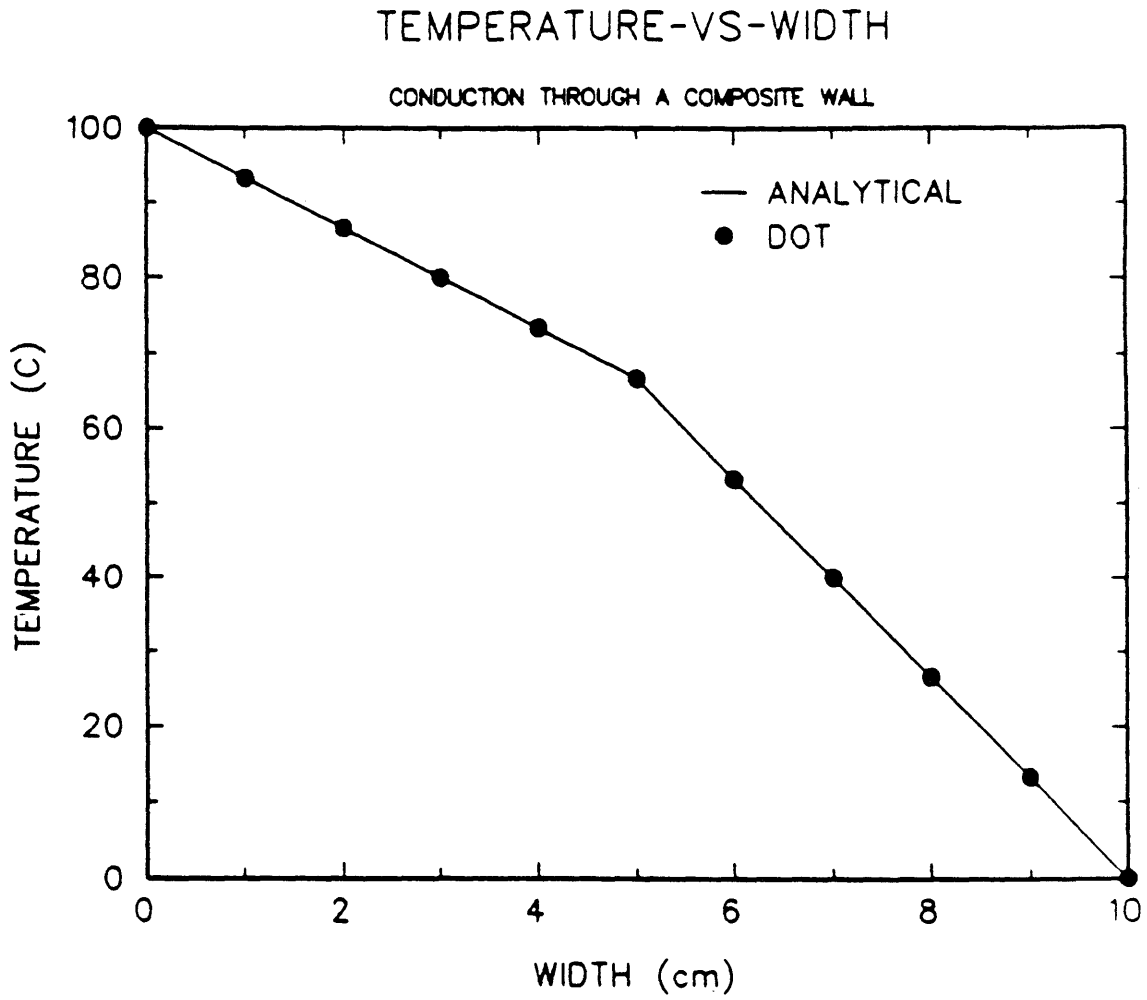


Figure 37 Temperature-vs-Width for a Steady State Infinite Plane Composite Wall.

Steady State Heat Generation in a Plane Composite Wall

The next problem analyzed by Dot was steady state heat generation in an infinite plane composite wall, Figure 38. The heat generation in A was set to 2 W/cc and in B 1 W/cc. The T_1 was set to 100 °C and T_3 was set to 0 °C. L_A was set equal to L_B which was 5 cm. The resulting analytical solutions for this problem and materials were:

$$T(x) = T_2 + 25 - x^2 \quad 0 < x < L_A \quad (91)$$

$$T(x) = 100 - \frac{x^2}{2} - 5x \quad L_A < x < (L_A + L_B) \quad (92)$$

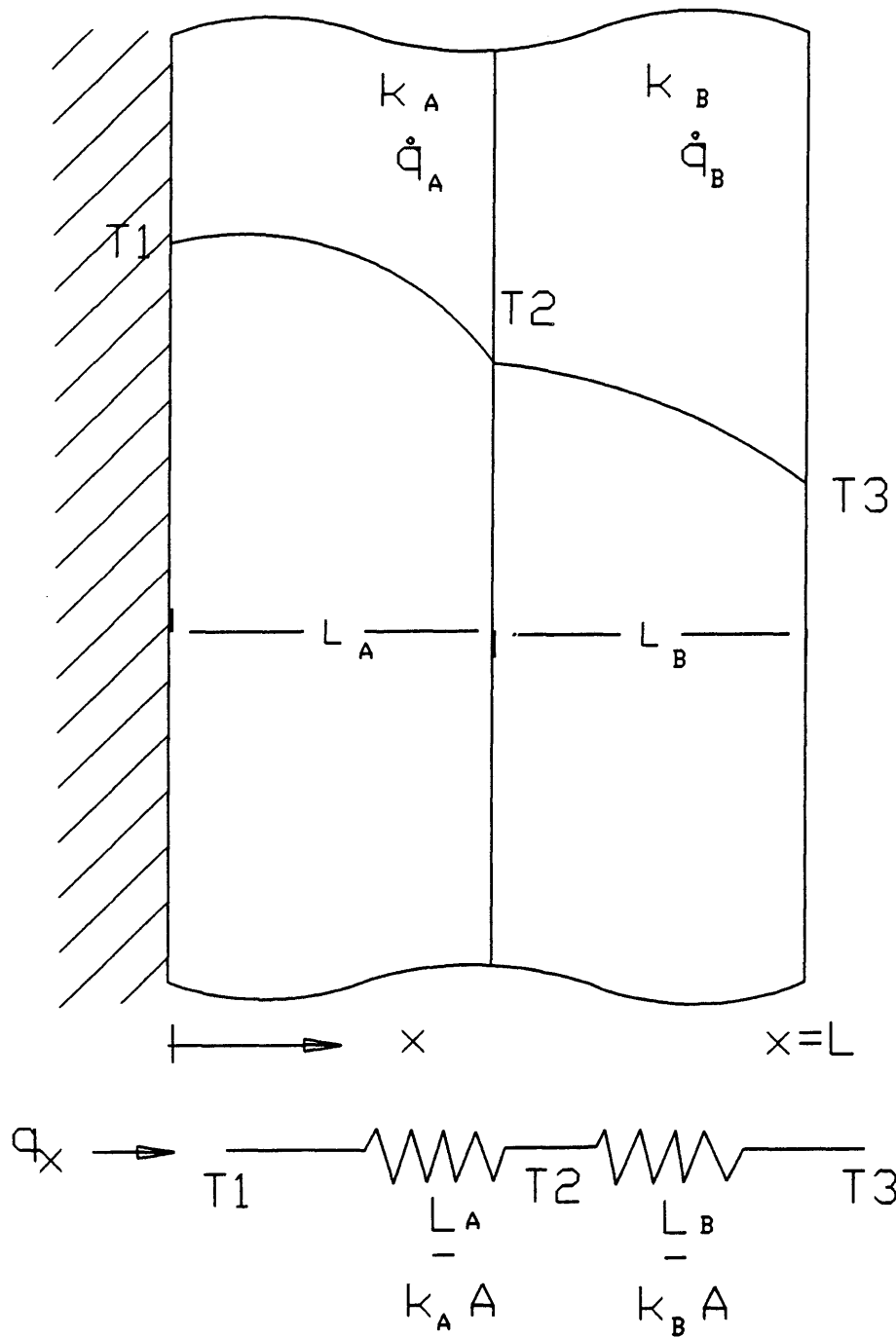


Figure 38 Heat generation in an Infinite Composite Wall.

The Dot input data file was:

```

420--05C-02
START 11/4/90 SAMPLE PROBLEM 3 INFINITE COMPOSITE WALL
WITH HEAT GENERATION
  22  1  0  1
  1      0  0  1
 11      10  0
 12      0  1  1
 22      10  1
-1  1  30  0  25  1
  0  0  2
  1 11  1  0.0
  2 22  1  0.0
  0
  1 10  1  1  4  2  2  1  1
  1      1  0  2
      1  1  0  0
  2      1  0  1
      1  1  0
  1 13 12  1  2  1
  5 17 16  5  6  1
  6 18 17  6  7  2
 10 22 21 10 11  2
STOP

```

The results of the analytical and numerical solutions are presented in Figure 39. The Dot results for this problem were not as accurate as for the previous problems. The Dot predicated temperature values were good to three significant figures.

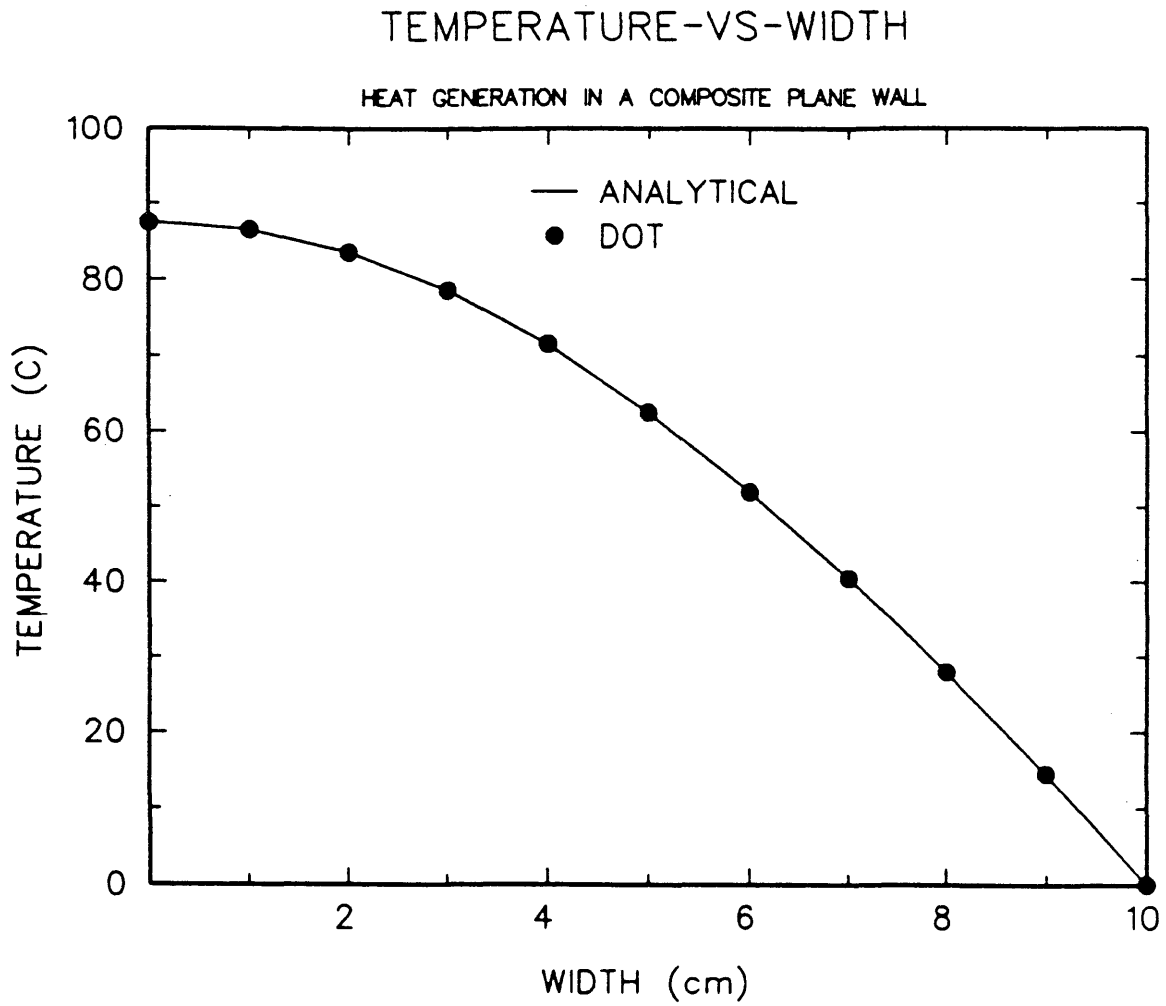


Figure 39 Temperature-vs-Width for a Steady State Infinite Plane Composite Wall with Heat Generation.

Steady State Heat Generation in a Composite Cylinder

The next problem analyzed by Dot was steady state heat generation in an infinite composite cylinder, Figure 40. The heat generation in A was set to 2 W/cc and in B 1 W/cc. The T_1 was set to 100 °C and T_3 was set to 0 °C. R_A was set equal to R_B which was 5 cm. The resulting analytical solutions for this problem and materials were:

$$T(r) = \left(\frac{-r^2}{2}\right) + T_2 + 12.5 \quad 0 < r < R_A \quad (93)$$

$$T(r) = \left(\frac{-r^2}{4}\right) - 12.5 \ln(r) + 53.78 \quad R_A < r < (R_A + R_B) \quad (94)$$

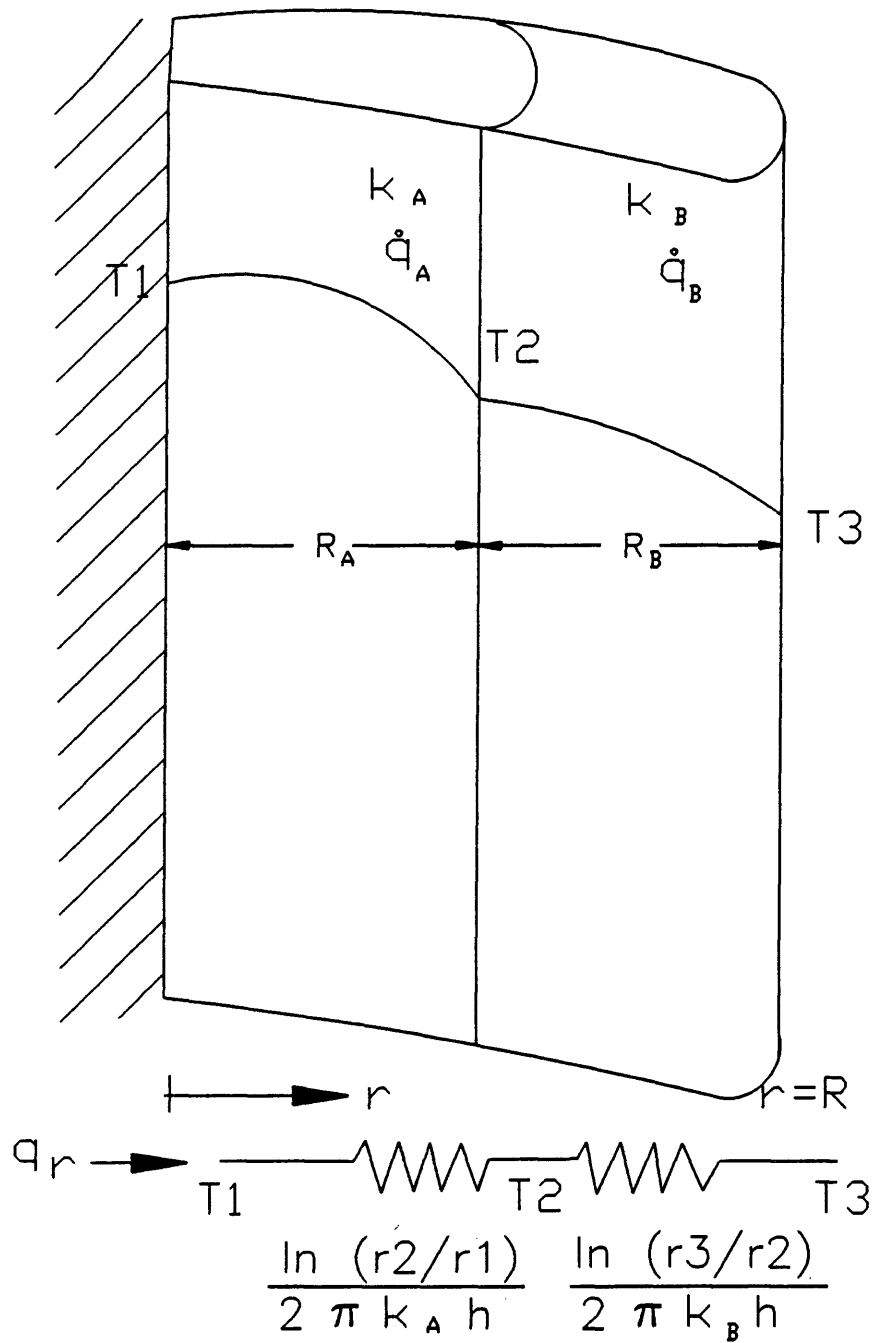


Figure 40 Heat Generation in an Infinite Composite Cylinder

The Dot input data file was:

420--05C-02

START 11/4/90 SAMPLE PROBLEM 4 INFINITE COMPOSITE CYLINDER
WITH HEAT GENERATION

22	1	0	1						
1			0		0	1			
11			10		0				
12			0		1	1			
22			10		1				
-1	1		30		0		25		1
0	0	2							
1	11	1			0.0				
2	22	1			0.0				
0									
1	10	1	0	4	2	2	1	1	
1				1	0		2		
			1		1		0		0
2				1	0		1		
			1		1		0		0
1	13	12	1	2					1
5	17	16	5	6					1
6	18	17	6	7					2
10	22	21	10	11					2

STOP

The results of the analytical and numerical solutions are presented in Figure 41. The results of the Dot predicted temperatures agreed with the analytical solution to within three significant figures indicating that the Dot temperatures are within experimental error of this analysis.

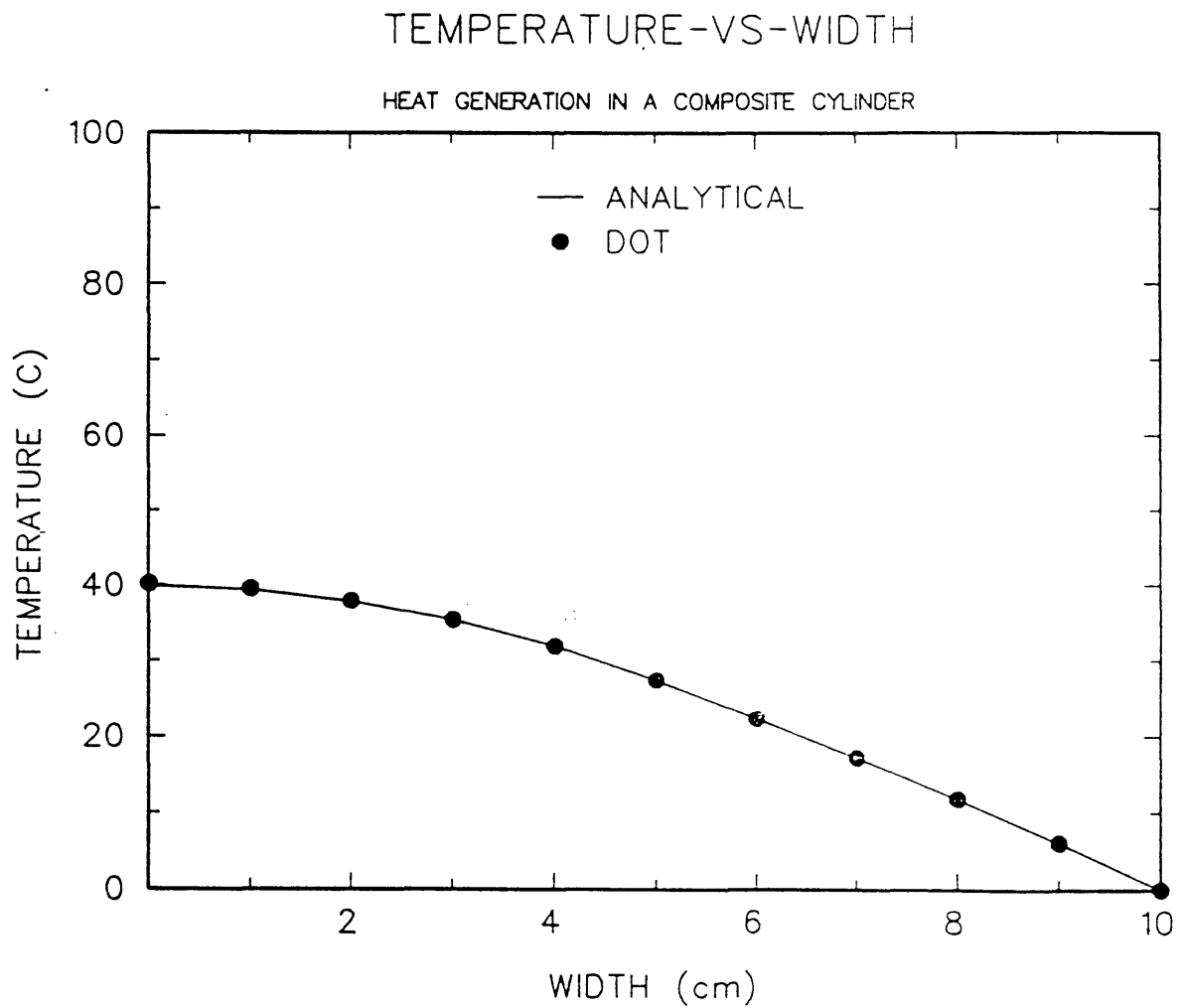


Figure 41 Temperature-vs-Width for a Steady State Infinite Composite Cylinder with Heat Generation.

APPENDIX III

Lotus Spreadsheet Equations for Heat Generation Calculations

For a detailed development of these equations refer to Appendix I. The coil resistance, A_1 , is defined as

$$A_1 = \frac{3.14 \rho_1 b_1}{\alpha L} \left[\frac{1}{d_1} + \frac{1}{b_1} \right] \quad (95)$$

ρ_1	Resistivity of conductor material, Ohms/m
b_1	Inside diameter of the coil, m
α	Space factor
L	Axial length of the inductor coil, m

The d_1 term is the reference depth for the inductor, a measure of current penetration, and it is defined as

$$d_1 = 3,160 \sqrt{\frac{\rho_1}{f \alpha}} \quad (96)$$

f	Frequency, rad/sec
-----	--------------------

The next constant is A_2 , which is the load resistance divided by N^2 , where N is the total turns in coil and A_2 is defined by equation (97).

$$A_2 = \frac{3.14 \rho_2 a_o K_2 K_1^2}{L d_2} \quad (97)$$

ρ_2	Resistivity of the load material, Ohms/m
d_2	Reference depth of the load material, m

a_o	Graphite die diameter, m
K_1	Constant based on the geometry
K_2	Constant based on the geometry
A_3	Internal reactance of the coil divided by N^2 , Ohms

A_3 is defined as

$$A_3 = \frac{3.14 \rho_1 b_1}{\alpha L S} \quad (98)$$

A_4 , internal reactance of the load divided by N^2 , is defined as

$$A_4 = \frac{3.14 \rho_2 a_o K_1^2}{L d_2} \quad (99)$$

The final constant A_5 , air-gap reactance divided by N^2 , is defined as

$$A_5 = \frac{15.7 \omega (b_1^2 - a_o^2) K_1 10^{-8}}{2 \pi L} \quad (100)$$

For a set number of turns, geometry, and power input to the coil an expected voltage drop across the coil can be calculated from equation (101).

$$E_L = \frac{N}{\sqrt{\frac{A_1 + A_2}{P_L [(A_1 + A_2)^2 + (A_3 + A_4 + A_5)^2]}}} \quad (101)$$

The power dissipated to the load can be calculated by multiplying the power to the coil by the ratio of the resistance of the load, divided by the total resistance.

$$P_L = P_S \left[\frac{A_2}{A_1 + A_2} \right] \quad (102)$$

The efficiency of the system is defined as

$$\eta = \frac{A_2}{A_1 + A_2} \quad (103)$$

The power per unit height is given by

$$P = \frac{P_L}{h} \quad (104)$$

The magnetic intensity is a function of Bessel functions and the power per unit length.

$$\phi = \frac{\pi 8 \sqrt{2} a}{\sigma s} \frac{\text{ber}(\frac{\sqrt{2}a}{s}) \text{ber}'(\frac{\sqrt{2}a}{s}) + \text{bei}(\frac{\sqrt{2}a}{s}) \text{bei}'(\frac{\sqrt{2}a}{s})}{[\text{ber}(\frac{\sqrt{2}a}{s})]^2 + [\text{bei}(\frac{\sqrt{2}a}{s})]^2} \quad (105)$$

$$H_o = \sqrt{\frac{P_L}{h\phi}} = \sqrt{\frac{P}{\phi}} \quad (106)$$

The following approximations are used to define the Bessel functions.

$$\begin{aligned} ber(x) = & 1 - 64(x/8)^4 + 113.777(x/8)^8 \\ & - 32.3634(x/8)^{12} + 2.64191(x/8)^{16} + \\ & - .08349(x/8)^{20} + .001225(x/8)^{24} \end{aligned} \quad (107)$$

$$\begin{aligned} bei(x) = & 16(x/8)^2 - 113.7777(x/8)^6 + 72.8177(x/8)^{10} \\ & - 10.5657(x/8)^{14} + .52185(x/8)^{18} \\ & - .01103(x/8)^{22} + .00011(x/8)^{26} \end{aligned} \quad (108)$$

$$\begin{aligned} ber'(x) = & x[-4(x/8)^2 + 14.22222(x/8)^6 \\ & - 6.06814(x/8)^{10} + .66047(x/8)^{14} \\ & - .02609(x/8)^{18} + .00045(x/8)^{22} \end{aligned} \quad (109)$$

$$\begin{aligned} bei'(x) = & x[1/2 - 10.66666(x/8)^4 + 11.37777(x/8)^8 \\ & - 2.31167(x/8)^{12} + .14677(x/8)^{16} \\ & - .00379(x/8)^{20} + .00004(x/8)^{24} \end{aligned} \quad (110)$$

Once the magnetic intensity is known then it can be used to calculate the electric intensity as a function of position.

$$E = \left[\frac{-\sqrt{2} * 2H_o}{\sigma s} \right] \sqrt{\frac{[ber(\frac{\sqrt{2}r}{s})]^2 + [bei(\frac{\sqrt{2}r}{s})]^2}{[ber(\frac{\sqrt{2}a}{s})]^2 + [bei(\frac{\sqrt{2}a}{s})]^2}} \quad (111)$$

The heat generation can be calculated by

$$\dot{Q}(r) = E^2 \sigma \quad (112)$$

Tables 8 is a Lotus spread sheet that calculates the heat generation for this analysis based on the previous equations.

Table 8

Lotus Spreadsheet for Heat Generation Calculations

THIS SPREAD SHEET IS DESIGNED TO CALCULATE THE HEAT GENERATION TERM IN AN INDUCTIVLY HEATED GRAPHITE DIE. IT WAS WRITTEN ON 8/20/90 BY TIMOTHY J. LEWIS.

THE PERMITTIVITY IS FOR A VACUUM.

TEMPERATURE OF THE MATERIAL MUST BE BETWEEN 1000 C AND 2800 C.

***** INPUT FOR THE SPREAD SHEET *****

FREQUENCY (Hz)	PERMIT- TIVITY (farads)	TEMP. (C)	POWER INPUT Watts	COPPER RESITIVITY (ohm-cm)	RADIUS OF CYLINDER (cm)
9.50E+03	8.85E-14	1.50E+03	5.00E+03	1.68E-06	5.398
SPACE FACTOR	DIE HEIGHT (in)	# OF COIL TURNS	K5 NAGAOKA'S CONSTANT	COIL ID (in)	K2 RESISTANC COEFFECIENT
7.50E-01	7.00E+00	7.00E+00	7.20E-01	7.00E+00	8.50E-01
CYLINDER DIA (in)	k2				
4.25E+00	8.50E-01				

***** CALCULATED VALUES *****

GRAPHITE RESITIVITY (ohm-cm)	d1 (in)	d2 (in)	K1	RADIUS/d2	
1.12E-03	3.04E-02	6.80E-01	8.23E-01	6.25E+00	
A1	A2	A3	A4	A5	
9.13E-05	7.10E-04	9.09E-05	8.35E-04	5.43E-03	
THE REQUIRED EMF EL (volts)	EFFICIENCY nu	POWER DELIVERED TO THE LOAD (Watts)			
1.12E+02	8.86E-01	4430.34			
PENETRATION TERM "s" cm	POWER FACTOR	BESSEL FUNCTION ARGUEMENT RADIUS	IF -8 < ARGUMENT < 8 THEN POLYNOMIAL APPROXIMATIONS FOR THE BESSEL FUNCTIONS ARE RESEANABLE.		
1.22E+00	1.00E+00	6.26E+00	BESSEL RADICAL Ho	MAGNETIC INTENSITY Ho	
AG = {[(2^0.5)*a]/s}			1.60	47.67	
RADIUS "a" (cm)	BESSEL ARGUMENT FOR "a" = AG	ber(AG)	bei(AG)	ber'(AG)	bei'(AG)
5.40E+00	6.26E+00	-8.66	-10.36	1.95	-12.62

Table 8

Lotus Spreadsheet for Heat Generation Calculations

RADIUS (cm)	BESSEL ARGUMENT	ber(x)	bei(x)	ber'(x)	bei'(x)
0.00E+00	0.00E+00	1.00E+00	0.00E+00	0.00E+00	0.00E+00
2.50E-01	2.90E-01	1.00E+00	2.10E-02	-1.52E-03	1.45E-01
5.00E-01	5.80E-01	9.98E-01	8.40E-02	-1.22E-02	2.90E-01
7.50E-01	8.70E-01	9.91E-01	1.89E-01	-4.11E-02	4.33E-01
1.00E+00	1.16E+00	9.72E-01	3.35E-01	-9.73E-02	5.74E-01
1.25E+00	1.45E+00	9.31E-01	5.21E-01	-1.90E-01	7.08E-01
1.50E+00	1.74E+00	8.58E-01	7.44E-01	-3.26E-01	8.28E-01
1.75E+00	2.03E+00	7.37E-01	9.99E-01	-5.14E-01	9.25E-01
2.00E+00	2.32E+00	5.54E-01	1.28E+00	-7.60E-01	9.86E-01
2.25E+00	2.61E+00	2.91E-01	1.57E+00	-1.07E+00	9.94E-01
2.50E+00	2.90E+00	-6.93E-02	1.85E+00	-1.43E+00	9.26E-01
2.75E+00	3.19E+00	-5.43E-01	2.09E+00	-1.85E+00	7.59E-01
3.00E+00	3.48E+00	-1.14E+00	2.27E+00	-2.30E+00	4.64E-01
3.25E+00	3.77E+00	-1.88E+00	2.35E+00	-2.77E+00	8.62E-02
3.50E+00	4.06E+00	-2.75E+00	2.26E+00	-3.22E+00	-6.37E-01
3.75E+00	4.35E+00	-3.74E+00	1.96E+00	-3.60E+00	-1.50E+00
4.00E+00	4.64E+00	-4.82E+00	1.37E+00	-3.85E+00	-2.61E+00
4.25E+00	4.93E+00	-5.95E+00	4.18E-01	-3.88E+00	-3.97E+00
4.50E+00	5.22E+00	-7.04E+00	-9.62E-01	-3.60E+00	-5.59E+00
4.75E+00	5.51E+00	-7.99E+00	-2.84E+00	-2.88E+00	-7.42E+00
5.00E+00	5.80E+00	-8.66E+00	-5.28E+00	-1.60E+00	-9.41E+00
5.25E+00	6.09E+00	-8.85E+00	-8.30E+00	3.86E-01	-1.15E+01
5.40	6.26	-8.66	-10.37	1.95	-12.63

Table 8

Lotus Spreadsheet for Heat Generation Calculations

BESSEL RADICAL	ELECTRIC INTENSITY (volts/cm)	RADIUS (cm)	HEAT GENERATION (Watts/cc)	HEAT TOTAL BESSEL
0.00E+00	0.00E+00	0.00E+00	0.00E+00	1.64E-02
1.07E-02	3.24E-03	2.50E-01	9.42E-03	2.47E-01
2.15E-02	6.49E-03	5.00E-01	3.77E-02	1.07E+00
3.22E-02	9.74E-03	7.50E-01	8.50E-02	2.90E+00
4.31E-02	1.30E-02	1.00E+00	1.52E-01	6.73E+00
5.43E-02	1.64E-02	1.27E+00	2.41E-01	1.16E+01
6.59E-02	1.99E-02	1.52E+00	3.55E-01	1.97E+01
7.84E-02	2.37E-02	1.77E+00	5.03E-01	3.17E+01
9.22E-02	2.79E-02	2.02E+00	6.95E-01	4.93E+01
1.08E-01	3.26E-02	2.27E+00	9.51E-01	7.53E+01
1.26E-01	3.81E-02	2.52E+00	1.30E+00	1.14E+02
1.48E-01	4.47E-02	2.77E+00	1.79E+00	1.58E+02
1.74E-01	5.25E-02	3.00E+00	2.47E+00	2.58E+02
2.05E-01	6.20E-02	3.25E+00	3.44E+00	3.90E+02
2.43E-01	7.35E-02	3.50E+00	4.83E+00	5.91E+02
2.89E-01	8.73E-02	3.75E+00	6.83E+00	8.95E+02
3.44E-01	1.04E-01	4.00E+00	9.70E+00	1.36E+03
4.11E-01	1.24E-01	4.25E+00	1.38E+01	2.06E+03
4.92E-01	1.49E-01	4.50E+00	1.98E+01	3.12E+03
5.89E-01	1.78E-01	4.75E+00	2.84E+01	4.72E+03
7.07E-01	2.14E-01	5.00E+00	4.09E+01	7.14E+03
8.49E-01	2.56E-01	5.25E+00	5.89E+01	6.18E+03
1.00	0.30	5.40	81.86	
			SUM =	27167.73
			ACTUAL =	26582.02
			%ERROR=	2.20

APPENDIX IV

Calibration Data for Load Cell

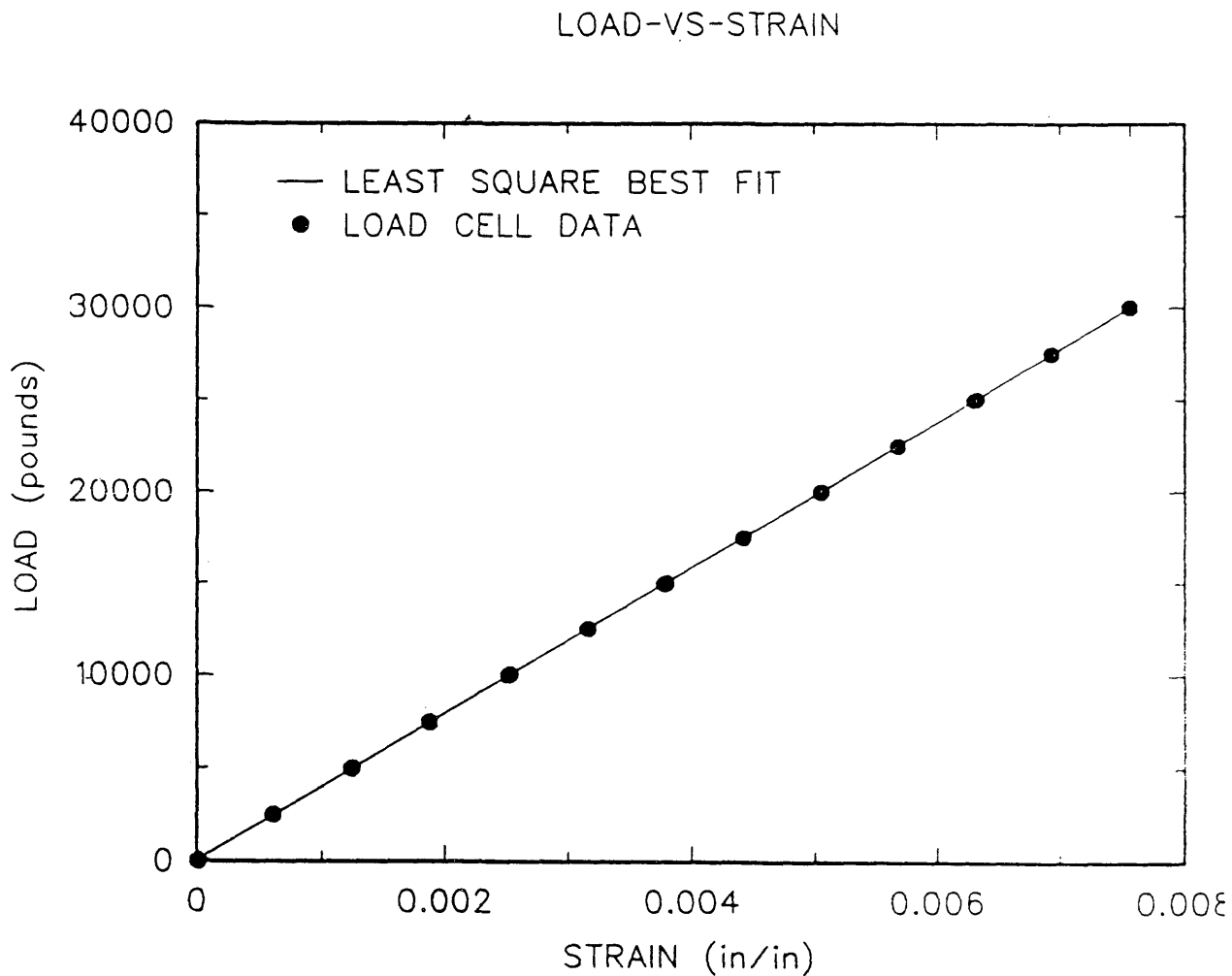


Figure 42 Load Cell Stress-Strain Curve Used in the Hydraulic System Calibration of the Hot Press.

APPENDIX V

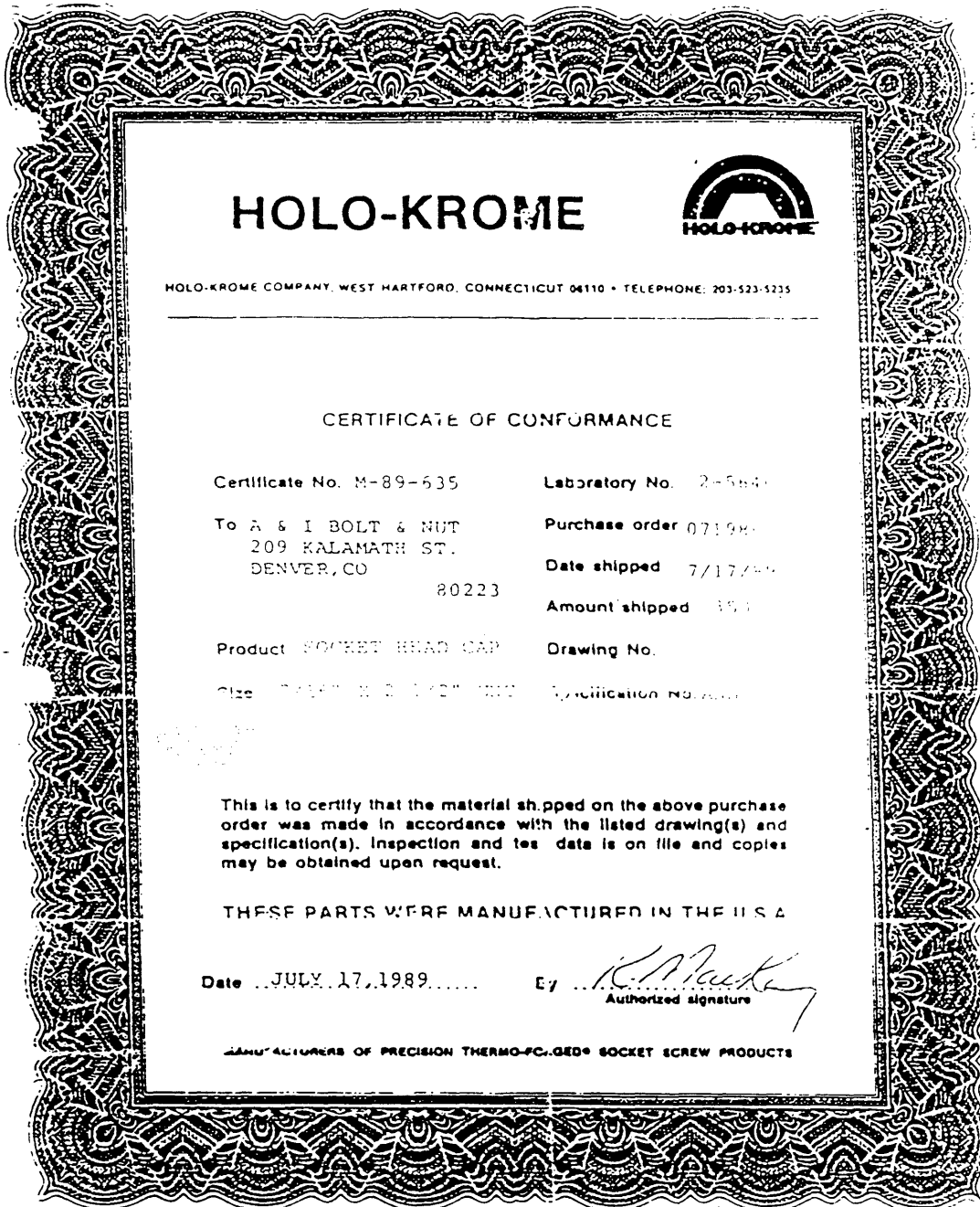


Figure 43 Certificate of Conformance for Grade 8 Bolts Used in the Hydraulic Press Construction

APPENDIX VI

STANDARD OPERATING PROCEDURE FOR HOT PRESS

This procedure manual has been written for operation of the hot press at the Colorado Center for Advanced Ceramics.

Written by: Timothy J. P. Lewis 1/8/91
Date

Reviewed by: Keith M. Axler 1-8-91
Date

Approved by: Gerald L. DePoorter 1/8/91
Date

Hot Press System

The induction hot press system consists of several components:

- 1) Hot press stack and package,
- 2) The hydraulic press and hydraulic system,
- 3) Radio frequency generator, induction coil, and Vacuum system.

The hydraulic press and hydraulic system provide the pressing force to be applied to the hot press stack. The hot press stack consists of the graphite die and punches. The hot press package encases the hot press stack and provides either a vacuum or controlled atmosphere for the graphite die as well as providing a means of transmitting the force to the stack. The hot press package also provides support for the induction coil.

Figure 44 is a block diagram showing the positioning of these various components in the laboratory and indicating utility requirements.

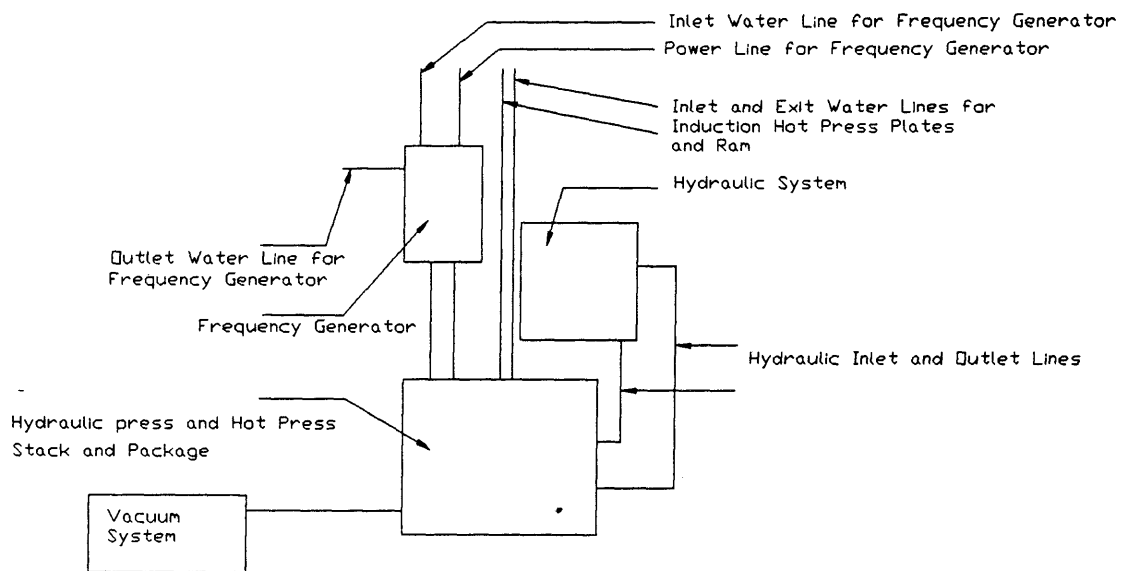


Figure 44 Block Diagram of the Induction Hot Press System

Figure 45 is a drawing of the system.

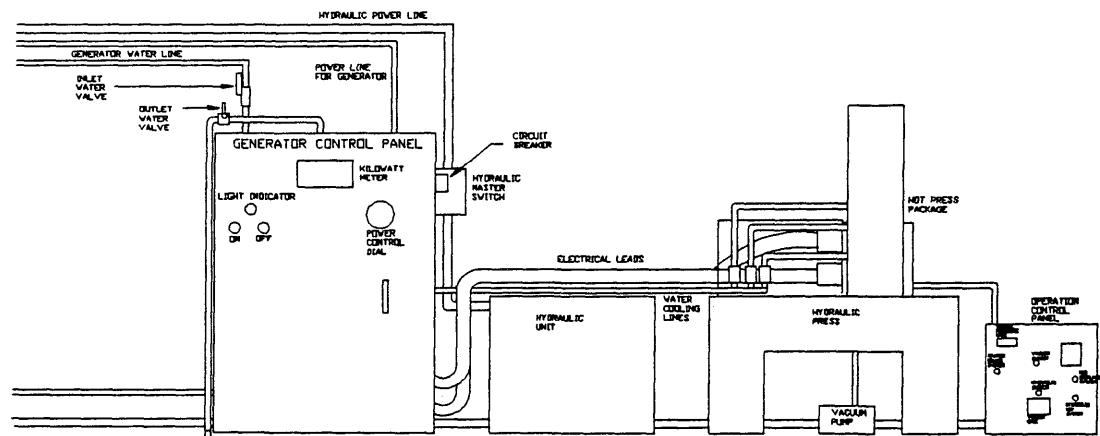


Figure 45 Induction Hot Press System

Radio Frequency Generator

Induction heating systems are efficient units designed with interlocks and circuit protection modules. Operators should be aware of all hazards involving high voltage. The following safety precautions and operational procedure should be read and understood by all operating and maintenance personnel and management personnel responsible for safety.

Operator safety is enhanced by several design features built into the equipment. Deliberately defeating these safeguards can expose the operator to hazards. The following precautions should always be observed.

WARNING

FAILURE TO COMPLY WITH THESE PROCEDURES MAY RESULT IN SERIOUS INJURY OR EXTREME DAMAGE TO THE SYSTEM.

- 1) Keep all cabinet doors locked.
- 2) Keep shields in place over furnace leads, and the plexiglass cover in place at all times during operating.
- 3) Always set main power disconnect to the Off position before opening the induction generator door. Do not depend on interlock devices for protection.

- 4) Insure graphite die and alumina stage are dry.
- 5) Always engage water cooling before operation. Do not depend on interlock devices to prevent coil melt down.
- 6) Always insure that the vacuum is engaged during operation of the system or the appropriate atmosphere is maintained.

Operation of the System

- 1) Clear all items (e.g. tools) from the press platform,
Figure 46.

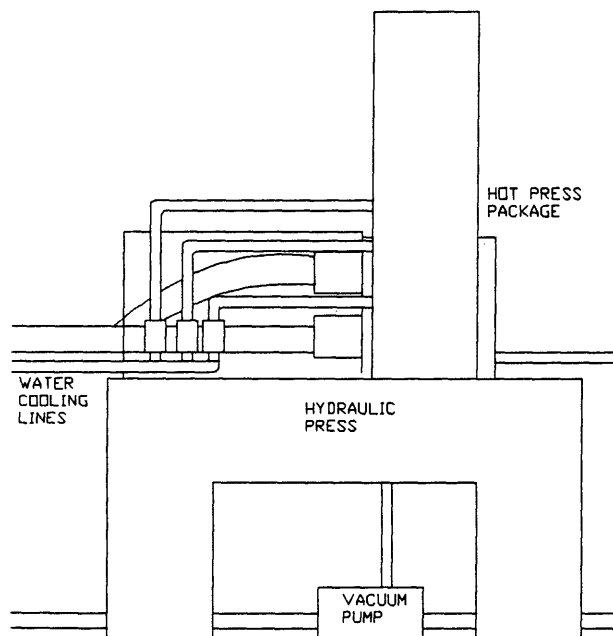


Figure 46 Hydraulic Press with Cooling Water Lines

2) Turn on yellow-handled inlet valve to start cooling water flow to the radio frequency generator. The outlet valve is preset at the required position for optimum flow. Visually check the plumbing for leaks. If leaks are present, turn off water flow and contact supervisor.

3) Open the front panel of the generator control panel, Figure 47,

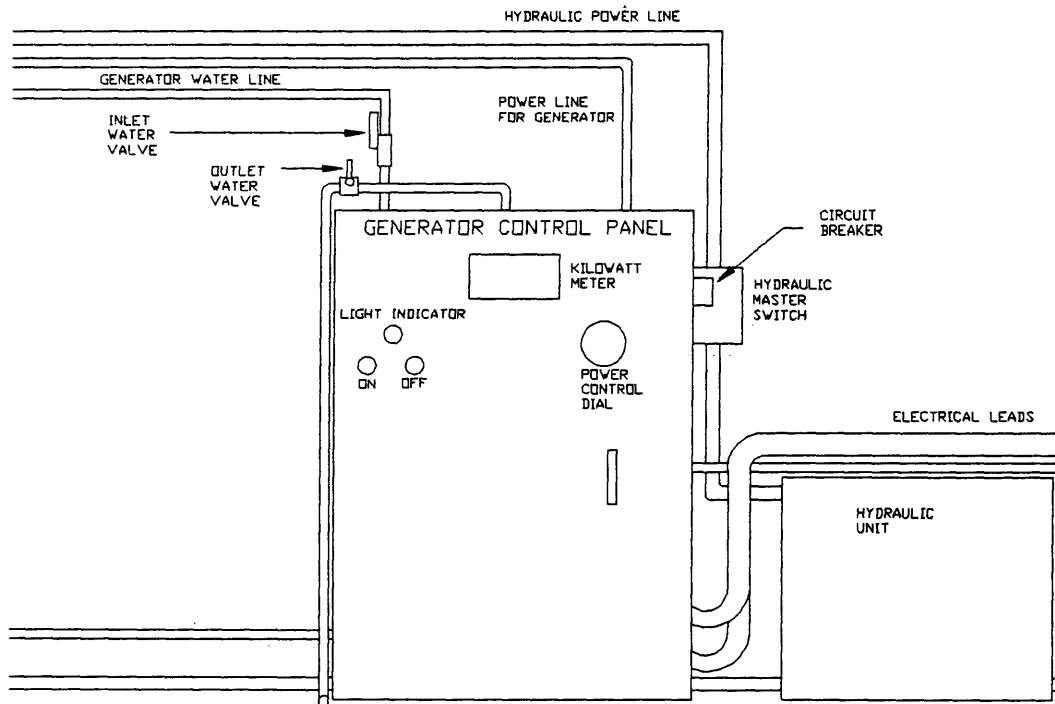


Figure 47 Generator Control Panel

and observe the pressure readings on the inlet and outlet water pressure gages. The pressure on the inlet gage must be >60PSI, the outlet pressure must be >20PSI.

4) Turn on nozzle for the green hose located on the column directly north of the frequency generator. This initiates water cooling of the hot press package.

5) Verify that the load cell is securely fastened to the hydraulic cylinder piston. Then, check that the color-coded electrical leads from the strain gage are properly attached to the corresponding terminals on the strain gage indicator.

****NOTE:** Observe the setting on the gage factor dial located on the front of the strain indicator. The proper gage factor for the load cell is 1.88. This should not be adjusted by the operator. If a different reading is observed, contact the supervisor.

6) Verify that the power cords for the hydraulic system and operation control panel are plugged in and that the overhead electrical lines are free of any obstructions.

7) Turn on the master power switch on the operation control panel.

8) Engage the master switch for hydraulic operation (located on the right-hand side of the generator control panel).

9) Engage vacuum switch located on the front of the operation control panel, Figure 48.

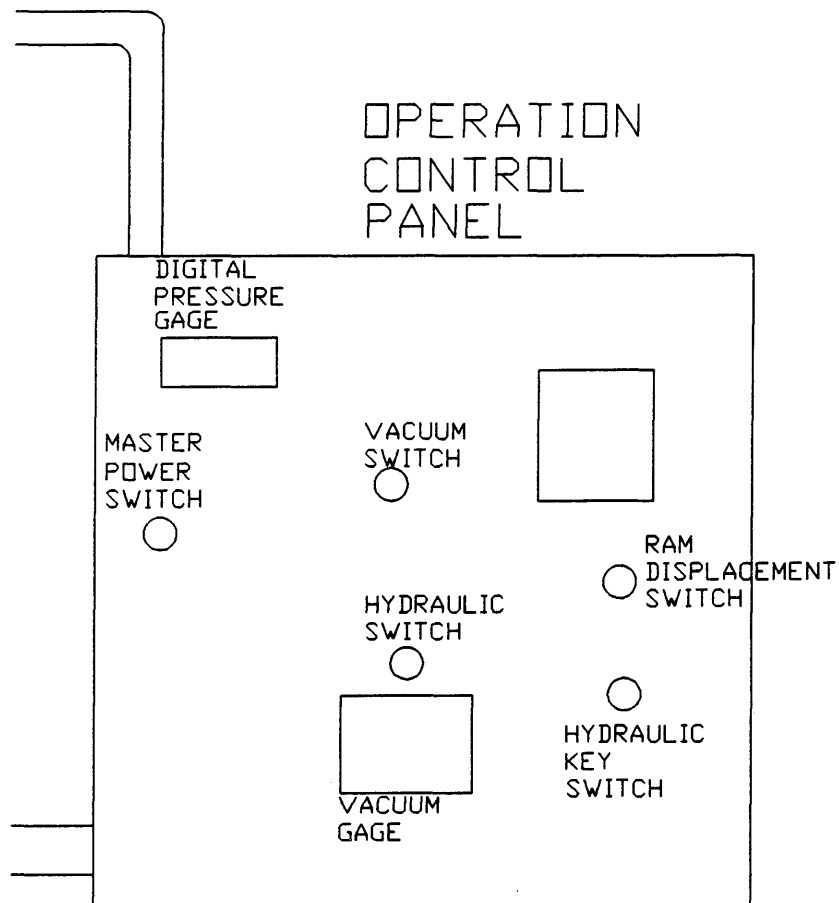


Figure 48 Operation Control Panel

and verify that the adjacent indicator light comes on. Then, turn on both the motor and "gas ball" switches on the fore-pump located underneath the press frame.

10) The hydraulic key switch is located on the operation control panel. Turn on the hydraulic switch and verify that

its adjacent indicator light comes on indicating power to the hydraulic system.

WARNING

Step 11 requires particular attention to procedure as severe damage to the equipment can result by improper operation of the ram displacement control switch.

11) While watching the load cell, engage the ram displacement control switch to the down position (located on the operation control panel). This will move the load cell downward towards the ram. Be careful that the load cell is stopped approximately 1 inch above the ram by turning OFF the ram displacement switch. The switch operates the movement of the load cell in both directions and is used to adjust the height to the specified 1 inch clearance.

12) Confirm that the hot press package is axially aligned with the load cell so that when the load cell is brought into contact with the ram, the parts seat flush against each other. If alignment is required, adjust the position of the hot press package at this time.

13) The hydraulic power supply dial is located on the Vickers control panel (on the operations control panel).

Observe that the indicator light is on at this time. Set the dial to zero to bring the hydraulic pressure to its minimum value.

14) Turn on the induction furnace power switch. This is the top switch on the breaker panel near the north wall of the bay.

15) Provide power to the generator control panel:

a. Depress the circuit breaker on the right-hand side of the generator control panel.

b. Lower the adjacent power switch while holding down the circuit breaker.

c. Release the circuit breaker and the power switch should now remain in the down position and the large, red indicator light on the front on the generator control panel should remain on.

16) Engage the hydraulic load:

a. Place the ram displacement switch into the down position. The load cell will be brought into contact with the ram.

b. Set initial hydraulic pressure by adjusting the setting on the hydraulic power supply dial on the Vickers control panel.

- 17) Engage frequency generator for induction heating:
- a. Engage the high-frequency control button on the generator control panel. Observe that an initial reading produced on the kilowatt meter (front of generator control panel).
 - b. Use the large, black control dial on the front of the generator control panel to dial-up the selected setting

WARNING

DO NOT EXCEED POWER LIMITS INDICATED ON THE KILOWATT METER LOCATED ON THE FRONT OF THE GENERATOR CONTROL PANEL.

**NOTE: Slowly adjust power level to allow time for off gas producing. This will insure that the vacuum remains low enough for operation.

Shut Down Procedure of the System

- 1) Disengage radio frequency generator slowly to zero power with control dial.
- 2) Turn off radio frequency control button on the generator control panel.

3) Turn off radio frequency generator with induction furnace power switch located in the breaker panel near the north wall of the bay.

4) Disengage the hydraulic load by placing the ram displacement switch to the up position. When the ram is fully retracted place switch in neutral position.

5) Turn off vacuum power switch on the operation control panel once the package is allowed to cool to room temperature.

6) Turn off hydraulic key switch and remove key. Turn off hydraulic switch.

7) Turn of master power switch on the operation control panel.

**NOTE: Observe that all light indicators are off.

8) Turn off strain gage indicator.

9) Turn off water cooling line to the hot press package at the green hose nozzle.

10) Turn off cooling water to radio frequency generator by closing yellow inlet valve above generator control panel.

APPENDIX VII

Drawings of Equipment

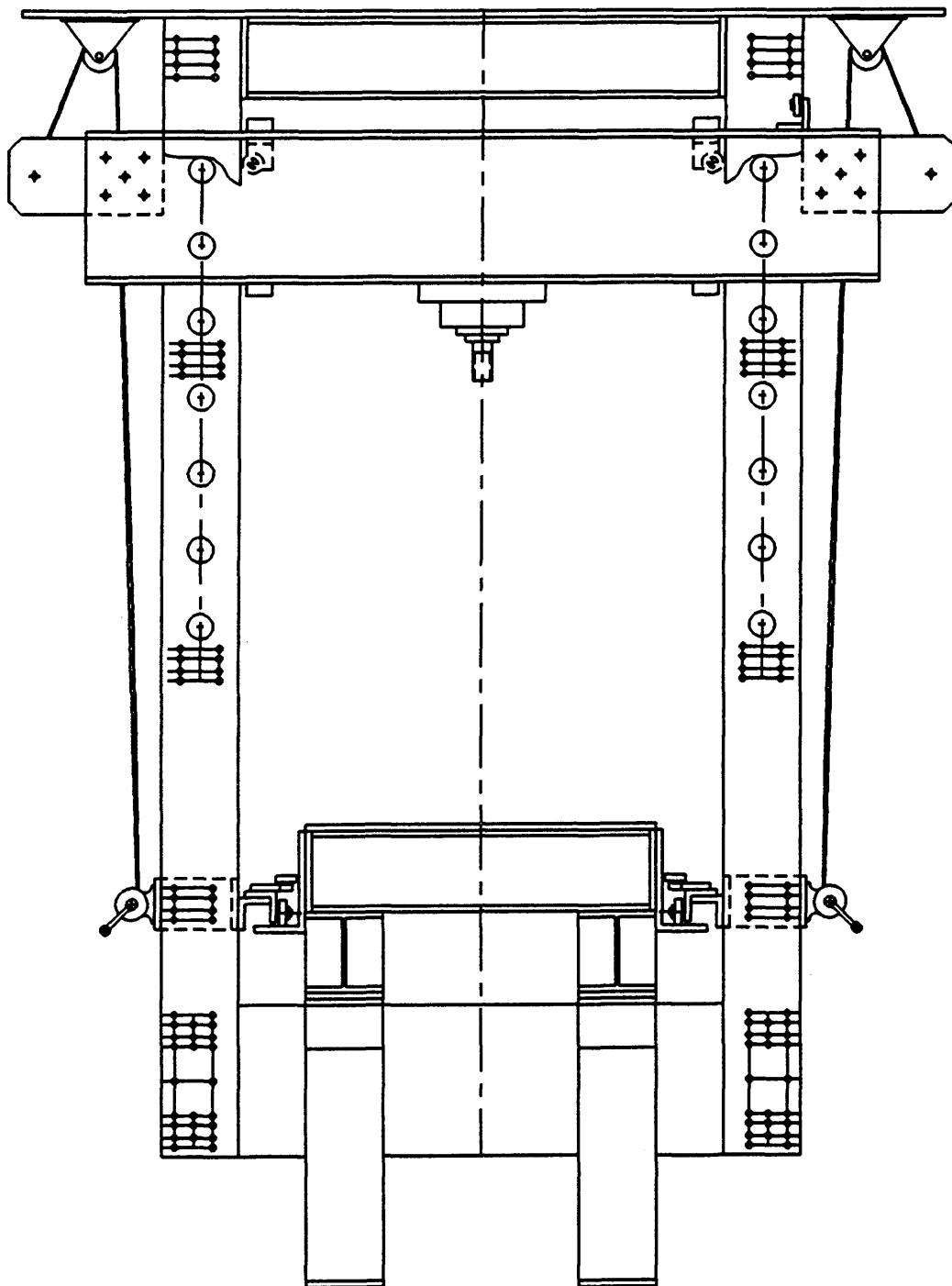


Figure 49 Front View of the Hydraulic Press

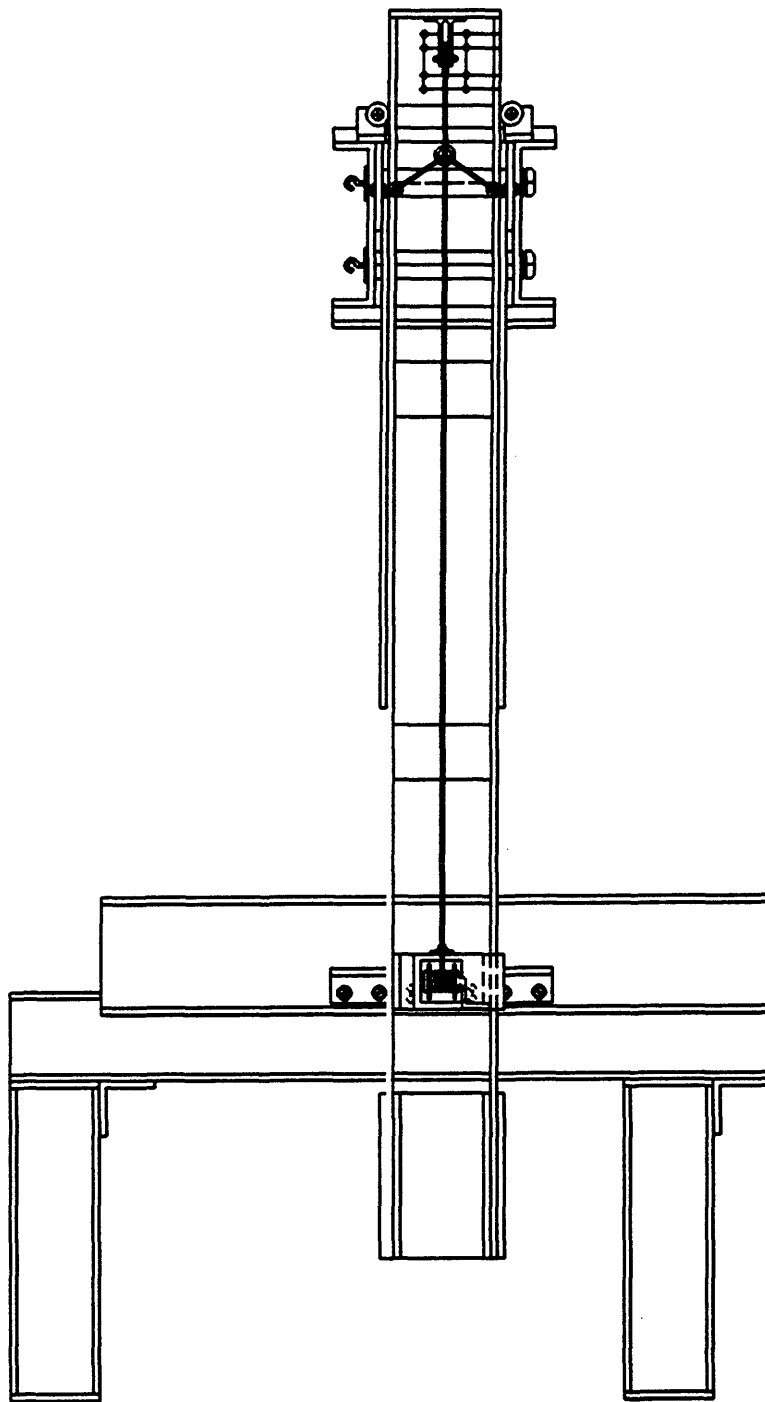


Figure 50 Side View of the Hydraulic Press

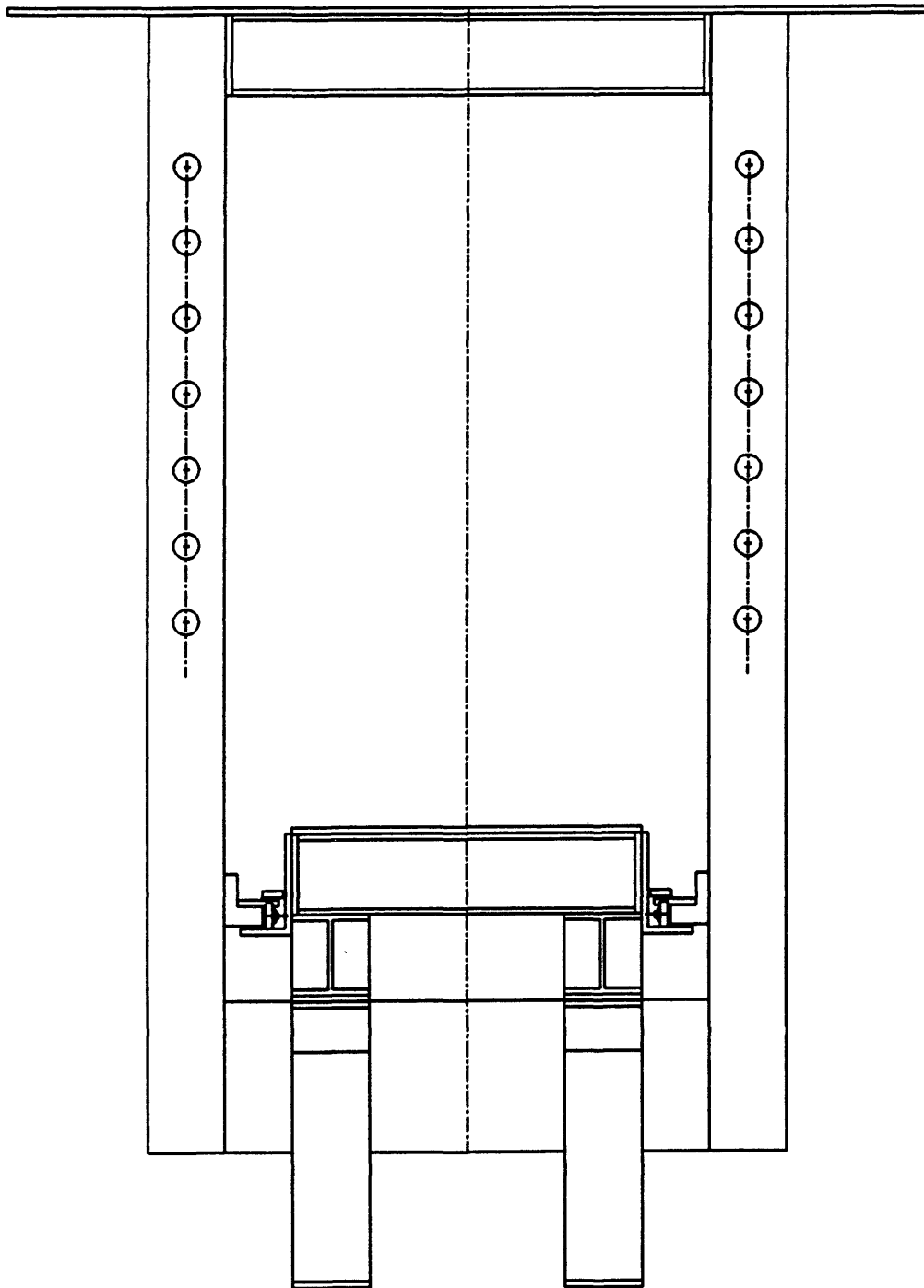


Figure 51 Front View of the Hydraulic Press without the Hydraulic Cylinder Support Structure

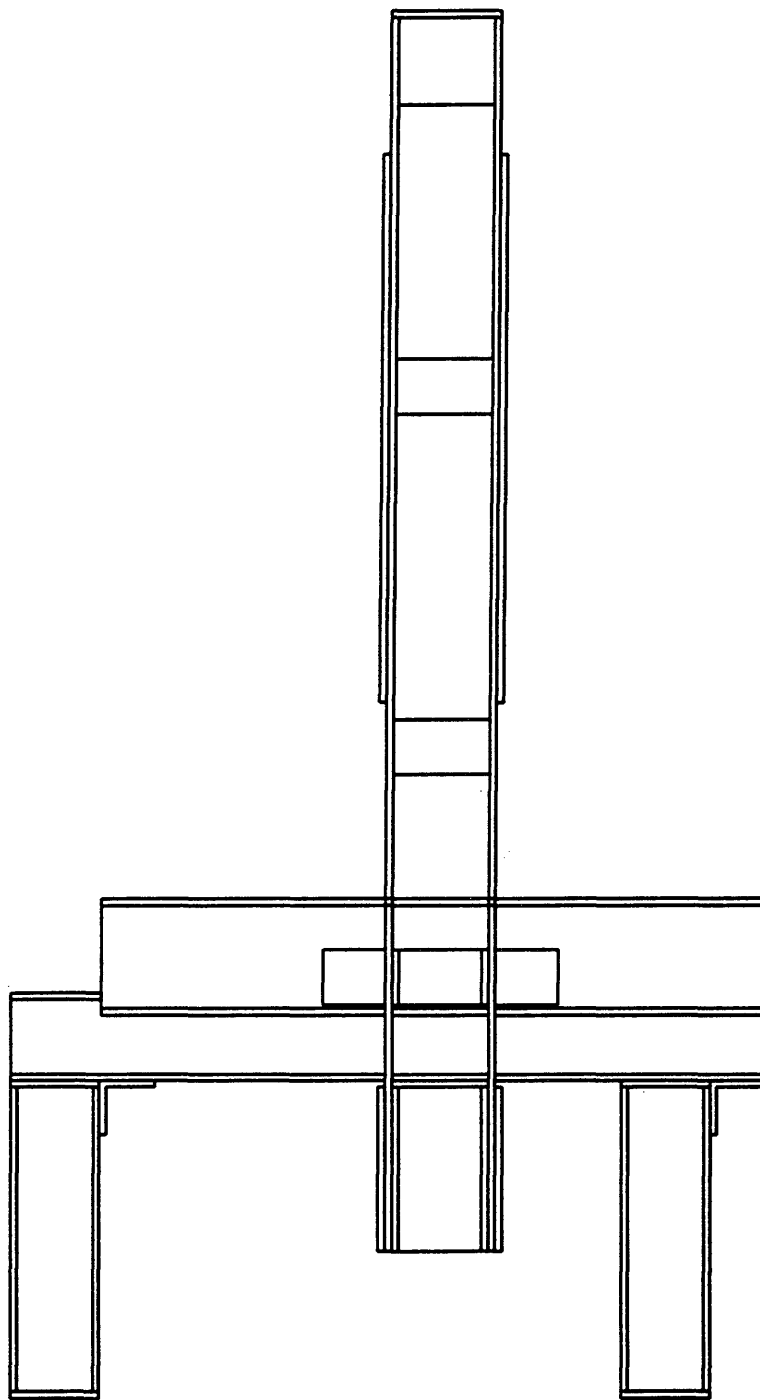


Figure 52 Side View of the Hydraulic Press Without Hydraulic Cylinder Support Structure

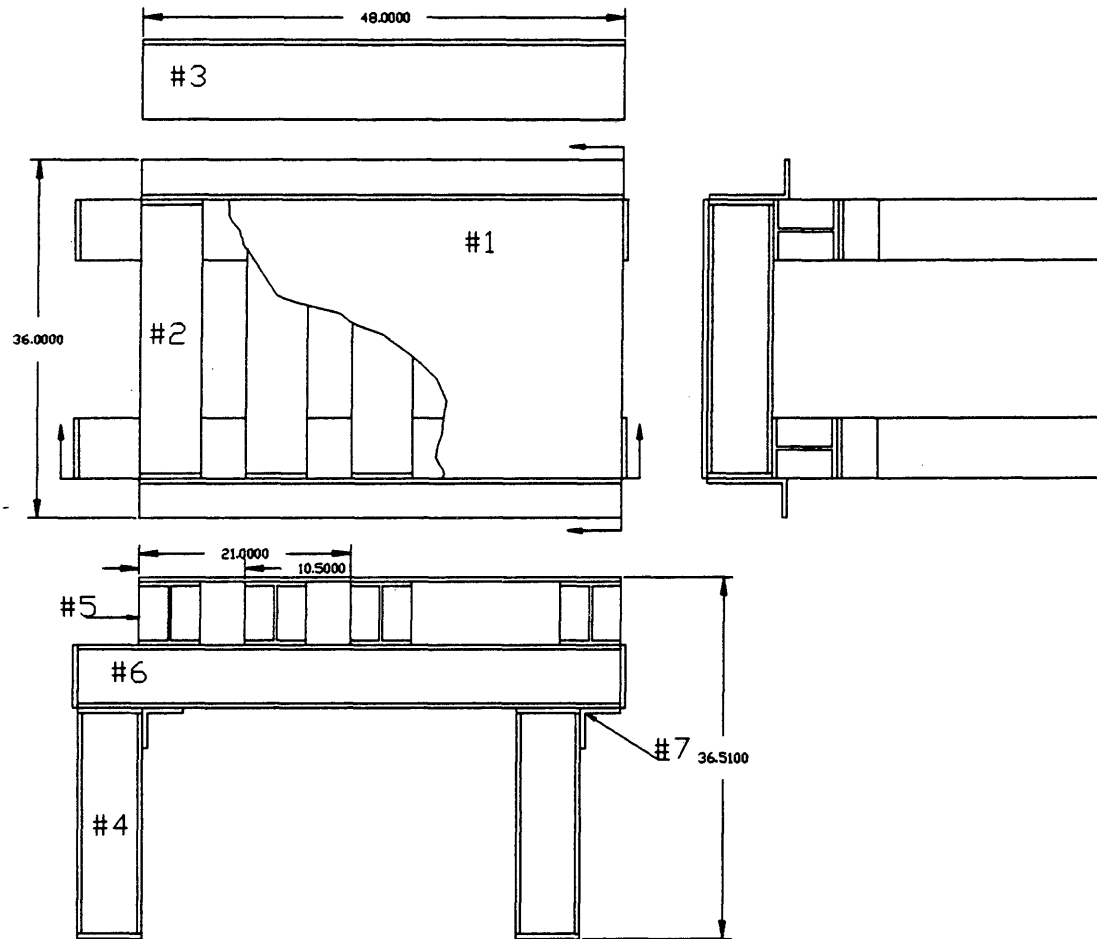


Figure 53 Hydraulic Press Support Table (Units in Inches)

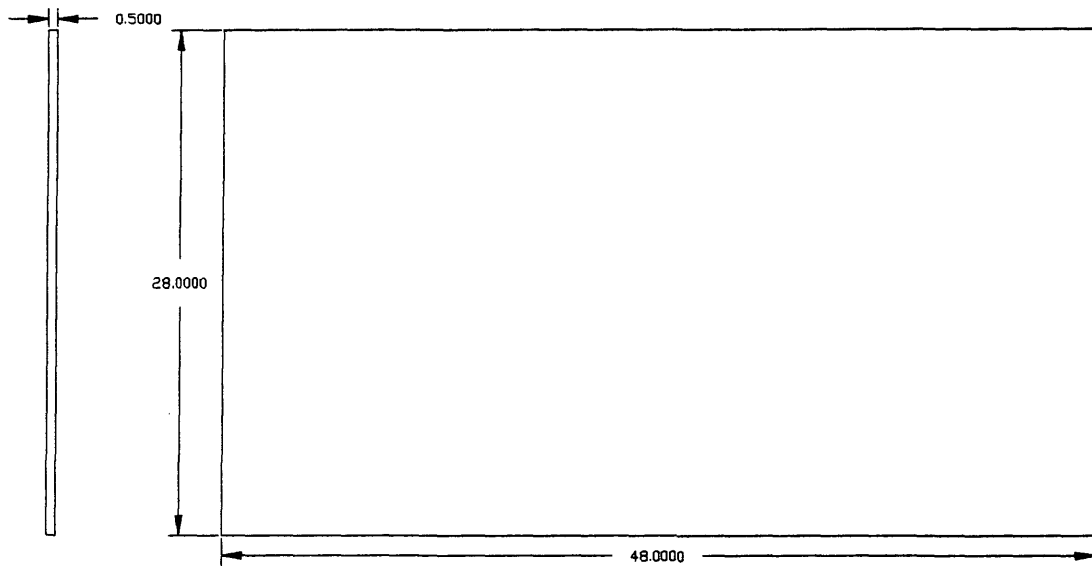
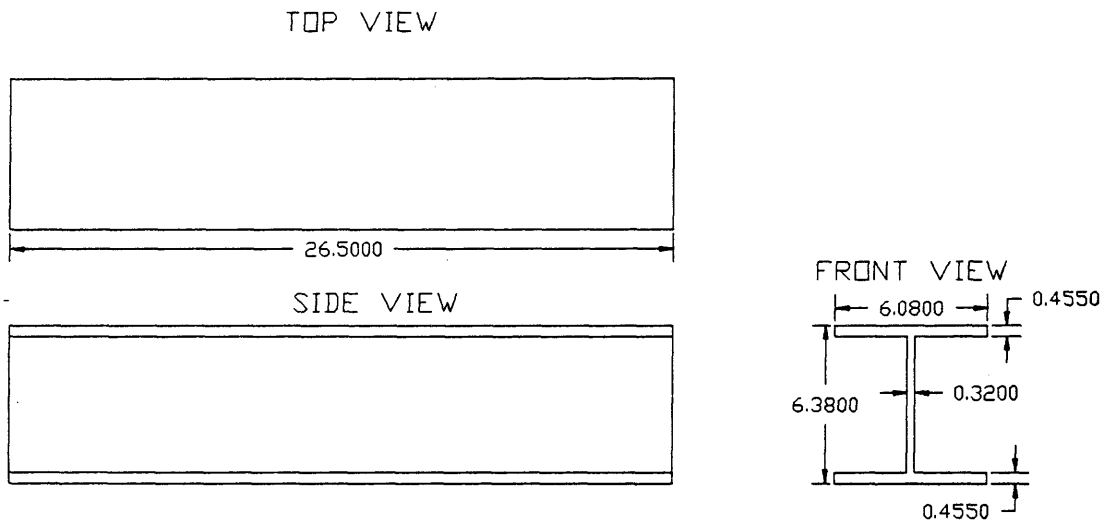


Figure 54 Section #1 of the Hydraulic Press Support Table,
Material AISI 1020 HR Steel, One Plate Total.
(Units in Inches)



**Figure 55 Section #2 of the Hydraulic Press Support Table,
W 6X25 I-Beam, Four I-Beams Total.
(Units in Inches)**

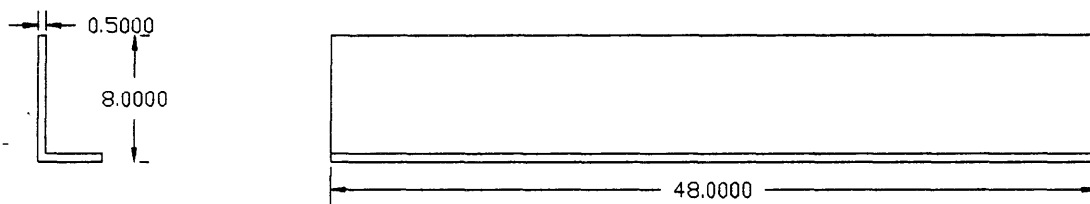


Figure 56 Section #3 of the Hydraulic Press Support Table, Angle Beam L 8X4X1/2, Two Total. (Units in Inches)

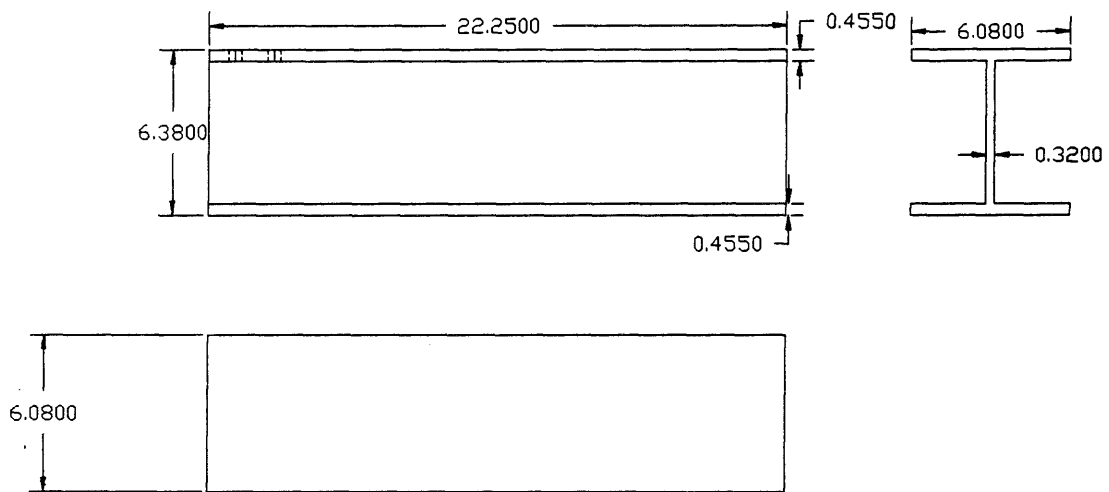


Figure 57 Section #4 of the Hydraulic Press Support Table,
W 6X25 I-Beam, Four I-Beams Total.
(Units in Inches)

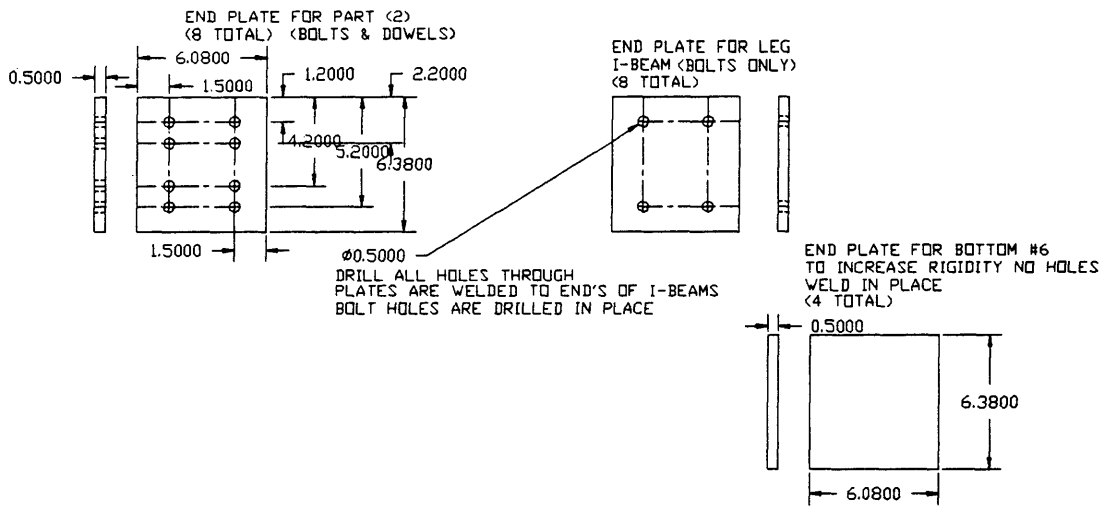


Figure 58 Section #5 of the Hydraulic Press support Table, Material 1020 HR Steel, Twenty Plates Total. (Unit in Inches)

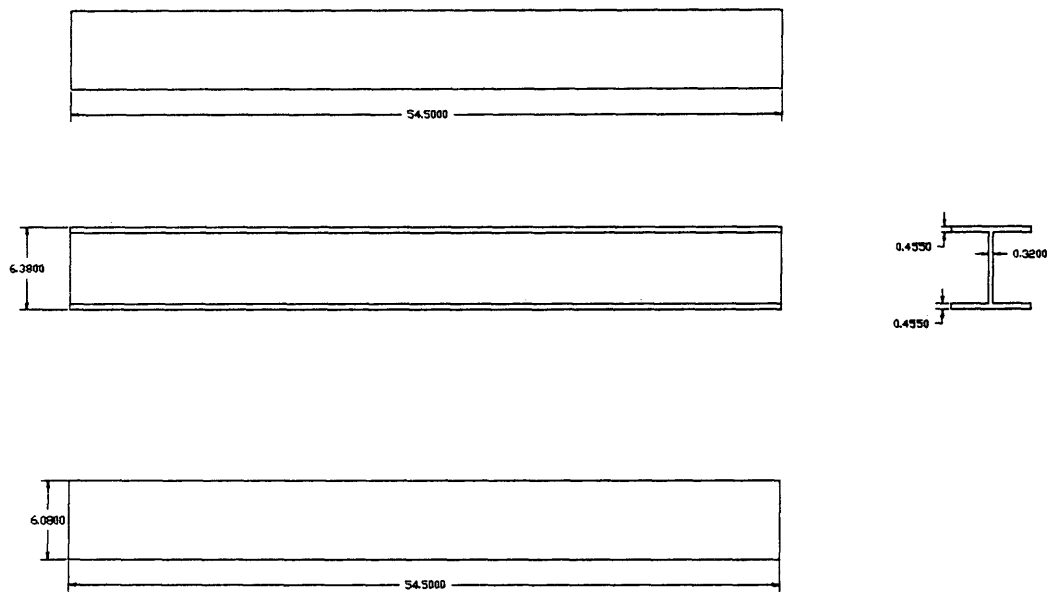


Figure 59 Section #6 of the Hydraulic Press Support Table,
W 6X25 I-Beam, Two Total. (Units in Inches)

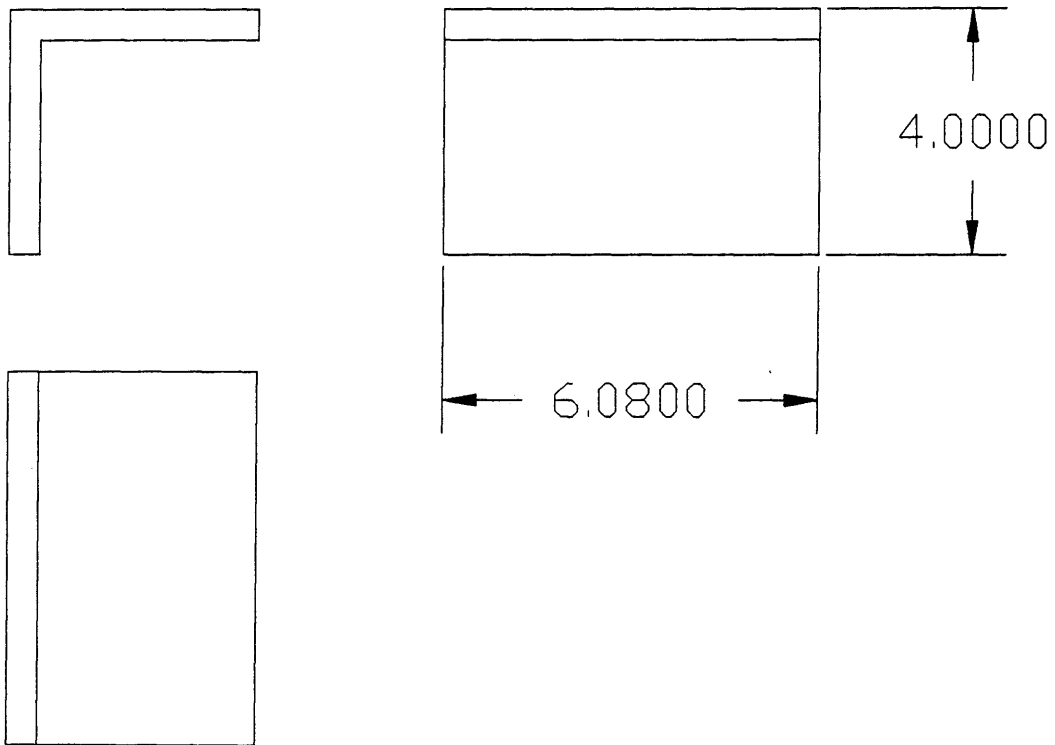


Figure 60 Section #7 of the Hydraulic Press Support Table,
L 4X4X1/2 I-Beam, Four Brackets Total.
(Units in Inches)

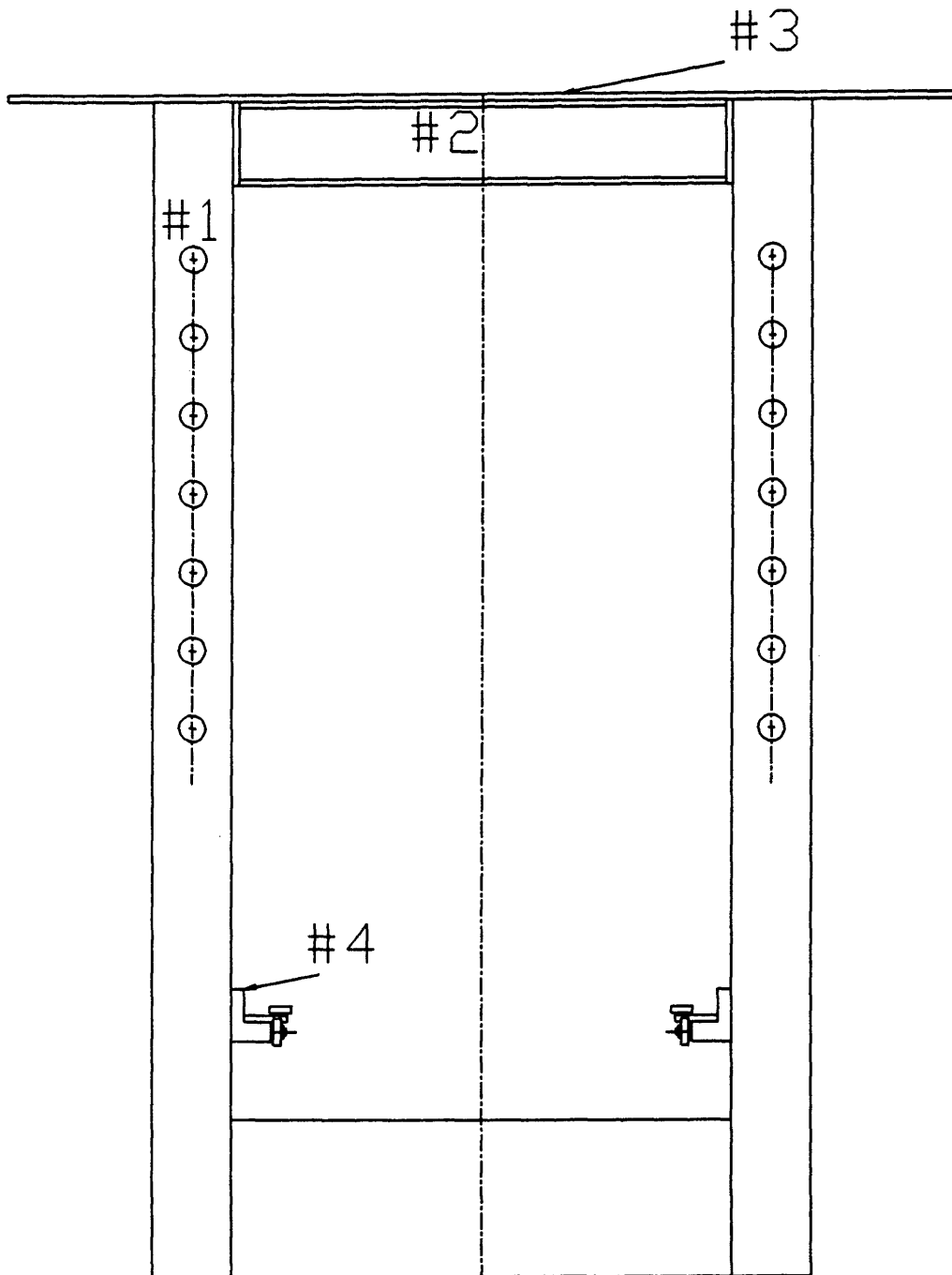


Figure 61 The Hydraulic Press Carriage

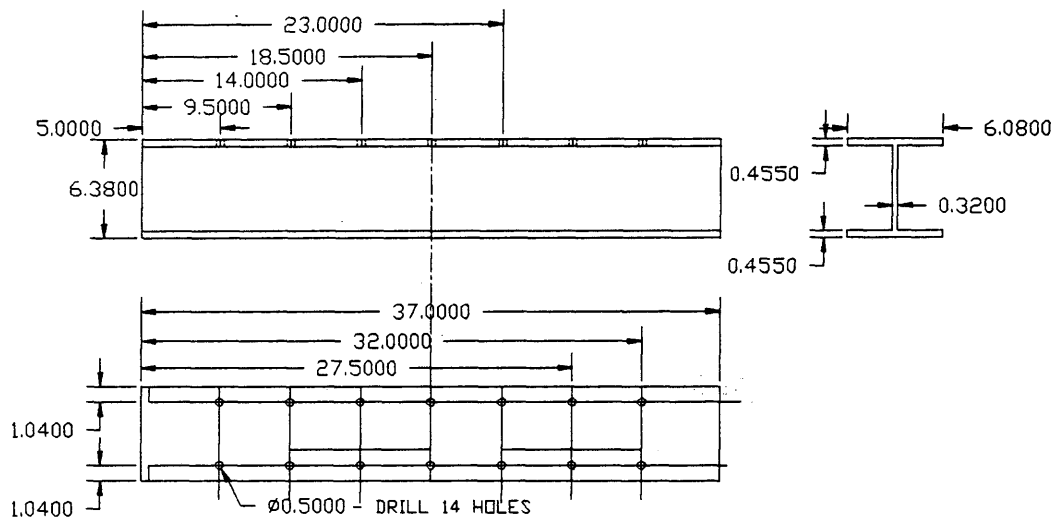


Figure 63 Section #2 of the Hydraulic Press Carriage,
W 6X25 I-Beam, One I-Beam Total.
(Units in Inches)

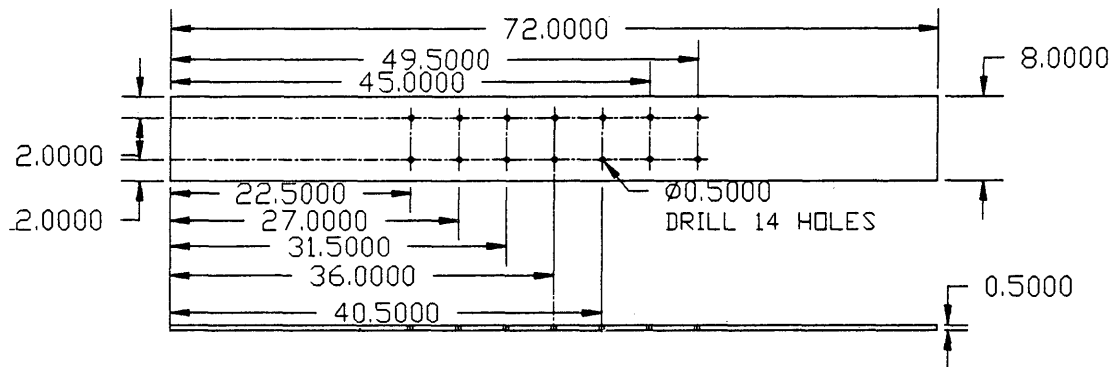


Figure 64 Section #3 of the Hydraulic Press Carriage,
 Material AISI 1020 HR Steel, One Plate Total.
 (Units in Inches)

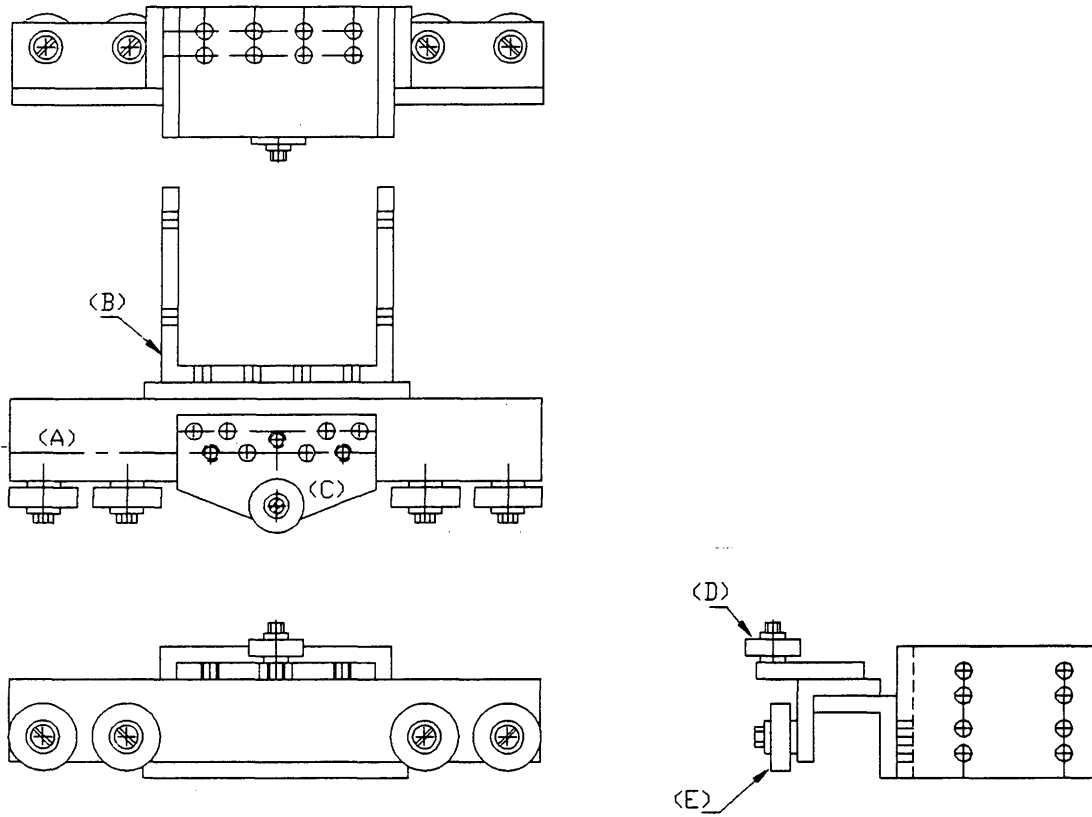
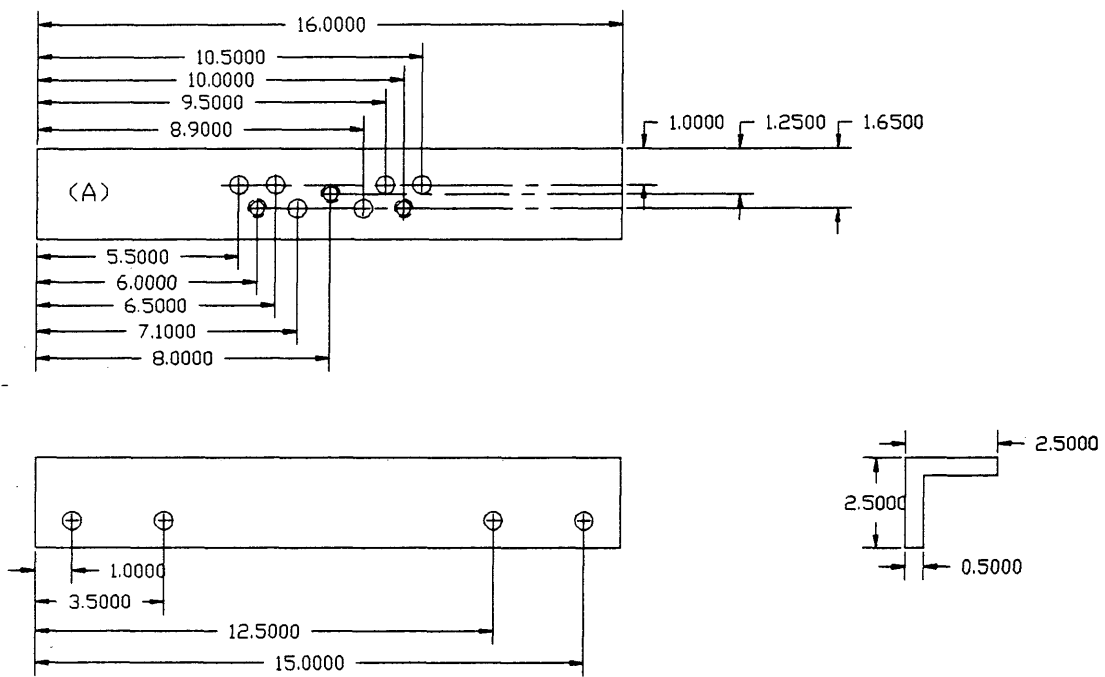


Figure 65 Roller Housing for the Carriage



**Figure 66 Section A of the Carriage Roller Housing,
L 2.5X2.5X1/2 Beam, Four Beams Total.
(Units in Inches)**

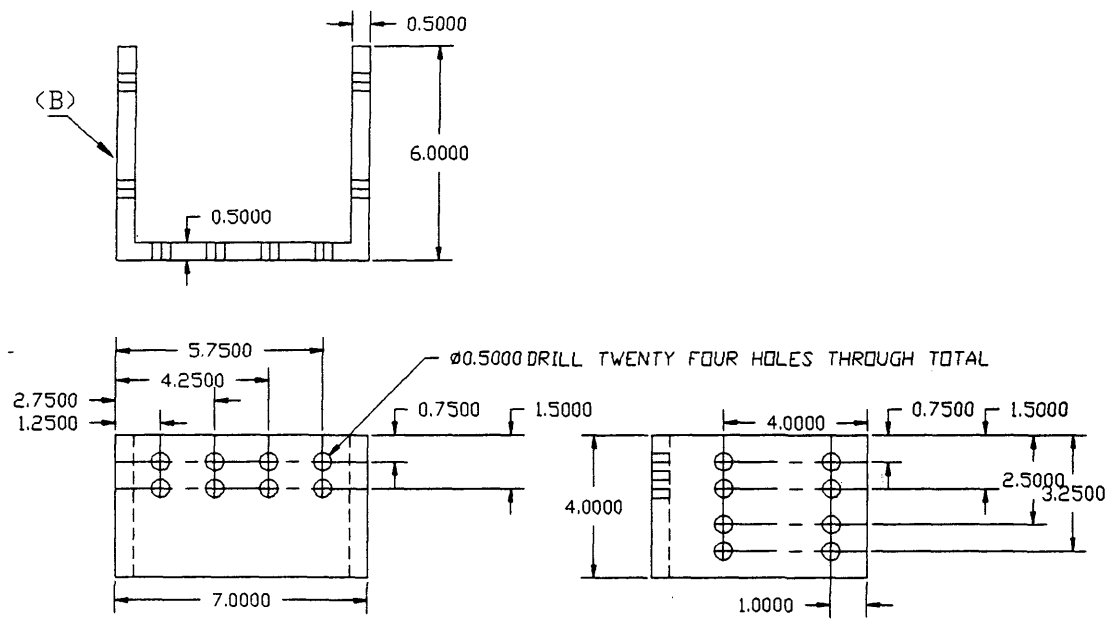
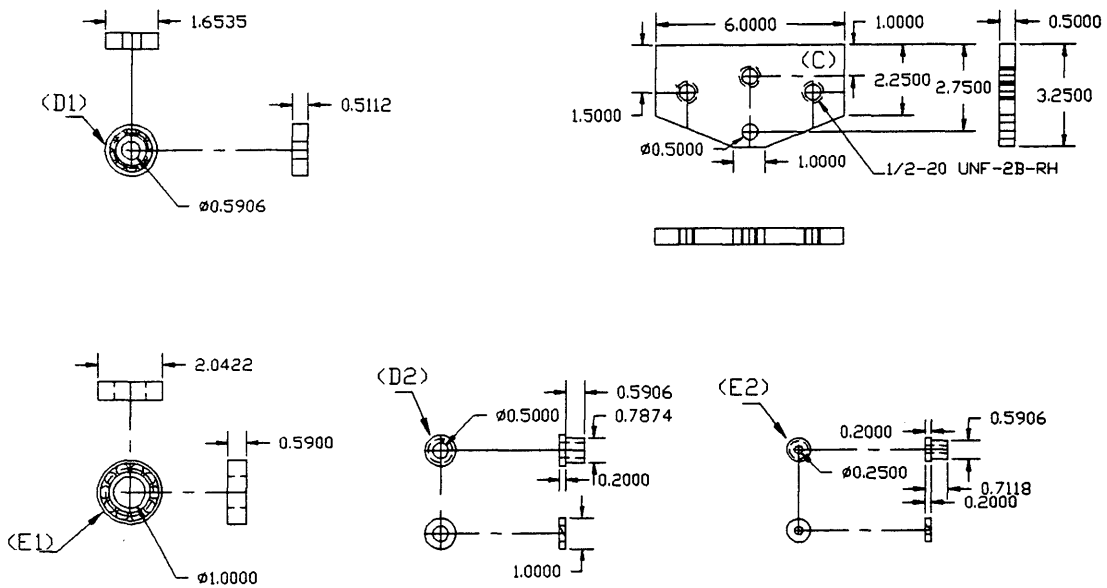


Figure 67 Section B of the Carriage Roller Housing,
 Material AISI 1020 HR Steel, Two Total.
 (Units in Inches)



- MATERIAL: 8-#3304-#Z99604 BALL BEARINGS
 8- AISI 1020 STEEL BUSHINGS (D2)
 8- AISI 1020 STEEL SELF LOCKING WASHERS (D2)
 8-SAE GRADE 8-1/2-UNF-2-SCREWS
 2-#3302 #99602 BALL BEARINGS
 2- AISI 1020 STEEL BUSHINGS (E2)
 2- AISI 1020 STEEL SELF LOCKING WASHERS (E2)
 2-SAE GRADE 2-1/2-UNC-2-BOLTS & NUTS
 1- AISI 1020 STEEL PLATE (C)
 3-SAE GRADE 8-1/2-UNF-2-OVAL ENDED BOLTS

Figure 68 Components for Carriage Roller Housing,
 Material As Specified, Two of Each Component.
 (Units in Inches)

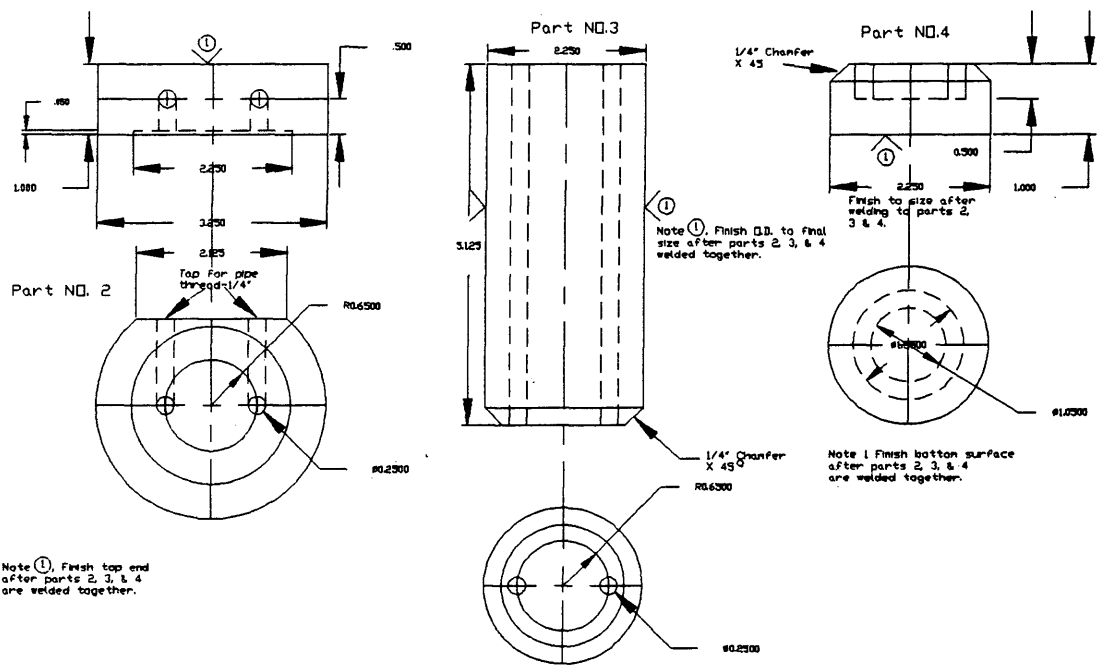


Figure 70 Induction Hot Press Top Plate Ram, Material Stainless Steel, One Total. (Units in Inches)

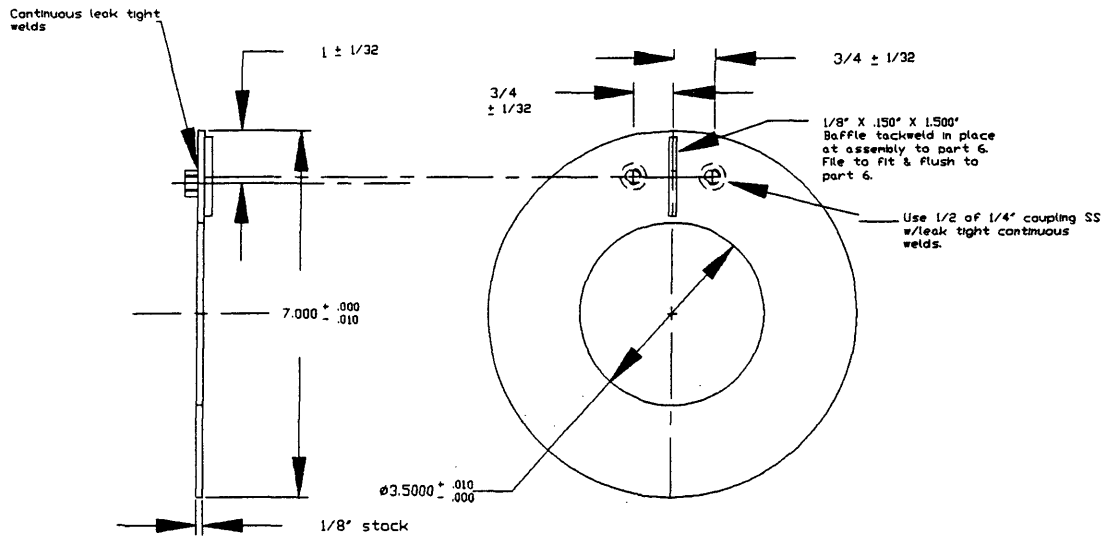


Figure 71 Top Plate Water Channel Cover Plate, Material Stainless Steel, One Total. (Units in Inches)

NOTE: Machine I.D. to size after
weldment assembly to part #3.

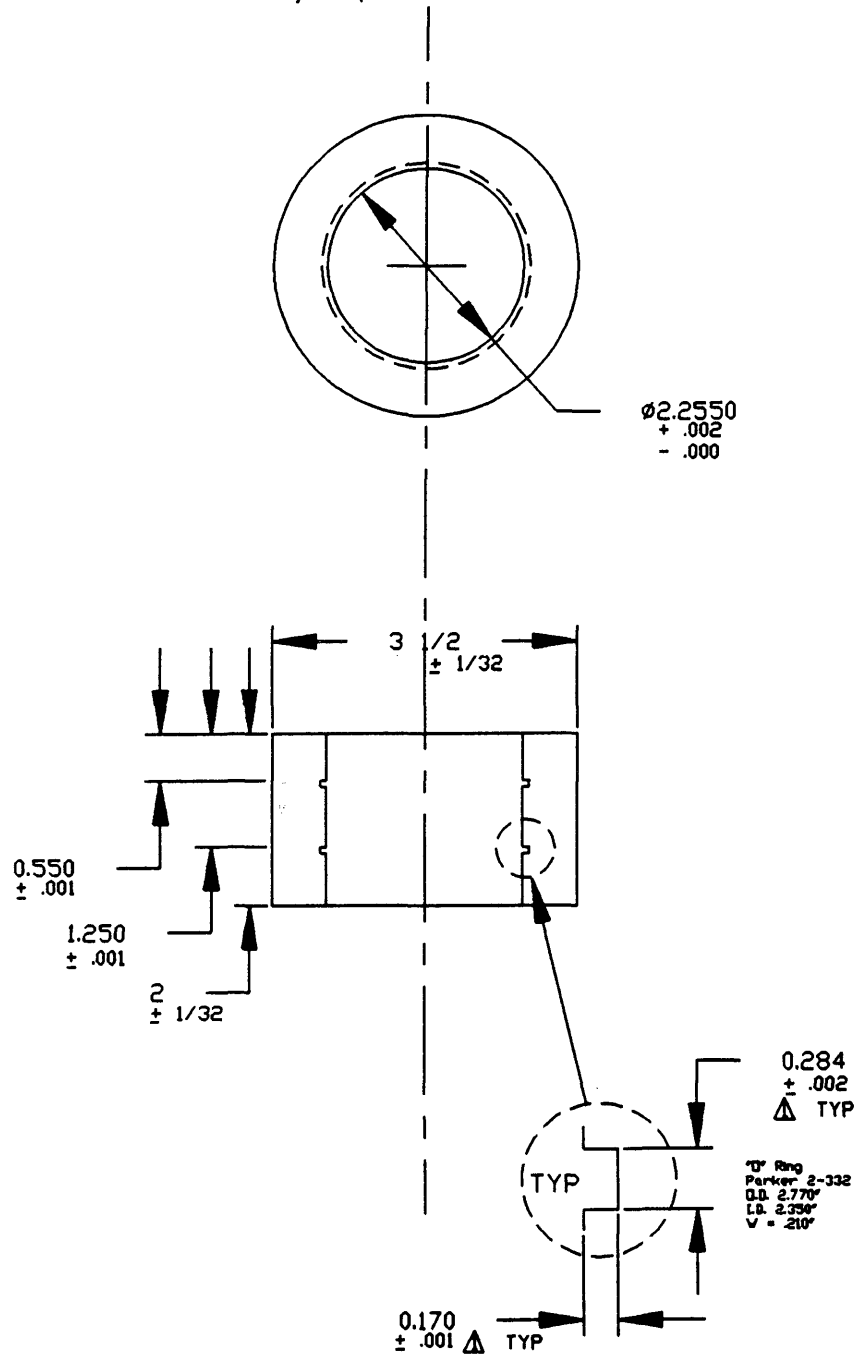


Figure 72 Top Plate Ram Guide, Material Stainless Steel,
One Total. (Units in Inches)

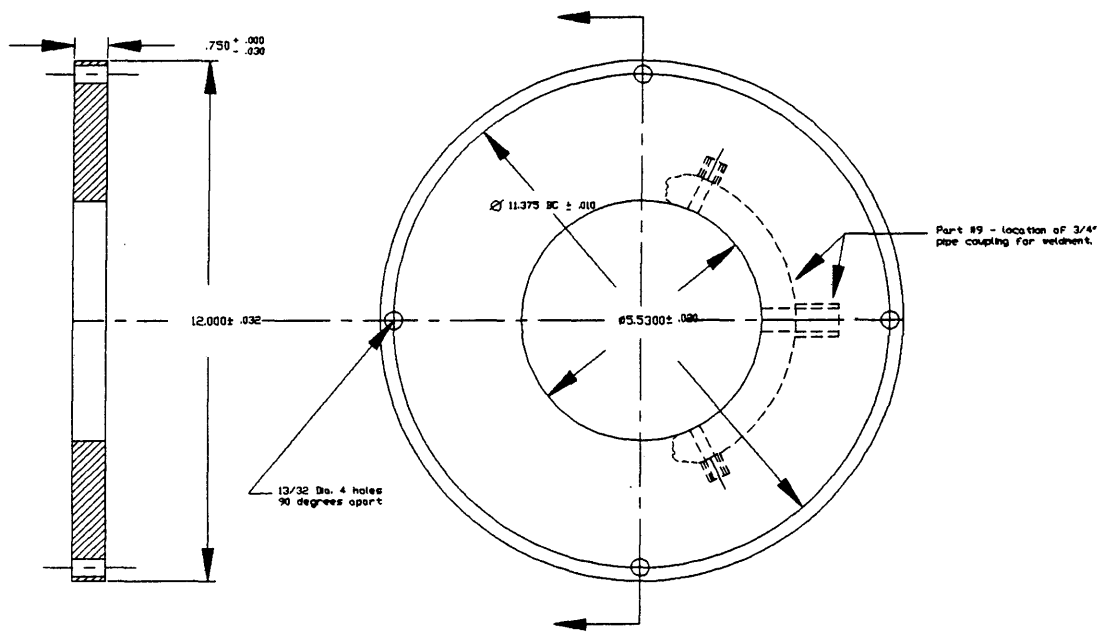


Figure 73 Induction Hot Press Base Plate, Material Stainless Steel, One Total. (Units in Inches)

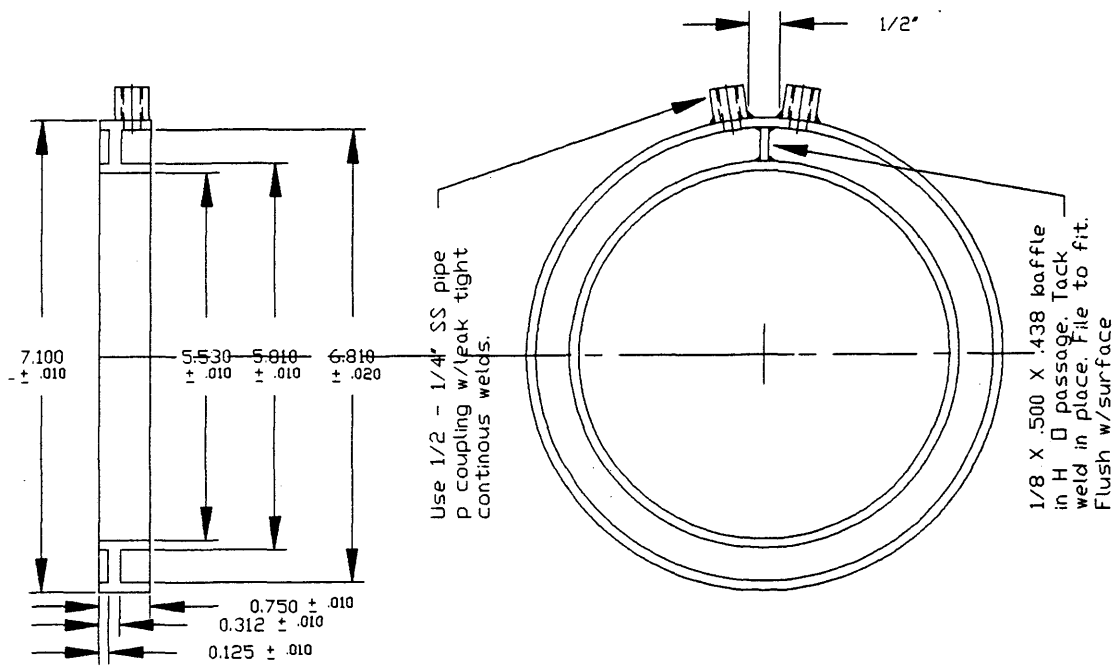


Figure 74 Base Plate Water Cooling Channel Ring, Material Stainless Steel, One Total. (Units in Inches)

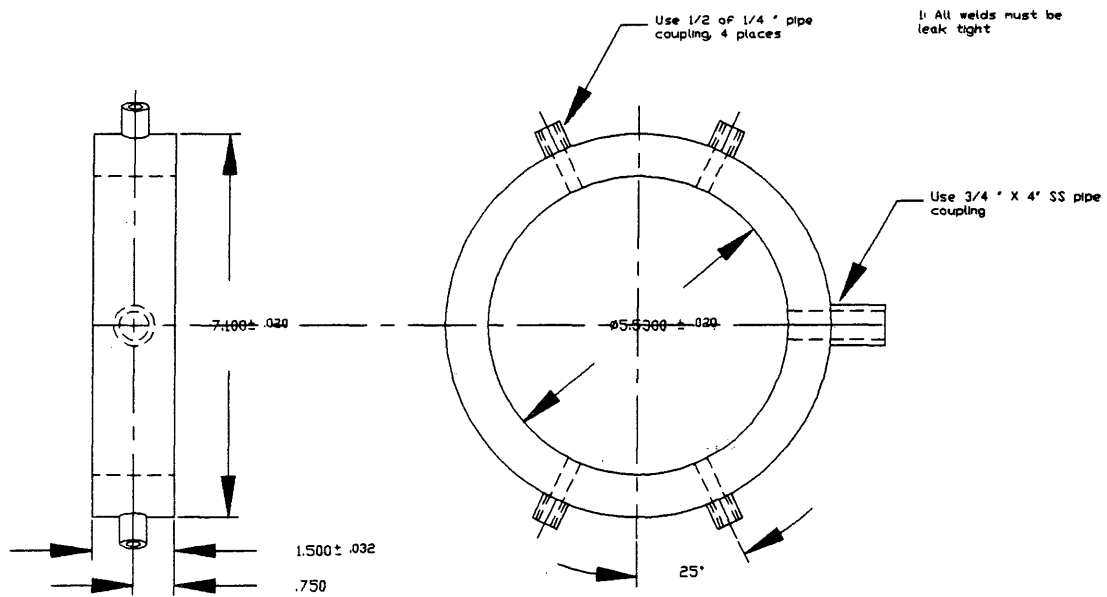


Figure 75 Base Plate Cylinder Stand, Material Stainless Steel, One Total. (Units in Inches)

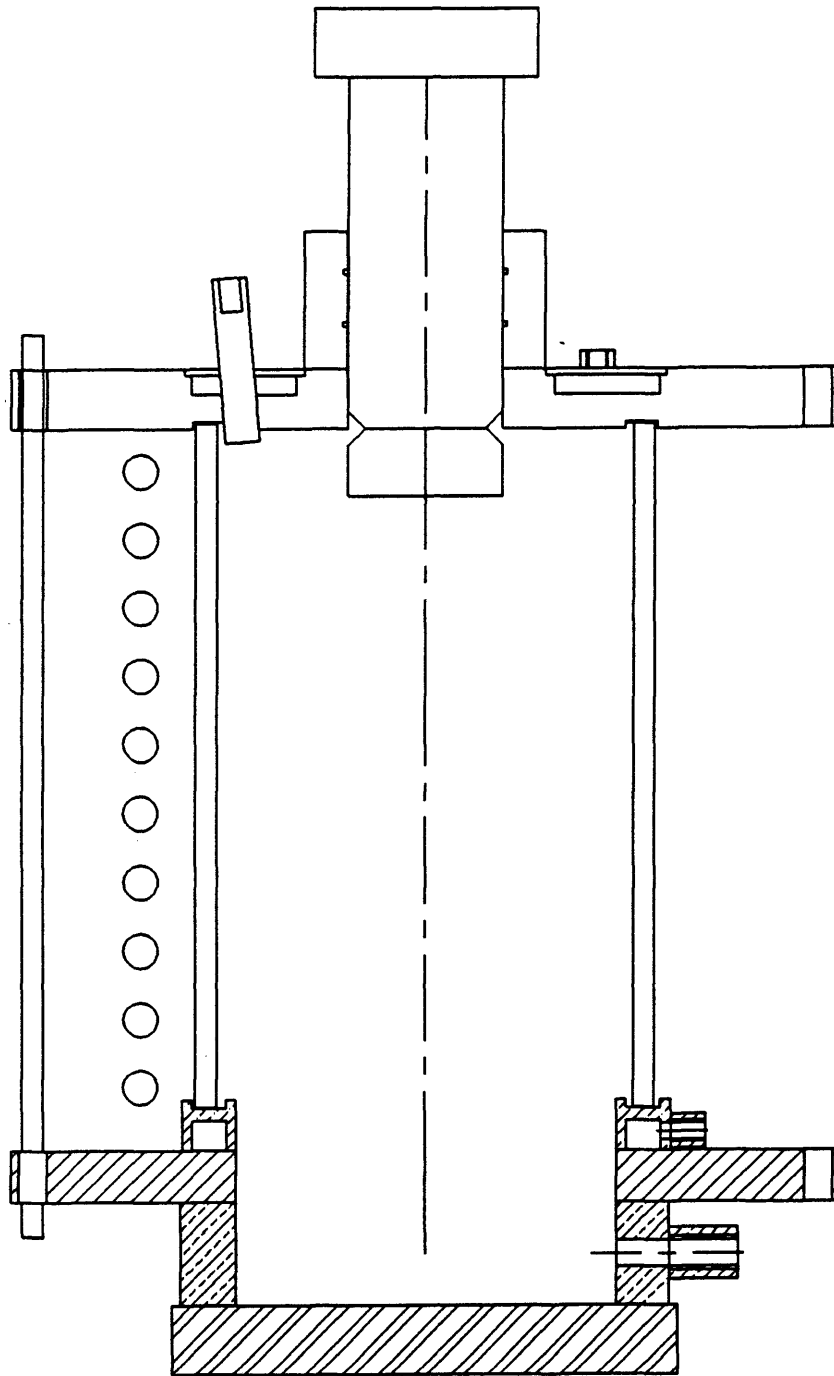


Figure 76 Induction Hot Press without Designations

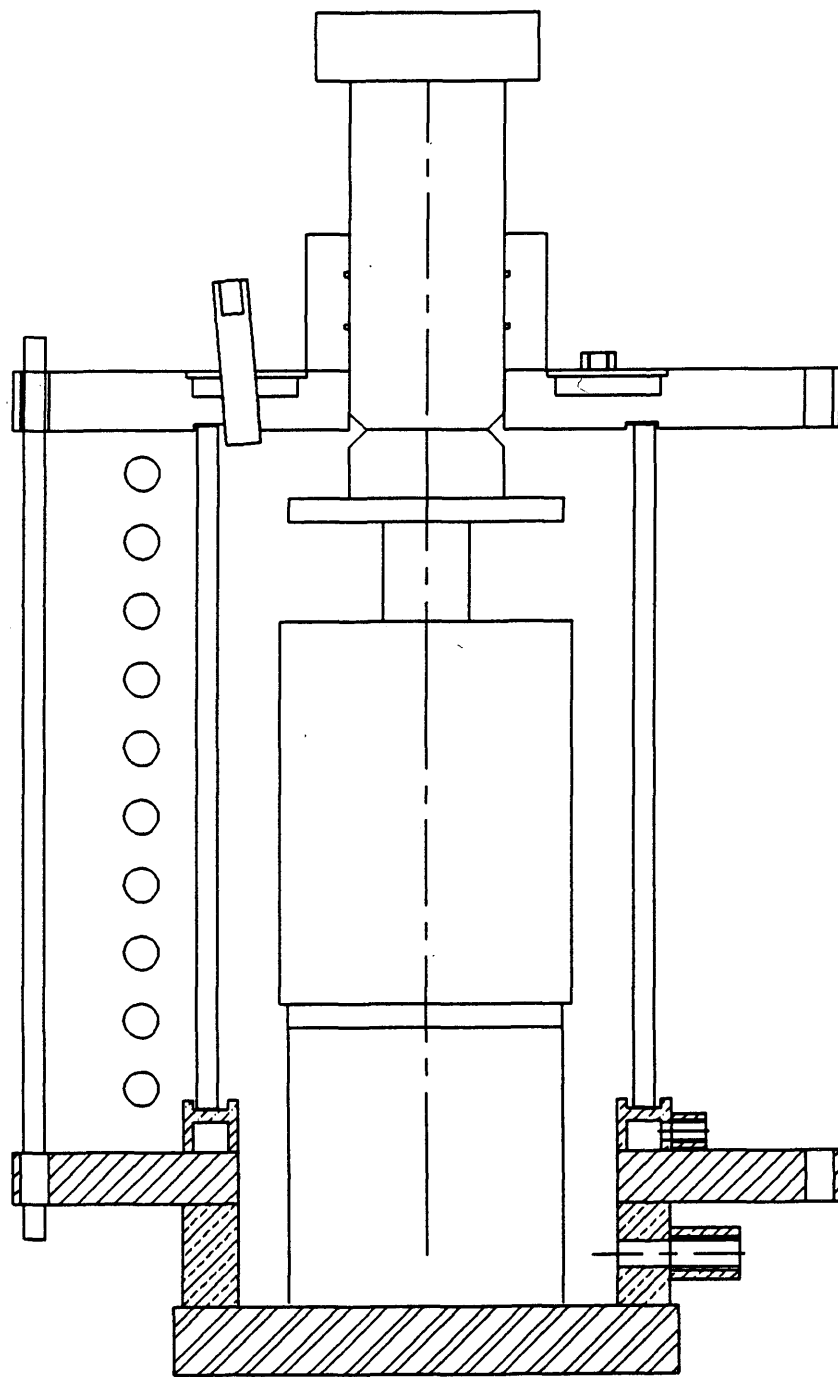


Figure 77 Induction Hot Press with Induction Stack